A PROTOCOL FOR PHYSIOLOGICAL MECHANICAL TESTING OF CORTICAL BONE USING DIGITAL VOLUME CORRELATION

BY

MICHAEL ROGALSKI

THESIS

Submitted in partial fulfillment of the requirements
for the degree of Master of Science in Mechanical Engineering
in the Graduate College of the
University of Illinois Urbana-Champaign, 2021

Urbana, Illinois

Adviser:

Associate Professor Mariana Kersh

ABSTRACT

As we age, an imbalance and uncoupling in the remodeling process deteriorates the intracortical network and subsequently weakens our bones. Impaired mechanical strength, structural degradation, and deficient material composition point to a loss of bone quality that leads to osteoporosis. As bone quality and strength decrease, patients become at high risk for osteoporotic fractures during a fall or other atypical loading conditions. Among these fractures, femoral neck fractures (or cervical hip fractures) lead to high mortality rates and societal costs. Dual-energy x-ray absorptiometry (DEXA) is the current gold standard for measuring apparent bone mineral density for diagnosing osteoporosis, but it continues to be an imperfect predictor of osteoporotic fracture risk. Thus, high resolution imaging techniques paired with mechanical testing and simulations are needed to better understand how the cortical pore network distributes load and which microstructural properties are the best indicators of fracture risk. Additionally, exercise is known to improve overall bone health, but targeted exercise interventions in the femoral neck have been less successful.

The overall objectives of this thesis were twofold. First, we aimed to quantify the physiological level of strain in the proximal femur during regular activity and characterize the resulting mechanical environment. Second, we aimed to perform a digital volume correlation (DVC) error analysis on cortical bone and perform mechanical testing to develop a protocol for loading bone and measuring local strains using DVC.

To investigate the normal level of strain in the femoral neck, we used 3D subject-specific finite element (FE) models to compare principal strains and their orientations for three loading configurations: [1] hip joint force, gluteus medius, gluteus maximus, gluteus minimus, vasti, iliopsoas, and several other smaller hip spanning muscles, [2] hip joint, gluteus medius, gluteus minimus, and the iliopsoas, and [3] hip joint force only. The principal strains and their orientations were compared in four quadrants of 8 regions during walking. Our findings indicate that including muscle forces result in more physiologically accurate FE models, and they support the hypothesis that FE models used to calculate femoral neck strains during walking should not neglect the contribution of muscle forces. These results help establish a baseline for the normal level of strain in the femoral neck which will help create new exercise interventions that cause bone adaptation and subsequent strengthening of the femoral neck.

For the DVC analysis, a pair of consecutive micro-CT scans was acquired of specimens from the superior neck, inferior neck and middle diaphysis with no motion between the

scans. The effect of three DVC input parameters on strain error was assessed via a Design of Experiments (DOE). Although the femoral neck specimens had large in-plane strain errors, the ε_{zz} component was 1,330 $\mu\varepsilon$, which indicates that uniaxial compression/tension testing of these specimens via DVC is feasible. Loaded DVC of femoral neck specimen may help elucidate the relationship between intracortical pore morphology and local strain, which may one day lead to new insights into (re)modelling mechanisms and femoral neck fragility.

To my parents, for their love, support, and ultimate sacrifice of emigrating to a foreign country in search of better opportunities for their children. Thank you to my siblings for their support and guidance throughout my life.

To my grandparents, for their love and encouragement from a young age.

To Dani, for her love and dedication.

ACKNOWLEDGMENTS

First and foremost, I would like to express my greatest appreciation to my advisor, Dr. Mariana Kersh, for her insight and wisdom in engineering, research, and life. She has been patient and encouraging at every step of my thesis project. Thanks to her guidance and mentorship I have developed invaluable research and engineering skills that will serve me a lifetime. Her passion for biomechanics is unmatched, and she is a role model of how to manage and lead an interdisciplinary research team. Thank you Dr. Kersh for fostering a fun and welcoming lab environment - I will greatly miss the discussions, coffee (tea) runs, and lab gatherings.

Thank you to the Tissue Biomechanics Lab members Roberto, Sara, Sony, Chenxi, Hyung-gwi, Kellie, Michael, Sam, Mikayla, Josh, Griffin, Elahe, and Berat. You all have helped me countless times and created a lab culture that is difficult to say goodbye to. Thank you for always providing helpful feedback and for the years of jokes, laughs, and research collaboration. I would also like to give a shout out to Dr. Thomas Levin Geiser Andersen and the rest of our collaborators at the University of Southern Denmark - it has been a pleasure working with you all.

I am grateful to the Beckman Institute, especially Travis Ross at the Vis Lab and Dr. Leilei Yin at the Microscopy suite for their help with my research project, along with all of the Beckman faculty and staff who make working here possible. Thank you to the Velux foundation for project funding, to the International Society of Biomechanics (ISB) for an international travel grant, and to the Mechanical Science and Engineering Department for the fellowship and opportunities over the past 6 and a half years. I will fondly remember my times spent on this vibrant campus.

Finally, I would like to thank my family. I am deeply grateful to my parents for supporting my path in life, my grandparents for encouraging me to be a scientist from a young age, and to my siblings for their support and guidance. Thank you to Dani for her love, dedication and motivation to help me reach this milestone.

TABLE OF CONTENTS

LIST OF TABLES

LIST OF FIGURES

CHAPTER 1

INTRODUCTION

1.1 Structure, function, and composition of bone

Bone is a mineralized tissue responsible for providing shape and structure to the body, protecting vital organs, contributing to movement, producing blood and regulating physiological processes. Based on their main shape, bones are categorized into four groups: long, short, flat or irregular. The primary mechanical role of long bones, such as the femur, is to support weight and facilitate movement. Long bones are comprised of a long hollow shaft called the diaphysis, a metaphysis on both ends that includes the growth plates, and a rounded epiphysis on both ends (Fig. 1A) [14, 15].

Bone is also categorized as either cortical bone or trabecular (cancellous) bone; the average adult skeleton is made of 80% cortical bone and 20% trabecular bone. Cortical bone forms the dense outer layer of bone, and is responsible for a large proportion of weight bearing function [16, 17]. Trabecular bone is a sponge-like lattice of plates and rods responsible for load transfer within bones. In long bones, the diaphysis contains thick cortical bone, while the metaphysis and epiphysis contain both trabecular and cortical bone (Fig. 1B) [14, 15].

Cortical bone is a hierarchical and composite material that results in unique properties depending on the location, direction, and length scale evaluated. At the nanoscale, the constituents by volume of cortical bone are mineral crystals (33-43%), organic collagen fibers (32-44%), and water (15-25%) (Fig. 2) [18]. Hydroxyapatite (HA) is the predominant mineral crystal in bone and it contributes to hardness, while the collagen fibrils provide elasticity. The mineral crystals and collagen fibers are the microscopic building blocks that form mineralized collagen fibrils orientated along the main axis of the collagen fibers. Continuing up the hierarchy, the collagen fibrils are arranged in fiber arrays creating lamellar sheets with varying orientations. These lamellar sheets surround the central canal of blood vessels and together make up the osteon (Fig. 2) [19]. This hierarchical and composite organization of bone is key to its strength, toughening mechanisms, and crack mitigation.

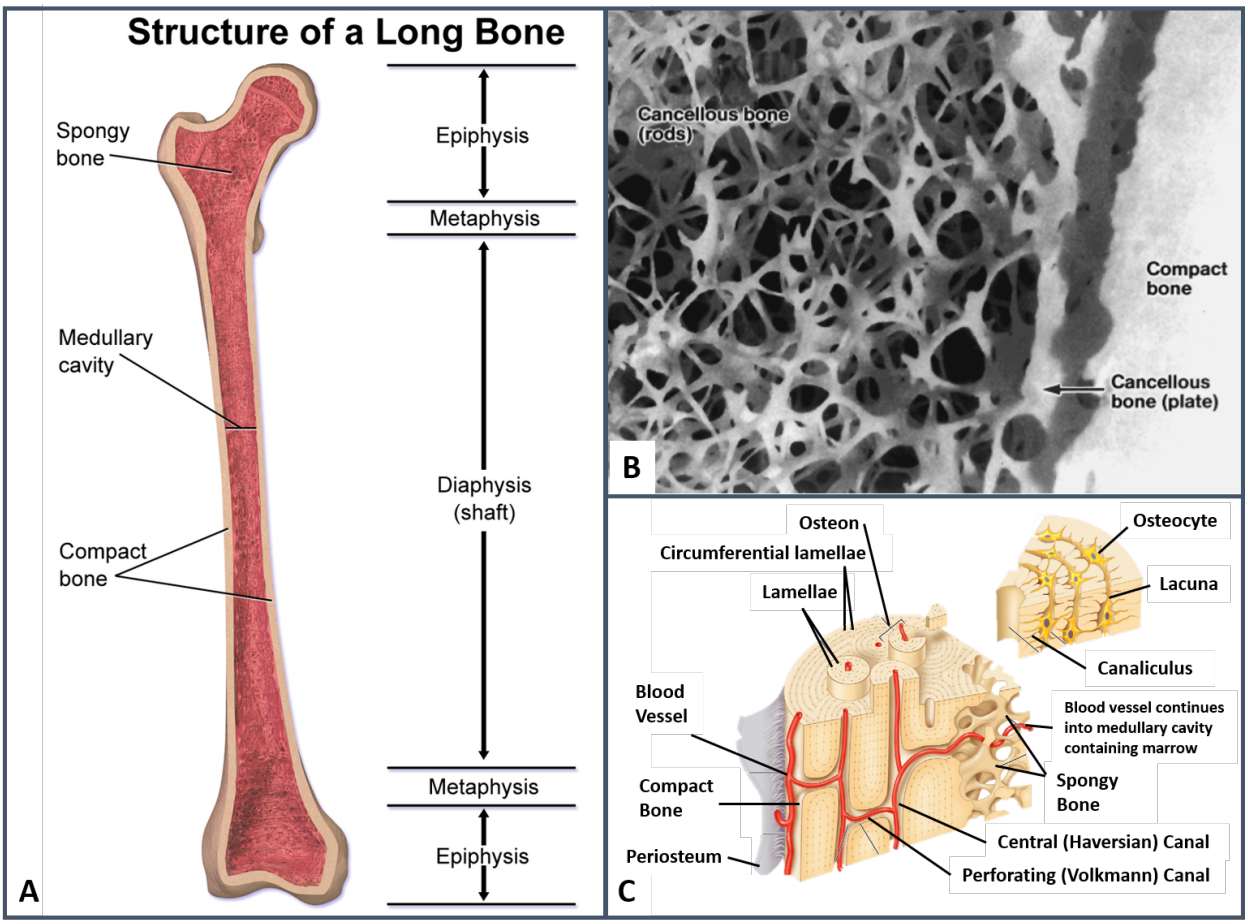

Figure 1: Diagram of the femur, an example of a long bone (A) [4], Photograph of trabecular and cortical bone from the proximal tibia (B) [5], C) Cortical bone microstructure (Source: Copyright © 2006 Pearson Education, Inc., publishing as Benjamin Cummings)

1.2 Bone (re)modeling and cortical porosity

At the micro-length scale, cortical bone exhibits a complex network responsible for the transport of blood and nutrients. This network is made of Haversian canals, which are central canals oriented along the primary axis of bone, and Volksmann's canals, which are oriented perpendicular to the primary axis of bone (Fig. 1C). On average, Haversian canals range from 50 to 150 μm, making them the largest contributor to bone porosity [20]. Several other microscopic pores such as lacunae, or small pockets containing osteocytes, also contribute to cortical bone porosity [20, 21]. Chappard and colleagues classified pores into five groups depending on their size: small (7–95 μm), intermediate (95–180 μm), large (180–270 μm), extra-large (270–360 μm), and giant pores (>360 μm) [22]. The complex pore network found

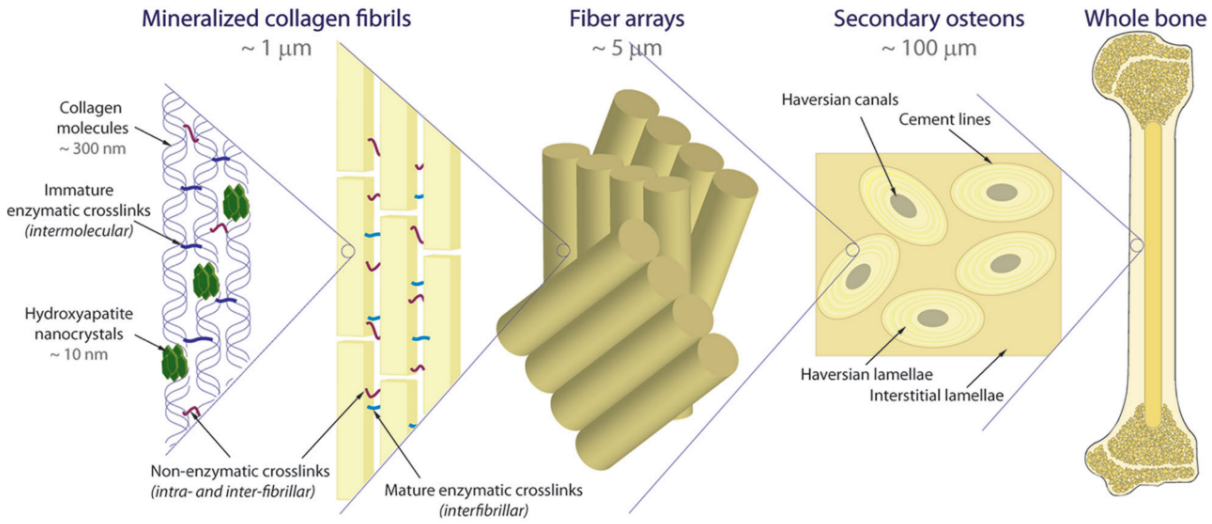

Figure 2: Hierarchical structure of human cortical bone. Schematic at micro- (~ 1 μm), meso- (~ 5 μm), and macroscale (~ 100 μm) cortical bone structure [6]. Copyright 2011, National Academy of Sciences

within cortical bone is important because of its role in blood and nutrient transport, crack prevention, and mechanosensation [23].

The size, shape and structure of cortical bone is constantly changing and is the result of two processes: modeling and remodeling. Modeling creates new bone and occurs predominately during childhood and adolescence, while remodeling is a lifelong process where bone renews itself. According to the mechanostat theory, (re)modeling is driven by osteocytes, which are bone cells that sense changes in the local mechanical environment [24]. For example, when the local strain exceeds a certain threshold and causes bone damage, osteoclast and osteoblast cells assemble to form a basic multicellular unit. Next, a cutting cone zone is made by osteoclasts that remove old or damaged bone. The cutting cone widens the cylindrical channel, temporarily increasing pore size. A reversal zone follows, and finally, a closing cone forms new bone (osteons) with osteoblasts, returning the cylindrical channel back to a healthy pore size (Fig. 3). It is worth mentioning that osteonal (re)modelling cannot be studied using rodent models as they have predominantly primary (plexiform and woven) bone, not secondary (osteonal, Haversion systems) bone [25].

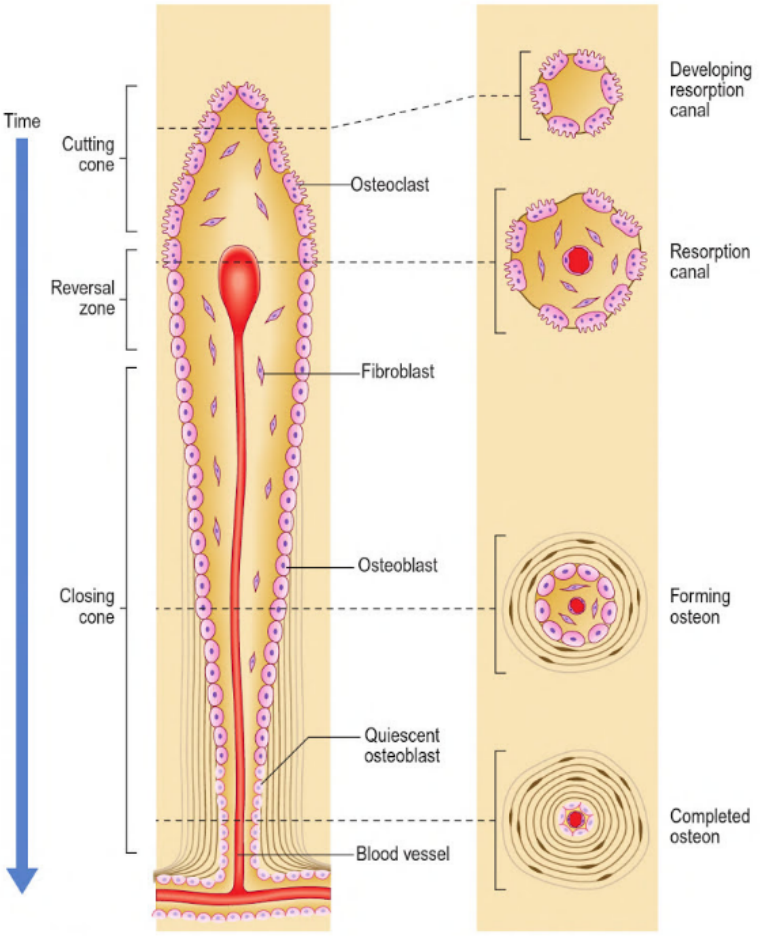

Figure 3: Timeline of longitudinal and cross-sectional view of the remodeling process [7]. The cutting cone is formed by osteoclast cells resorbing the bone matrix into a cylindrical channel. After the reversal zone, the closing cone is formed by osteoblasts reforming bone by building new osteonal lamellae. The image on the right illustrates a cross-section through each of the zones.

1.3 Clinical motivation: cortical thinning and osteoporotic fractures

As we age, an imbalance and uncoupling in the remodeling process deteriorates the intracortical network and subsequently weakens our bones [26, 27]. Excessive resorption increases the average Haversian canal diameter leading to an increase in porosity and "trabecularization" of the cortex [28, 29]. While pore size and porosity increase, there is a simultaneous decrease in pore number, meaning that pores coalesce, and additionally, that the total bone area containing pores decreases. The decrease in cortical bone area during aging is known

as cortical thinning (Fig. 4). This twofold microstructural degradation of cortical bone is one of main indications of osteoporosis.

Impaired mechanical strength, structural degradation, and deficient material composition point to a loss of bone quality that leads to osteoporosis. As bone quality and strength decrease, patients become at high risk for osteoporotic fractures during a fall or other atypical loading conditions. Among these fractures, femoral neck fractures (or cervical hip fractures) lead to mortality rates as high as 27% [30, 31]. Further, the costs associated with osteoporotic fractures are predicted to increase from $35 billion in 1990 to $130 billion by 2050 due to the world's aging population [32, 31, 33].

1.3.1 Current clinical challenges for diagnosis

Dual-energy x-ray absorptiometry (DEXA) is the current gold standard for measuring apparent bone mineral density for diagnosing osteoporosis. However, only 10 - 44% of bone fractures can be explained by low BMD (Stone et al., 2003). DEXA only provides an aggregate measure of bone quality; it does not include structural properties known to contribute to bone strength. For example, DEXA does not assess cortical thinning or cortical porosity. Macroscopic measurements also cannot fully explain bone remodeling and damage, which depend on the local mechanical behavior. As a result, DEXA continues to be an imperfect predictor of osteoporotic fracture risk.

1.4 Significance and open questions

Significant personal, financial, and societal burdens due to osteoporotic fractures are considered to likely increase in the future, necessitating improved techniques for prevention, treatment, and rehabilitation of bone disease. Macro-level tests like DEXA cannot predict the underlying mechanisms that lead to femoral neck fractures. Thus, high resolution imaging techniques paired with mechanical testing and simulations are needed to better understand how the cortical pore network distributes load and which microstructural properties are the best indicators of fracture risk. These improvements, coupled with advances in in-vivo imaging capabilities might one day lead to better diagnostic tools for high-risk patients.

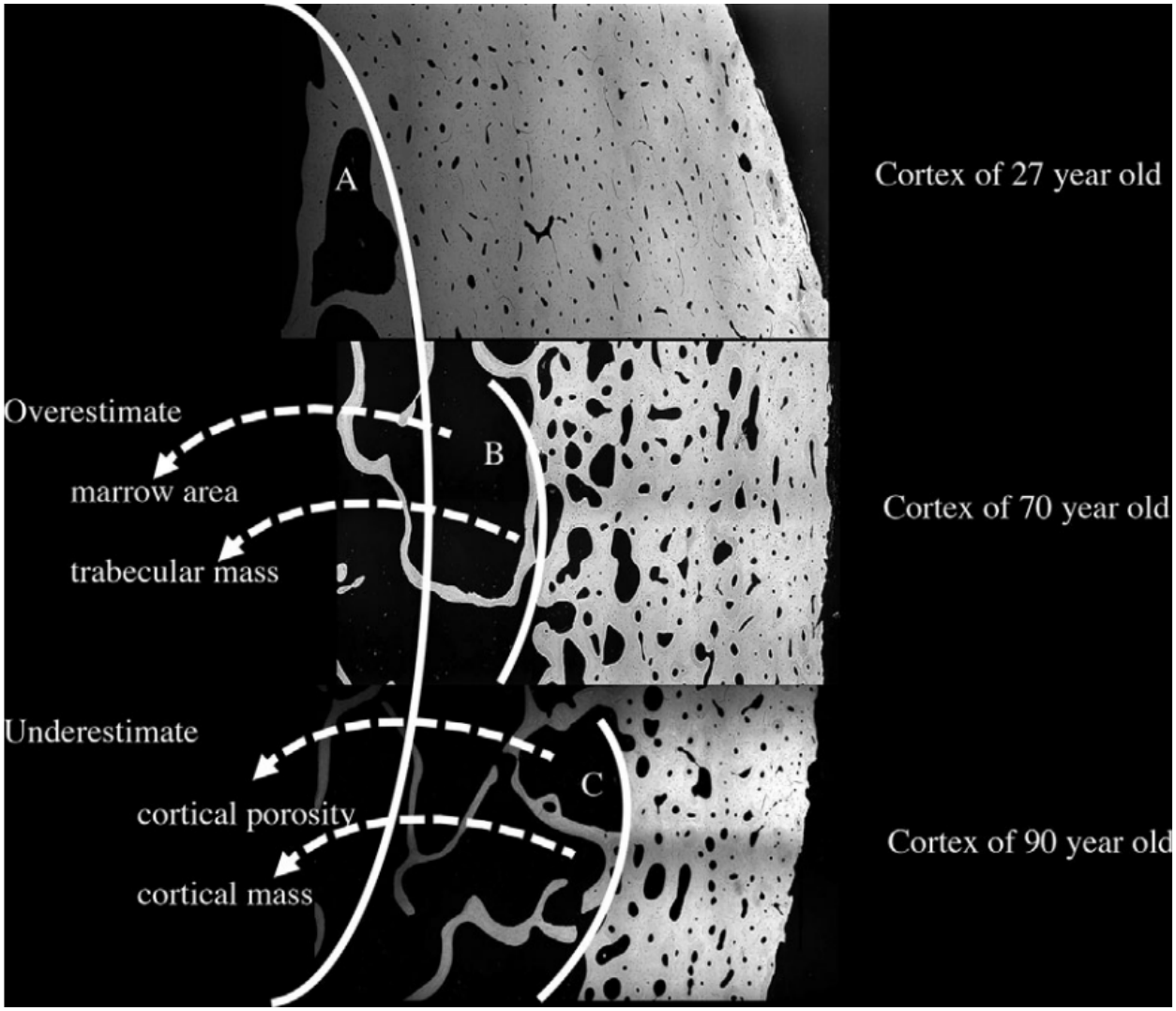

Figure 4: Cortical thinning as a result of an imbalance in the remodeling process. The endosteal surface is marked by the white line A of a specimen from a 27-year-old. This is the original delineation of the interface between cortical and trabecular bone. As the cortical bone thins, the interface appears to recede (white line B in a 70-year-old specimen and white line C in a 90-year-old specimen). [8]

Improved diagnosis, as well as more effective preventative measures, are critical in reducing the incidence of osteoporotic fractures. Exercise is known to improve overall bone health, but targeted exercise interventions in the femoral neck have been less successful. Calculating the normal level of strain in the femoral neck and how that relates to remodeling will help create new exercise interventions that cause bone adaptation and subsequent strengthening of the femoral neck. These interventions may help prevent fractures due to falls or other atypical loading conditions in osteoporotic patients.

1.5 Thesis outline

The overall objectives of this thesis were twofold. First, we aimed to quantify the physiological level of strain in the proximal femur during regular activity and characterize the resulting mechanical environment. Second, we aimed to perform a digital volume correlation (DVC) error analysis on cortical bone, and perform mechanical testing to develop a protocol for loading bone and measuring local strains using DVC. To achieve the two objectives, the study was divided into the following aims:

1. Characterize the role of muscles on proximal femur strain distributions in FE models
    - Run 3D subject-specific FE models for three loading configurations: [1] hip joint force, gluteus medius, gluteus maximus, gluteus minimus, vasti, iliopsoas, and several other smaller hip spanning muscles, [2] hip joint, gluteus medius, gluteus minimus, and the iliopsoas, and [3] hip joint force only
    - Analyze the maximum and minimum principal strains and their orientations in four quadrants of eight sections of the femur
2. Optimize Digital Volume Correlation (DVC) for cortical bone samples from the femur
    - Perform a DVC error analysis on cortical bone from three different regions of the femur
    - Perform mechanical testing on cortical bone samples to develop loaded DVC protocol

CHAPTER 2

ROLE OF MUSCLE FORCES ON PROXIMAL FEMUR STRAIN DISTRIBUTIONS

2.1 Summary

Femoral neck fractures are frequent causes of disability or death, and their incidence and associated costs are expected to increase rapidly due to the world's aging population. Establishing a baseline for daily loading of the femoral neck is critical to understand the incidence of femoral neck fractures and develop preventative measures. However, there remain several methods used to model physiological loading of the femur, and discussion persists whether the femoral neck is loaded predominantly in bending or compression. We used 3D subject-specific (n=20) finite element (FE) models to compare principal strains and their orientations for three loading configurations: [1] hip joint force, gluteus medius, gluteus maximus, gluteus minimus, vasti, iliopsoas, and several other smaller hip spanning muscles, [2] hip joint, gluteus medius, gluteus minimus, and the iliopsoas, and [3] hip joint force only. The principal strains and their orientations were compared in four quadrants of 8 regions (proximal femoral neck, middle femoral neck, distal femoral neck, pertrochanter, subtrochanter, proximal diaphysis, middle diaphysis, and distal diaphysis) during walking. As predicted by Wolff's Trajectorial Theory, the presence of large tensile and compressive principal strains in the hip joint force only model indicated a bending moment throughout the femoral neck. However, the model including muscle forces resulted in significantly decreased strain magnitudes, as well as compression in all four quadrants, suggesting that the inclusion of muscle forces decreased the bending moment observed in a hip joint force only model. Further, the model with muscle forces resulted in a more homogeneous strain distribution. In the pertrochanter, including muscle forces increased the compressive and tensile strains. Both the femoral neck and pertrochanter were more sensitive to changes in their compressive, rather than tensile, orientation, and in the femoral neck, the changes in strain orientation followed similar patterns as the changes in strain magnitude. Together, these findings indicate that including muscle forces result in more physiologically accurate FE models, and they support the hypothesis that FE models used to calculate femoral neck strains during walking should not neglect the contribution of muscle forces. Model files used for calculating femoral neck strains and orientations are available at: uitbl.mechse.illinois.edu/downloads.

2.2 Literature review

2.2.1 Physiological Loading in the Femur

Exercise has been shown to be an inexpensive and promising means for encouraging bone adaptation via muscle-driven loading of bone [34, 35, 36, 37, 38], but targeted adaptation of the femoral neck has been less successful. In order to identify activities that may encourage bone remodeling and therefore prevent femoral neck fractures, it is critical to understand femoral neck loading during regular activity and quantify the resulting mechanical environment [39].

One of the first studies on daily loading of the femoral neck was by Julius Wolff in 1892 [40, 41] in which he posited two theories related to bone adaptation: (1) Wolff's Law of bone formation, which suggests that bone will form based on the forces applied and (2) Wolff's Trajectorial Theory. The latter, founded on Ward's and Von Meyer's models (Fig. 5B), simplifies the femur as a curved cantilever beam with only the hip joint force acting at the femoral head (Fig. 5A). This loading results in bending of the proximal femur, leading to compression on the medial (or inferior) side of the femoral neck and tension on the lateral (superior) side. Wolff validated the Trajectorial Theory by citing the neck shaft angle, graphic static requirements, and most famously, that the trabecular structures in the femoral neck aligned with the tensile and compressive stresses (Fig. 5C) [40, 41, 9].

However, the mechanical state of physiologically loaded bone, and its consequence on adaptation, has since been re-evaluated. Finite element (FE) and numerical studies have shown that most of the proximal femur is loaded axially in compression when ligament and/or muscle forces were included with the hip joint force. Taylor and colleagues first demonstrated that the femur is predominantly loaded in compression and not bending when muscle forces are included in an FE model [42]. Using first a numerical model and an FE model in a subsequent study, Duda et al added evidence that muscle forces play a substantial role in balancing loads in the femur and that bending moments decreased when muscle forces were included (Fig. 6). Most recently, Rudman and colleagues used a 2D plane stress FE model to show that there are predominantly compressive stresses in the proximal femur when capsular ligament forces were included (Fig. 7) [11].

Several of these studies noted that decreased bending caused internal forces and strains to decrease, resulting in more physiologically representative loads according to Frost's mechanostat theory [43, 10, 42]. These computational and numerical findings are supported by Simoes

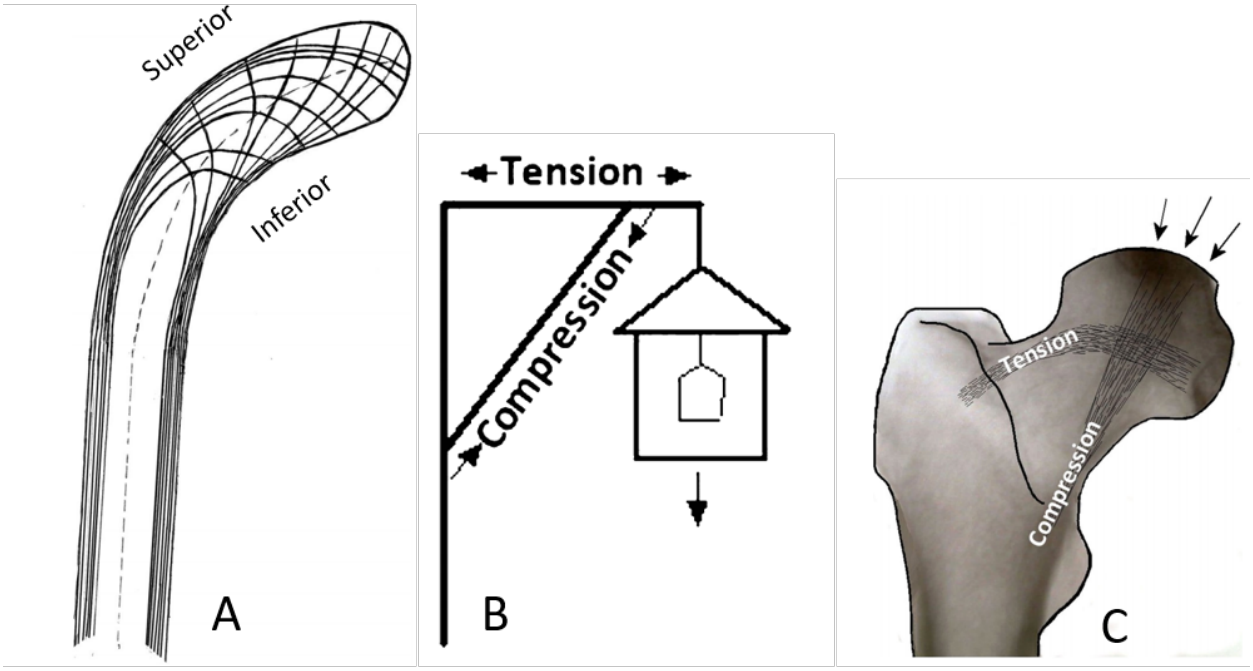

Figure 5: Stress trajectories predicted by Culmann within a curved crane (A), Representation of Ward's concept relating the structure of a gas-lamp to that of trabecular structures within the femoral neck (B), and Diagram of the compressive and tensile trajectories in the femoral neck (C) [9].

et al, who showed experimentally using strain gauges and a synthetic femur that strains decreased when muscle forces were applied in addition to a joint reaction force [44].

More generally, Sverdlova and colleagues have recently found evidence that a predominant state of compression is more physiologically plausible in the femur because biological systems are optimized by evenly distributing the amount of unloaded material to minimize bending [45]. In theory, these mechanisms create more lightweight and efficient structures since bone is stronger in compression instead of tension.

In summary, including muscle forces in simulations of daily activity in the femur result in different mechanical states than when muscle forces are not included. While muscle forces decrease bending and reduce internal loads, it is important to note that some degree of bending remains in the femur during physiological conditions. However, bending caused by a model with only a joint reaction force is not physiologically representative of the femur during daily activity.

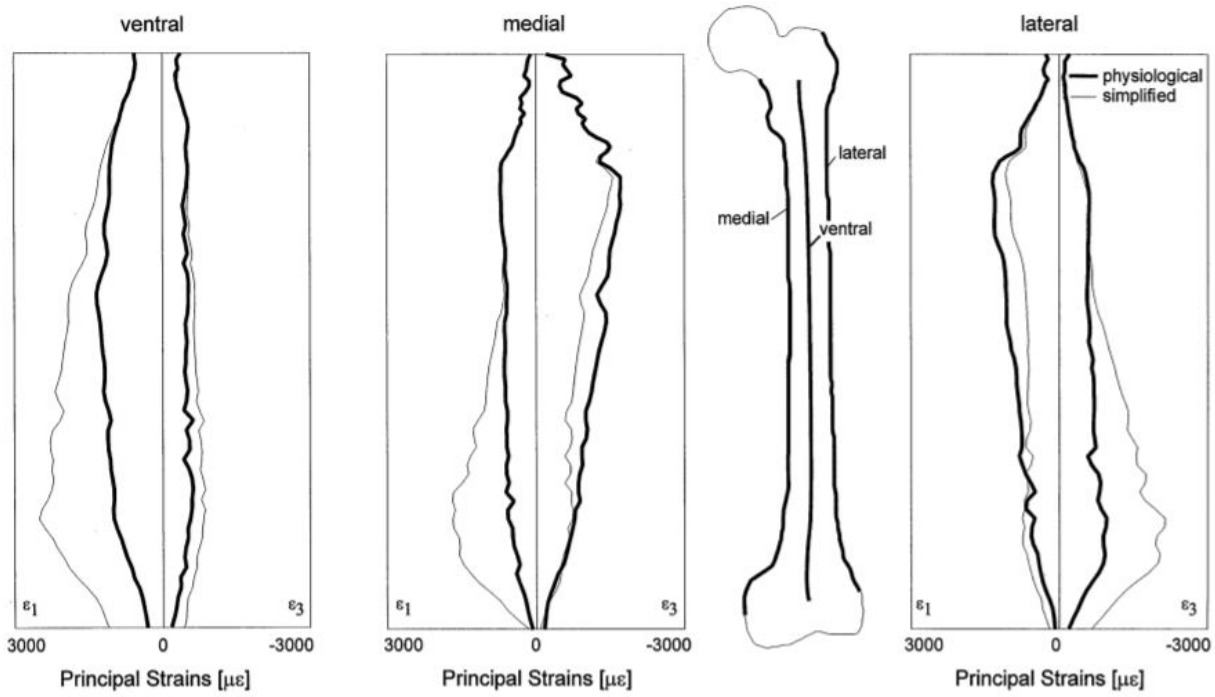

Figure 6: Minimum and maximum principal strains along the ventral, medial, and lateral sides of the human femur at 45% of the gate cycle. The dark line includes all thigh muscles, while the light lines only include the hip contact, abductors, and ilio-tibial band [10].

2.3 Motivation

Despite recent publications showing the effect of including muscle forces, many studies continue to only include the hip joint force acting on the femoral head when modelling daily activity in the femur. Often, the rationale for this simplification is that muscle forces are difficult to quantify and apply experimentally or computationally.

While some studies have evaluated the effect of different configurations of muscle and hip forces on diaphyseal strains, these studies did not evaluate the femoral neck region. Further, no study has directly compared strain distributions between subject-specific femur FE models with and without muscle forces. Thus, it remains unclear whether including muscle forces results in **significant** differences in femoral neck strain during physiological tasks such as walking.

Understanding whether computational predictions of bone strain during locomotion should include both hip and muscle forces is needed to develop targeted exercise interventions designed to prevent femoral neck fractures. Further, loading models of rodent long bones have shown significant increases in bone area in regions of compression compared to tension

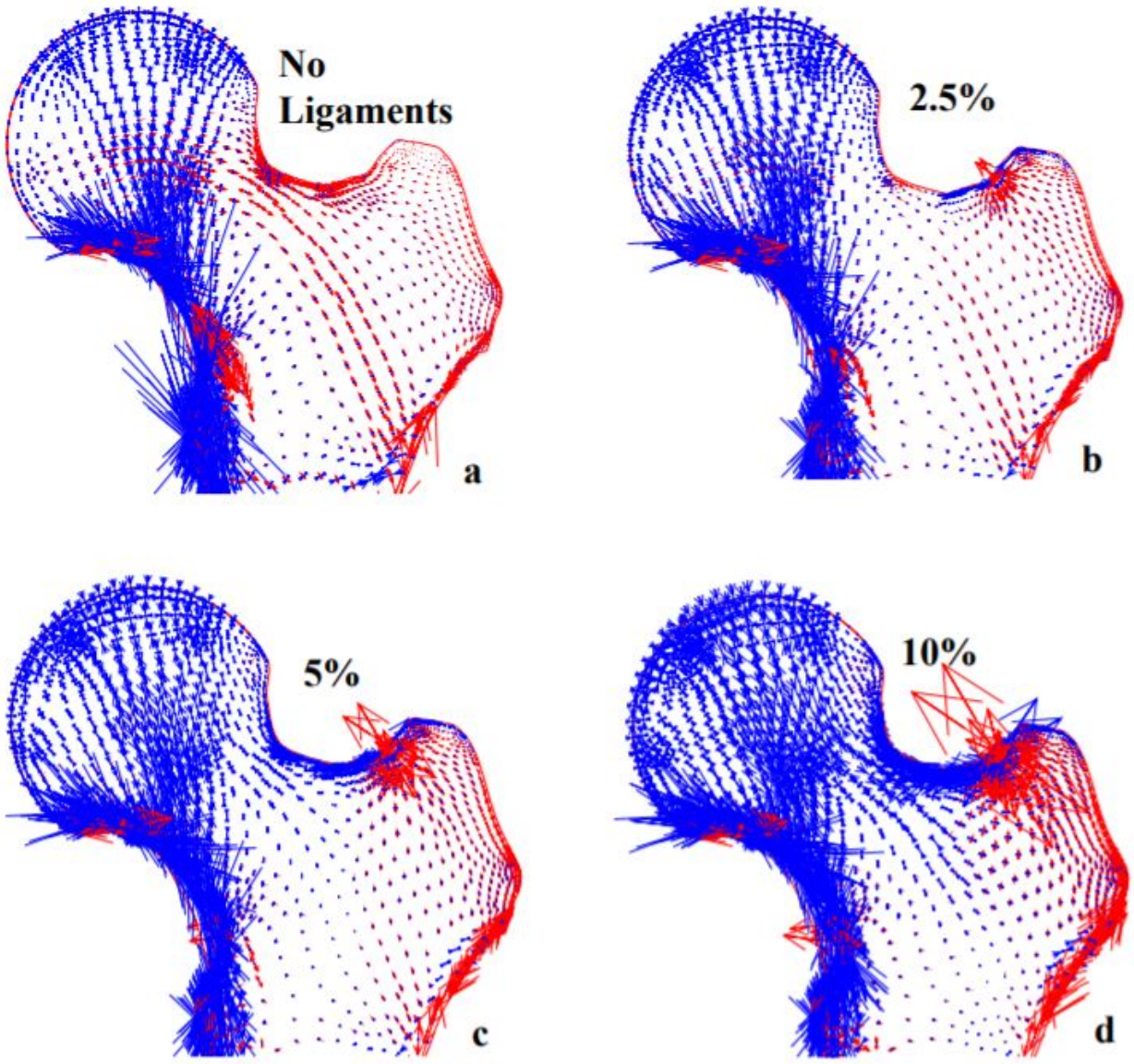

Figure 7: The distribution of maximum (red) and minimum (blue) principal stresses as tension in the spring elements is increased. The length and direction of the arrows show the relative magnitude and direction of stress [11].

[46], supporting the importance of characterizing the local strain environment. Finally, physiologically accurate strain distributions in the proximal femur are relevant in pre-clinical testing of hip implants and the design of internal fixation devices.

Table 1: List of peer-reviewed studies investigating the effect of muscle forces on computational and experimental strains in the femur.

Paper	Study Type	Loading Conditions	Limitations
Taylor 1996	FE model	1) JRF, abductors, 2) JRF, abductors, IT tract 3) JRF, abductors, IT tract, iliopsoas 4) JRF, abductors, IT tract, iliopsoas	n = 1, not subject specific forces or model, did not compare to a no muscle condition
Duda 1997	Quasi-Static Calculations	1) No muscles active 2) Abductors (gluteus maximus, gluteus medius, and gluteus minimus) 3) All muscles according to Brand et al (1986)	n = 1, not subject specific forces or model
Duda 1998	FE model	1) JRF, all muscles 2) JRF, abductors, IT band, adductors, vasti, gastrocnemi 3) JRF, abductors, IT band, adductors, vasti 4) JRF, abductors, IT band, adductors 5: JRF, abductors, IT band	n = 1, not subject specific forces or model, did not analyze femoral neck, did not compare to a no muscle condition
Simoes 2000	Experimental	1) JRF 2) JRF, abductors 3) JRF, abductors, iliopsoas, vastus lateralis	Synthetic composite femur, n =1, only one strain gauge on femoral neck
Rudman 2006	FE model	1) Two-legged stance no ligaments 2) Two-legged stance 2.5% strain 3) Two-legged stance 5% strain 4) Two-legged stance 10% strain 5) One-legged stance 5% strain	2D FE model, n=1, not subject specific forces or model

2.4 Study aims

The aim of this study was to use 3D subject-specific finite-element models to compare principal strains and their orientations for three loading configurations: [1] hip joint force, gluteus medius, gluteus maximus, gluteus minimus, vasti, iliopsoas, and several other smaller hip spanning muscles , [2] hip joint, gluteus medius, gluteus minimus, and the iliopsoas, and [3] hip joint force only (Table 2). Strain was measured because it has been suggested as a likely mechanical stimulus for bone (re)modeling [47, 48, 49, 50, 51]. Principal orientation was measured because it helps gauge trabecular bone orientation [52, 53, 54, 55] and patterns of mechanoadaptation [56]. The principal strains and their orientations were compared in 32 sections of the femur during walking. We hypothesized that the model with the hip joint and muscle forces would show significantly smaller principal strains and significantly different principal strain orientations.

2.5 Material and Methods

2.5.1 Gait Experiments, Computed Tomography Imaging, and Musculoskeletal Modeling

A subset of data (n=20) from a previously published study were analyzed [39]. To summarize, postmenopausal women (ages 60-74 years) with no history of lower-extremity fractures, drug therapy, and musculoskeletal disease were recruited and asked to walk at a self-selected speed. Kinematic and ground reaction force data were collected using a nine-camera motion capture system and three in-ground force plates, respectively. A generic musculoskeletal model (OpenSim) was scaled to each participant and inverse kinematic analysis was used to calculate the joint angles, which were then filtered, differentiated, and combined with ground reaction force data to calculate the joint torques using inverse dynamics. Static optimization was used to calculate muscle forces. Computed tomography (CT) images were acquired with an isotropic voxel size of 0.5mm, and a calibration phantom was used to convert CT attenuation data into apparent Young's modulus.

2.5.2 Finite Element Modeling

The femur was segmented from the CT images (Amira v5.3; Thermo Scientific, Hillsboro, OR, USA) and discretized into quadratic tetrahedral elements (Abaqus v6.11; Simulia, Paris, France). The FE model assumed spatially heterogeneous, isotropic Young's moduli and a Poisson's ratio of 0.3 [57, 58]. The hip joint force was applied as a point vector on the femoral head and muscle forces were applied at the node closest to the muscle attachment point and oriented along the muscle force line-of-action. The distal end of the femur was constrained against all displacements, and axial springs were applied to the femoral head to represent the hip capsule.

We developed three different models from this data: [1] hip joint force, gluteus medius, gluteus maximus, gluteus minimus, vasti, iliopsoas, and several other smaller hip spanning muscles, [2] hip joint, gluteus medius, gluteus minimus, and the iliopsoas, and [3] hip joint force only (Table 2, Fig. 8A). The lateral/superior, medial/inferior, anterior, and posterior quadrants of 8 regions (proximal femoral neck, middle femoral neck, distal femoral neck, pertrochanter, subtrochanter, proximal diaphysis, middle diaphysis, and distal diaphysis)

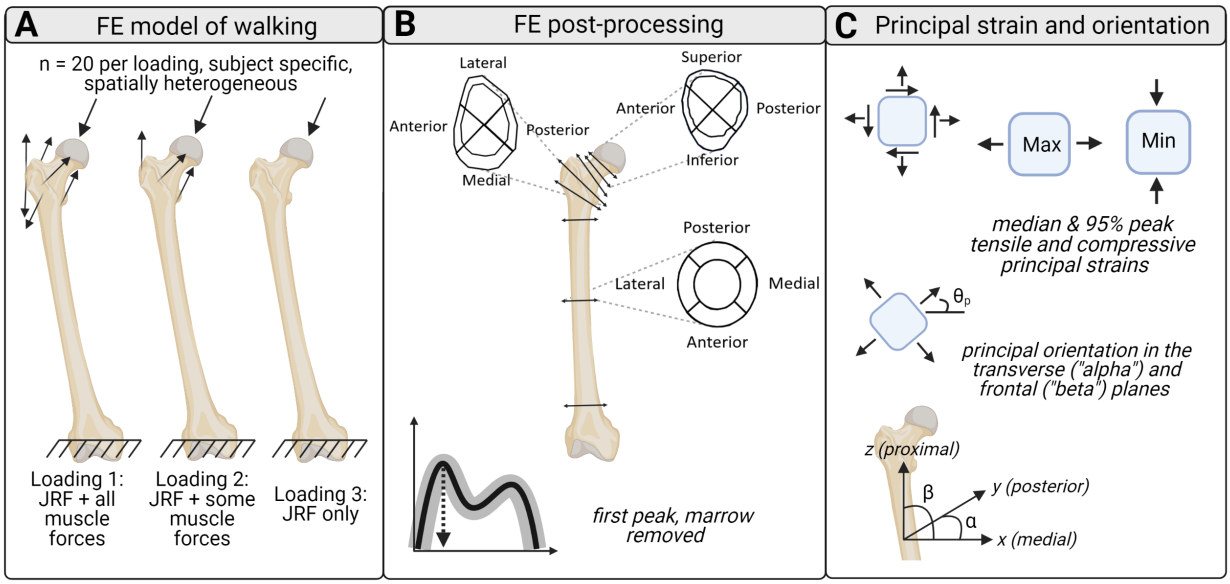

Figure 8: Subject-specific (n=20) FE models (A) of three models were divided into 32 regions (B), and their principal strains and orientations were calculated (C). Maximum and minimum principal strains are referred to as tensile and compressive strains, respectively, in this study.

were identified based on anatomical landmarks in the solid models of each subject (Fig. 8B).

2.5.3 Principal Strain and Principal Orientation Calculations

All principal strain and orientation calculations were performed in MATLAB (vR2018b; MathWorks, Natick, MA, USA). First, elements in the FE model with Young's moduli below 1000 MPa [59] were assumed to be bone marrow and discarded from the analysis. The time point corresponding to maximum strains during the first half of the stance phase was used for all analyses. The strain tensor for each remaining element was assembled according to Equation 1:

$$\varepsilon_{ij} = \begin{bmatrix} \varepsilon_{11} & \varepsilon_{12} & \varepsilon_{13} \\ \varepsilon_{21} & \varepsilon_{22} & \varepsilon_{23} \\ \varepsilon_{31} & \varepsilon_{32} & \varepsilon_{33} \end{bmatrix} \tag{1}$$

where ε_{ij} is the strain in each coordinate direction.

Table 2: Loading conditions used to evaluate contributions of muscle forces to principal strains in the proximal femur.

	Joint reaction force	*Gluteus medius*	*Gluteus minimus*	*Iliopsoas (psoas, iliacus)*	*Gluteus maximus*	*Adductors (brevis, longus, magnus)*	*Quadratus femoris*	*Vastus medialis, lateralis and intermedius*	*Biceps femoris short*	*Gemelli*	*Pectineus*	*Piriformis*
Loading 1	✓	✓	✓	✓	✓	✓	✓	✓	✓	✓	✓	✓
Loading 2	✓	✓	✓	✓								
Loading 3	✓											

Next, the maximum and minimum principal strains were calculated according to Equations 2, 3 and 4:

$$Det \left| \varepsilon_{ij} - \lambda I \right| = 0 \tag{2}$$

$$\varepsilon_1 = max \left(\lambda_1, \lambda_2, \lambda_3 \right) \tag{3}$$

$$\varepsilon_3 = min \left(\lambda_1, \lambda_2, \lambda_3 \right) \tag{4}$$

where $\left(\lambda_1, \lambda_2, \lambda_3 \right)$ are the eigenvalues of the strain tensor.

The elements corresponding to the median and 95th percentile principal strain in each region were calculated (Fig. 8C). The median principal strain of all twenty subjects was then calculated for each region and for all three loading conditions. In this study, maximum and minimum principle strains are synonymous with tensile and compressive strains, respectively.

We calculated the principal strain orientation using the eigenvector of the tensile and compressive principal strains (Equations [5,6]). The x, y, and z directions of the principal orientation correspond to the medial, posterior, and proximal anatomical directions in the FE model, respectively. From these anatomical directions, we calculated 2 angles: alpha (y/x, in the transverse plane) and beta (z/x, in the coronal/frontal plane) (Fig. 8D).

$$\left|A - \lambda I\right| v = 0 \tag{5}$$

$$v_{\varepsilon 3/\varepsilon 1} = \begin{bmatrix} v_x \\ v_y \\ v_z \end{bmatrix} \tag{6}$$

2.5.4 Statistical Analysis

Normality was checked using a one-sample Kolmogorov-Smirnov test and because all data were found to be non-normally distributed, the results were presented as medians and median absolute deviations (Table 3). We calculated statistically significant differences between the "all muscle" group (Loading 1) and the other two groups (Loading 2 and 3) using a linear mixed-effects model at an alpha level of 0.05 according to Equation 7,

$$Linear\,mixed\,effects\,model\ =\ Strain\ \sim\ Condition\ +\Big(\,1\mid Subject\Big) \tag{7}$$

where strain is either principal strain or principal orientation (MATLAB R2018b; MathWorks, Natick, MA, USA).

2.6 Results

For all analyses, the maximum principal strains were in tension and minimum principal strains were in compression. These values are herein referred to as the median tensile and compressive strains, respectively. Note that median refers to the median values of all subjects. Overall, the effect of different loading conditions on tensile and compressive strains was similar for all three regions of the femoral neck. Therefore, the middle neck is reported

Table 3: Median (median absolute deviation) Tensile and Compressive Strains ($\mu\varepsilon$) for 3 loading conditions in four quadrants of the middle femoral neck and pertrochanter. The median percent change is reported, not percent change of medians. *p<0.05, **p<0.01, *** p<0.001

		Median Tensile Strain ($\mu\varepsilon$)			Median Compressive Strain ($\mu\varepsilon$)		
		Loading 1: "All muscle + JRF"	Loading 2: "Some muscle + JRF"	Loading 3: "JRF only"	Loading 1: "All muscle + JRF"	Loading 2: "Some muscle + JRF"	Loading 3: "JRF only"
Middle Neck							
Superior	Median	601 (198)	670 (179)	**1440 (175)*****	-854 (272)	-845 (251)	**-519 (107)*****
	% Change		20.5%	140.7%		-6.4%	-43.1%
Posterior	Median	565 (128)	610 (127)	**836 (191)*****	-1405 (275)	**-1528 (320)***	**-996 (234)*****
	% Change		9.1%	62.5%		10.9%	-26.9%
Inferior	Median	516 (94)	**544 (102)***	**679 (113)*****	-1608 (275)	**-1690 (293)***	**-1989 (316)*****
	% Change		5.3%	25.9%		4.7%	22.2%
Anterior	Median	408 (93)	**469 (130)****	**662 (118)*****	-946 (146)	-914 (174)	**-1276 (270)*****
	% Change		20.2%	41.7%		0.7%	41.3%
Pertrochanter							
Lateral	Median	1447 (258)	1424 (240)	**439 (116)*****	-766 (140)	-766 (119)	**-294 (65)*****
	% Change		-1.3%	-70.9%		-1.4%	-60.3%
Posterior	Median	613 (154)	650 (189)	**481 (91)****	-708 (161)	**-769 (172)***	**-607 (117)*****
	% Change		4.8%	-19%		12.5%	-19.8%
Medial	Median	577 (104)	**645 (76)*****	**561 (82)****	-1414 (225)	**-1562 (211)*****	**-1396 (220)****
	% Change		10.8%	-3%		8.3%	-2.4%
Anterior	Median	856 (240)	**1019 (255)***	**478 (123)*****	-996 (228)	-1056 (223)	**-581 (108)*****
	% Change		15.4%	-42.6%		6.1%	-39.7%

and discussed within the main body of this thesis. Results for the subtrochanteric and pertrochanteric regions were also similar. Further, only the median is reported in the main text because the 95th percentile strain exhibited similar patterns. The full datasets are included in the Appendix of this chapter.

2.6.1 Principal Strain

Relative to loading 1 (all muscle + JRF), loading 3 (JRF only) significantly increased the tensile strain in all four quadrants of the middle neck during walking (p<0.001). The superior quadrant had the largest change in tensile strain, +140.7% (p<0.001), while the inferior quadrant had the smallest change in tensile strain, +25.9% (p<0.001). The inclusion of some muscles + JRF (Loading 2) resulted in similar trends but in fewer regions and to a lesser degree. Tensile strains were significantly increased in the inferior (+5.3%, p=0.038) and anterior (+20.2%, p=0.0092) quadrants (Table 3, Fig. 9).

The effect of muscle forces on compressive strains was more variable. Models using only the joint reaction force decreased the compressive strains in the superior and posterior quadrants

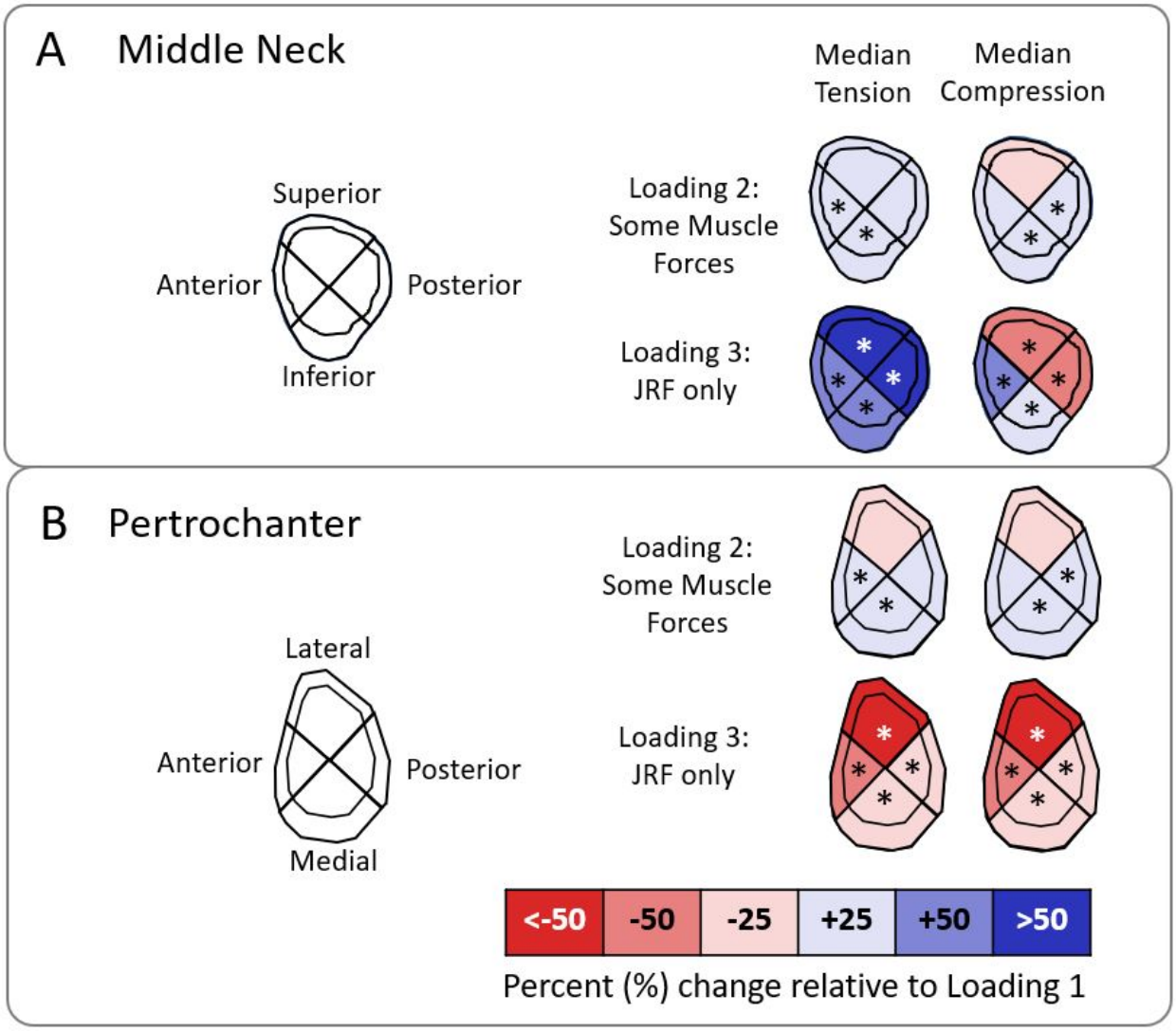

Figure 9: Percent change in loading conditions 2 and 3 relative to loading condition 1 for median tensile and compressive strains in four quadrants of the middle femoral neck (A) and pertrochanter (B). *p<0.05

of the middle neck (p<0.001) and increased the compressive strains in the inferior and anterior quadrants (p<0.001) compared to those models using all muscles + the JRF. Similar to the effect on tensile strains, the superior quadrant had the largest change in compressive strain, -43.1% ($p < 0.001$), while the inferior quadrant had the smallest change in compressive strain, +22.2% (p<0.001). Loading 2 (some muscles + JRF) increased compressive strains in the posterior (+10.9%, p=0.019) and inferior (+4.7%, p=0.040) quadrants (Table 3, Fig. 9).

Relative to loading 1, both the compressive and tensile strains in all four quadrants of

the pertrochanter were decreased in models using only the JRF ($p<0.0074$). The lateral quadrant had the largest decrease in tensile and compressive strain, -70.9% and -60.3%, respectively, while the medial quadrant had the smallest decrease in tensile and compressive strain, -3% and -2.4%, respectively. Conversely, loading 2 increased the tensile strain in the medial and anterior quadrants ($p<0.015$), and increased the compressive strain in the posterior and medial quadrants ($p<0.038$). The anterior and posterior quadrants had the largest changes in tensile and compressive principal strain, +15.4% and +12.5%, respectively (Table 3, Fig. 9).

The compressive strains for loading 1 and 2 tended to be greater in magnitude than the tensile strains in the femoral neck ($\left|-\varepsilon_3\right| > \left|\varepsilon_1\right|$), signaling a dominant state of compression (Table 3). Conversely, for loading 3 the tensile strain in the superior (1440 $\mu\varepsilon$) and posterior (836 $\mu\varepsilon$) quadrants was larger or comparable to the compressive strain (-519 and -996 $\mu\varepsilon$), showing more balance between tension and compression (Table 3). For all 3 loading conditions in the pertrochanter, the tensile strain was consistently larger than the compressive strain in the lateral quadrant, and the compressive strain was larger than the tensile strain in the posterior, medial, and anterior quadrants.

As muscle forces were progressively included from loading 3 to 1, the strain range (max - min) decreased across all four quadrants in the middle femoral neck (778 to 201 to 193 $\mu\varepsilon$ for tensile strains and 1470 to 845 to 754 $\mu\varepsilon$ for compressive strains), resulting in a more homogeneous strain distribution. The same pattern was evident from loading 3 to 1 for compressive strain in the pertrochanter (1102 to 796 to 706 $\mu\varepsilon$). However, the pertrochanteric tensile strain became less homogeneous as muscle forces were added (122 to 779 to 870 $\mu\varepsilon$).

2.6.2 Principal Orientation

Relative to loading 1 (all muscle + JRF), loading 3 (JRF only) changed the compressive principal strain vector in the superior (+117.3%, $p=0.0037$) and posterior quadrants (+42.1%, $p<0.001$) of the middle neck. Loading 3 significantly increased the tensile strain orientation in the anterior quadrant (+93.5%, $p=0.0032$). The inferior quadrant had the smallest changes for loading 2 and 3 ($< \pm 2\%$, $p>0.05$). For all quadrants in the middle neck, loading 3 had a smaller median absolute deviation than loading 1 for both tensile and compressive orientation (Table 4,Fig. 10).

Within the pertrochanter, relative to loading 1 (all muscle + JRF), loading 3 (JRF only)

Table 4: Median (median absolute deviation) Tensile and Compressive Beta Orientation (°) for 3 loading conditions in four quadrants of the middle femoral neck and pertrochanter. The median percent change is reported, not percent change of medians. *p<0.05, **p<0.01, *** p<0.001

		Tensile Orientation Beta (°)			Compressive Orientation Beta (°)		
		Loading 1: "All muscle + JRF"	Loading 2: "Some muscle + JRF"	Loading 3: "JRF only"	Loading 1: "All muscle + JRF"	Loading 2: "Some muscle + JRF"	Loading 3: "JRF only"
Middle Neck							
Superior	Median	36.5 (8.7)	39.8 (11.3)	26.7 (6.1)	54.1 (43.2)	47.8 (26)	**116.1 (9.3)****
	% Change		-4.7	-27.1		21.6	117.3
Posterior	Median	119.9 (57.2)	100.1 (60.3)	27.8 (20.7)	70.5 (11.8)	67.7 (4.8)	**99.5 (3.4)*****
	% Change		-20	-77.4		0.7	42.1
Inferior	Median	152.3 (10)	144.5 (28.6)	153.7 (6.1)	66.2 (10.1)	71.1 (7.1)	65.7 (8.1)
	% Change		-0.7	1		2	1.1
Anterior	Median	25.6 (16.6)	23 (6.6)	**166.5 (9.9)****	80.6 (13.7)	93.3 (13.9)	81.1 (5)
	% Change		16.6	93.5		17.3	-0.2
Pertrochanter							
Lateral	Median	100.3 (8.8)	101 (14.6)	81.3 (12.1)	30.2 (20.2)	49.3 (29.2)	134.8 (34.8)
	% Change		-4.4	-14.9		11.3	29.5
Posterior	Median	100.2 (41)	123.3 (14.6)	**41.2 (20.6)*****	79.9 (44.8)	94.5 (52.3)	**127.5 (20.7)***
	% Change		6.3	-55.2		-0.8	58.4
Medial	Median	33.1 (28)	104.3 (67.2)	162.7 (13.6)	89.3 (6.1)	**81.9 (5.1)***	**82.8 (5)****
	% Change		3.2	47.2		-8.2	-7.3
Anterior	Median	67.5 (14.5)	54.3 (8.6)	56 (11.8)	131.5 (10.4)	136.5 (7.6)	153.2 (9.4)
	% Change		-2.1	-5.4		0.9	6.5

decreased the tensile (-55.2%, p<0.001) and increased the compressive (+58.4%, p=0.019) strain orientations in the posterior quadrant. Loading 2 (-8.2%, p=0.047) and 3 (-7.3%, p=0.0072) decreased the compressive orientation in medial quadrant. The anterior quadrant had the smallest changes for loading 2 and 3 ($< \pm 6.5\%$, p>0.05) (Table 4, Fig. 10).

2.7 Discussion

When only the joint reaction force was applied, the superior neck experienced maximum tensile strains while the inferior neck resulted in maximum compressive strains thereby indicating a bending moment throughout the femoral neck (Table 3). However, when muscle forces were included (loading 1 and 2), the principal strains of all four quadrants were in compression ($\left|-\varepsilon_3\right| > \left|\varepsilon_1\right|$), suggesting that including muscle forces decreased the bending moment observed in a hip joint force only model. The shift from bending to compression due to the combined loading of muscle and hip forces is consistent with other studies that have found that the femoral neck is primarily loaded in compression when muscle forces are included [42, 43, 11, 45]. However, these previous studies did not answer whether the

Figure 10: Median compressive and tensile orientation for 3 loading conditions in four quadrants of the middle femoral neck and pertrochanter. Dashed lines denote compressive orientation while solid lines denote tensile orientation.

differences were statistically significant since the sample sizes were low (n=1) and data was derived from variable sources.

Our results illustrate that without muscle forces (loading 3), compressive and tensile strains are significantly different from models that include muscle forces in every quadrant. The inclusion of some muscle forces (loading 2) resolves some of the discrepancies, but compressive and tensile strains remained significantly different for two quadrants. Likewise, in the pertrochanter loading 3 resulted in significantly different tensile and compressive strains in every quadrant, and loading 2 had significantly different strains for two quadrants. However, these changes did not alter the balance of tension and compression in the pertrochanter. Compressive strains remained larger than tensile strains for all three models and in every quadrant besides the lateral quadrant, which may be due to local muscle forces rather than bending. Of the significant differences in the middle neck and pertrochanter, the superior/lateral quadrant generally had the largest changes for both tensile and compressive strain, while the inferior/medial quadrant had the smallest changes (Table 3).

With decreased bending, and subsequently smaller tensile strains, the models with muscle forces do not follow Wolff's traditional tensile pattern in the femoral neck, supporting other studies that have questioned the validity of the Trajectorial Theory [9, 60, 61, 62]. Loading a majority of the trabecular bone in compression makes for better use of the mechanical

properties of bone and may be more likely to bring about bone remodelling [63, 9, 46, 64]. Our results contradict the large tensile trajectory in the femoral neck - a central claim of the Trajectorial Theory - but we do not ignore that there remain appreciable tensile strains (Table 3) when muscle forces are included, and some degree of bending in the femoral neck is likely [62]. This is evident by the fact that compressive strains were not uniform - and were instead larger in the inferior-posterior quadrants compared to the superior-anterior quadrants. Therefore, the femoral neck is likely in a state of combined loading of bending superimposed with compression. This leads us to question the validity of Wolff's Trajectorial Theory illustrating a tensile trajectory along the lateral/superior section of the femoral neck.

Including muscle forces also tended to significantly decrease the overall strain magnitudes in the femoral neck, as reported by others when analyzing strains throughout the femur [44, 65, 43]. For example, strain gauge measurements of the inferior femoral neck from Simoes and colleagues showed a similar decrease in magnitude ($\approx$ 400 $\mu\varepsilon$) when including muscle forces [44]. According to the mechanostat theory, this decrease may be physiologically significant, as the largest strain value (-1989 $\mu\varepsilon$) in loading 3 (JRF only) reaches the lower limit of the modeling minimum effective strain (MES), which has been proposed to trigger a bone response to reduce strain [47, 66]. On the other hand, the strain values in the model with muscle forces (-1608 to -854 and 408 to 601 $\mu\varepsilon$) fall more consistently within the physiological loading zone defined by the mechanostat theory. The opposite trend is evident in the pertrochanter, wherein strains in this region may be underpredicted (-294 $\mu\varepsilon$) without muscle forces (loading 3). When muscle forces are included (loading 1), compressive and tensile strain increase in the pertrochanter and fall within a more physiologically realistic strain range (-1414 to -708 and 577 to 1447 $\mu\varepsilon$) (Table 3). Several FE studies also point to the physiological significance of a homogeneous strain distribution, which is more evident in loading 1 of the middle neck [10, 45].

The strain orientations in the middle neck and pertrochanter were sensitive to muscle forces, but not to the same degree as strain magnitude (Tables 3, 4). In the femoral neck, the largest changes in orientation occurred in the superior quadrant, while the inferior quadrant saw no change in orientation. These results follow the same pattern as the changes in strain magnitude, potentially signifying the link between loading mode (bending vs. compression) and strain orientation. In the pertrochanter, the largest changes occurred in the posterior and medial quadrants, which did not follow the same pattern as strain magnitude. Both the femoral neck and pertrochanter were more sensitive to changes in their compressive, rather than tensile, orientation. The influence of muscle forces on strain orientation in the proximal femur should not be ignored and may be particularly relevant for studies modelling bone

adaptation or investigating trabecular bone orientation.

There are a few limitations to this study. The results shown here may differ for activities other than walking or non-postmenopausal individuals. For higher loading activities, different numerical strain values and trends are likely due to the difference in magnitude and relative contribution of muscle groups [39]. Another limitation is that our models assumed isotropic Young's moduli. Orthotropic moduli would undoubtedly provide more realistic material properties, but the error due to isotropic moduli is small [67] and systematic when comparing the three models. Lastly, proximal femur geometry may also contribute to bending. Others have shown that the hip axis length and neck shaft angle is linked to the degree of bending and hip fracture risk [68, 69, 70], but we do not expect these parameters to affect our results since the role of muscle forces on the same subject was considered. Care should be taken when interpreting the results in the distal diaphysis due to proximity to the fixed boundary condition.

In conclusion, our findings support the hypothesis that FE models used to calculate femoral neck strains during walking should not neglect the contribution of muscle forces, as they reduce bending and result in a strain distribution that is more physiologically likely. While subject specific FE modeling, as done here, is time consuming and not always feasible; the location, direction, and magnitude of muscle forces may be estimated with published data [71, 72] and would likely yield more physiologically accurate loading of the proximal femur. FE models including muscle forces help grow our understanding of how the femoral neck is physiologically loaded during normal activity, which is critical to identify activities that may encourage bone remodeling and prevent femoral neck fractures. The strain data provided in the study may also lead to improvements in pre-clinical testing of hip implants, as well as developments in the design of internal fixation devices.

CHAPTER 3

DVC ERROR AND MECHANICAL TESTING OF CORTICAL BONE IN THE FEMUR

3.1 Summary

Digital volume correlation (DVC) is a promising full-field experimental technique which may help elucidate the relationship between intracortical pore morphology and local strain. To the author's knowledge, no study has performed DVC on cortical bone from the clinically significant femoral neck region.

The superior neck, inferior neck and middle diaphysis were chosen based on morphological and structural differences throughout the femur. First, a pair of consecutive micro-CT scans was acquired of the specimen with no motion between the scans. Any strain measured was considered the strain error of our system. The effect of three DVC input parameters on strain error was assessed via a Design of Experiments (DOE). The subset size was varied from 41, 61, 81, 101, and 202, the subset step was 30% or 50% of the subset size, and the confidence threshold was 0.01 or 0.001 voxels. Prior to loaded digital volume correlation, mechanical testing was performed to characterize the cortical bone specimen and potting material, as well as to optimize DVC testing protocols. Finally, loaded DVC was performed using a CT-based mechanical testing system.

Several parameters such as subset size, step size, confidence threshold, and strain filter size were varied. The standard deviation of error calculated for all three specimen agreed with reported values, however, the mean error of the in-plane normal strain components (ε_{xx}, ε_{yy}) for the inferior and superior neck were larger than reported values, and they did not follow a power law trend. Although the femoral neck specimens had large in-plane strain errors, the ε_{zz} component was 1,330 $\mu\varepsilon$, which indicates that uniaxial compression/tension testing of these specimens is feasible. The large in-plane error calculated is likely due to the lack of in-plane pattern (i.e. smaller cortical bone thickness) compared to the diaphyseal specimen. A fixed platen, as opposed to a potted "endcap" molded to the shape of the bone, and bone cement formed the best experimental setup to reduce system compliance and stress relaxation during DVC testing. Further experimentation is required for loaded DVC, as our specimens underwent predominantly rigid body motion.

Studying the relationship between full-field strain and intracortical pore morphology in the femoral neck may one day lead to new insights into bone fragility, (re)modelling mechanisms, and allow for the validation of FE models.

3.2 Literature review

3.2.1 Imaging Bone

Significant personal, financial, and societal burdens due to osteoporotic fractures are considered to likely increase in the future, necessitating improved techniques for prevention, treatment, and rehabilitation of bone disease. Macro-level tests like DEXA cannot predict the underlying mechanisms that lead to femoral neck fractures. Therefore, consistent and accessible imaging modalities are critical to quantify cortical bone microstructure and understand its impact on mechanical strength.

High resolution peripheral quantitative computed tomography (HR-pQCT) is a promising method for in-vivo imaging of cortical bone, but the resolution remains too low to adequately quantify cortical bone microstructure since more up to 60% of cortical pores are less than 100 um in diameter [22]. Micro-computed tomography (uCT) is accessible, relatively inexpensive, and achieves a high resolution ($<$ 10 microns) sufficient to quantify cortical pores [2], making it the current gold standard for ex-vivo cortical microstructural analysis. Synchrotron-radiation micro-CT (SR-microCT) achieves higher resolution than micro-CT for ex-vivo specimens, but it is expensive and relatively inaccessible. Less common imaging techniques include ultrasound and magnetic resonance imaging (MRI), both of which do not emit radiation, but these methods need further technological development in regards to resolution and image quality to see widespread adoption [73].

Image volumes of cortical bone are used to quantify 2D or 3D microstructure. 2D measures of pores are calculated from cross-sectional images (Table 5), while 3D measures of canal networks are calculated using the entire image volume (Table 6). For example, one of the most common 2D measures is pore diameter (Po.Dm), which has been classified by size: small (7–95 μm), intermediate (95–180 μm), large (180–270 μm), extra-large (270–360 μm), and giant groups ($>$ 360 μm) [22]. The progression from 2D to 3D measures is straightforward for some parameters, such as pore diameter (2D) to canal volume (3D). However, more complex 3D measures first used in trabecular bone, such as connectivity density and tortuosity, cannot

Table 5: Measures of 2D cortical bone morphology [1]

Tt.At	mm^{-2}	Total cross sectional area inside the periosteal envelope
Ct.Ar	mm^{-2}	Cortical bone area = cortical volume Ct.V divided by the number of slices
Ct.Ar/Tt.Ar	%	Cortical area fraction
Ct.Th	mm	Average cortical thickness
Ps.Pm	mm	Periosteal perimeter
Ec.Pm	mm	Endocortical perimeter
Ct.Po	%	Cortical porosity: in a given cortical region, the volume of pores (Po.V) divided by the total volume of cortical bone compartment (Ct.V)
Po.N	n	Pore number
Po.V	mm^{-3}	Total pore volume
AvgPo.V	mm^{-3}	Average pore volume = Po.V divided by Po.N
Po.V.SD	mm^{-3}	Standard deviation of pore volume
Po.Dn	mm^{-3}	Pore density = pore number Po.N divided by total volume of cortical bone compartment Ct.V
Circularity		referred to as shape factor in some studies

be interpreted in 2D. Although more computationally intensive, 3D measures may provide a more complete picture of the heterogeneous pore network than traditional 2D measures.

Whether we characterize structure in 2D or 3D, one fact is certain: the cortical pore network is spatially heterogeneous. Chappard and colleagues found that there is greater porosity, pore diameter, pore number, and more large, extra-large and giant pores in the lateral superior neck compared to inferior neck and diaphysis [22]. Others have found that in women, canal diameter was highest in the superior region, and that these canals were significantly larger than those in the inferior region [26]. Together, these data provide evidence of the large variations in the structure of the intracortical network. Different regions and pore networks may provide insight into the heterogeneity of remodeling mechanisms and structure-strength relationships in cortical bone [22]. Experimentally, variations in cortical microstructure are important to consider when choosing specimen groups and regions of interest for a given experimental design aimed to evaluate the strength of bone.

3.2.2 Macro-mechanical Analysis of Bone Strength

Ex-vivo mechanical testing of bone is well documented for traditional loading conditions such as compression, tension, bending, shear, and torsion [74, 75, 76, 77, 78, 79, 80, 81, 82, 83]. Structural and material properties such as stiffness/Young's modulus, yield load/stress, yield displacement/strain, ultimate load/stress, and fracture toughness are derived from standard loading conditions and reported throughout the literature [84].

Table 6: Measures of 3D cortical bone morphology [2, 3]

TV	Tissue volume
Ca.V	Canal volume
Ca.S	Canal surface area
Ca.V/TV	Cortical porosity
Ca.S/TV	Canal surface to tissue volume
Ca.N	Canal number
Ca.Dm	Canal diameter
Ca.Sp	Canal seperation
Ca.Le/TV	Canal length to tissue volume
	Canal intersections
Ca.ConnD	Canal connectivity density
SMI	Structure model index
DA	Degree of anisotropy
	Tortuosity

Global mechanical properties are often related to microstructural properties to understand the determinants of strength in bone. For example, the fatigue life of secondary bone has been negatively correlated with canal diameter ($r^2 = 0.73$) and canal separation ($r^2 = 0.56$), while the fatigue life of plexiform bone was negatively correlated with canal separation ($r^2 = 0.41$), but positively correlated with canal number ($r^2 = 0.36$) [85]. Several other studies found similar results, wherein porosity was an important determinant of bone strength [86, 87, 88, 89, 90]. These findings suggest that the canal size and spacing may play an important role in the strength of bone. Further, porosity and osteonal density have been shown to be the best explanatory morphological parameters for fracture toughness [91]. Together, the morphological parameters could explain 49-68% of variation in fracture toughness. Interestingly, initiation fracture toughness is greater for a large number of small osteons rather than a small number of large osteons in the femur [91]. While important for characterizing macro-level strength, these relationships do not help us understand the local properties and the spatial origin of bone failure which are driven by the hierarchical and composite nature of bone.

3.2.3 Micro-Mechanical Analysis of Bone Strength: Computational Methods

Computational techniques were one of the first methods used to unravel the relationship between **local** structural and mechanical properties. Specifically, the current "gold standard"

for assessing local mechanical properties in bone is micro-finite element models (micro-FE or uFE), which are created using high-resolution image volumes such as uCT or HR-pQCT. The benefits of micro-FE modelling include saved material, monetary and time resources, as well as ease of developing subject specific models.

Micro-FE analysis allows researchers to create and analyze hierarchical and heterogeneous material and structural properties. For example, Gustafsson and colleagues have used micro-FE simulations to illustrate the importance of local cortical microstructure on crack propagation [92]. Further, a local analysis of mechanical stimuli has improved the understanding of bone (re)modelling events. For example, highly irregular intracortical pores are associated with increased strain energy, potentially signifying a disruption in the healthy cycle of remodelling and morphological alterations [93]. However, as the common aphorism states, "All models are wrong, but some are useful". Micro-FE models are no exception, and they should be validated using experimental methods.

3.2.4 Micro-mechanical Analysis of Bone Strength: Experimental Methods

Validating micro-FE models is a critical step to ensure that they provide reasonable predictions of the quantities of interest. However, validating local mechanical properties, in 3D, requires full-field experimental methods. Digital image correlation (DIC) and nanoindentation are two 2D full-field experimental methods used to validate FE models [94], but 3D full-field methods are less common.

At the turn of the century, advances in computational resources allowed for digital volume correlation (DVC) to emerge as a novel method for measuring 3D experimental full-field displacements and strains at the tissue level [95]. DVC is the 3D version of DIC, which is limited to surface or in-plane measurements. Both methods track the deformation of features within images by optimizing an objective function (Fig. 11). While the feature resolution of DIC is limited by the quality of the speckle pattern, DVC relies on the the naturally occurring 3D "speckle pattern" of materials. For example, DVC is able to track the internal patterns of rocks, foams, composites, and bone. The internal pattern of cortical bone is its naturally occurring canal network. In a brief period of time, the full-field bone strain measurements from DVC have helped us gain insight into crack initiation and propagation mechanisms [96, 97, 98], canal structure-strength relationships [3, 99], as well as validate FE models [100, 101, 102].

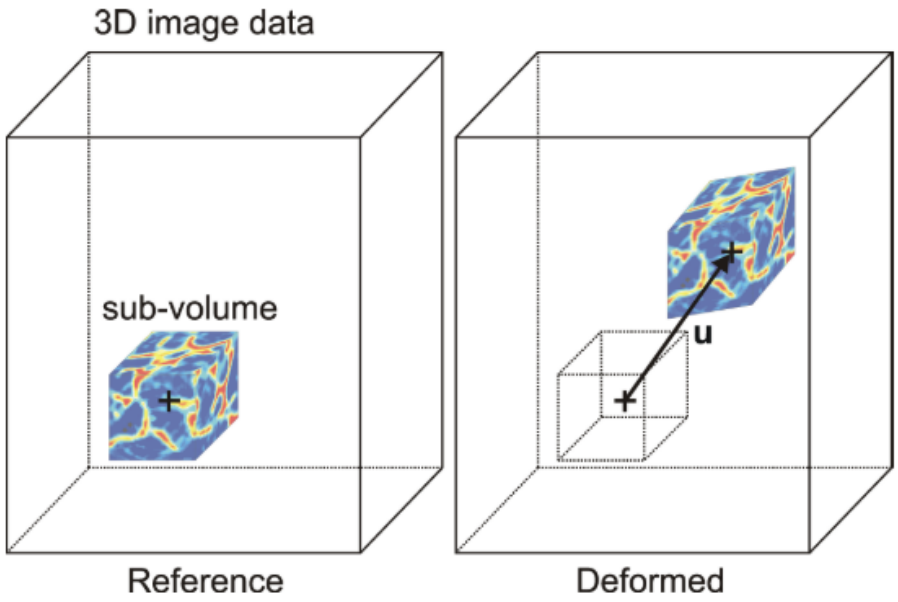

Figure 11: In digital volume correlation (DVC), volumes of the specimen are generated in both a reference and in a deformed state. DVC algorithms are used to calculate the displacement/strain field based on a naturally occurring internal pattern.

3.2.4.1 Digital Volume Correlation: Theory of Method

The following theoretical overview of the principles of DVC is summarized from Roberts and colleagues' review of DVC applications in bone [103].

1. Generation of 3D images volumes in both unloaded and loaded conditions.
    - Volumes of the specimen are generated in both an undeformed (reference) state and in a deformed state.
2. Measurement of a displacement field represented by discrete measurement points distributed throughout the specimen.
    - Within the reference image, a grid of points is defined
    - At each displacement measurement point, a 3D image subset of user-defined size is generated and centered about this point. The DVC algorithm then determines the deformation required to best correlate (map) the subset in the reference image with a subset in the deformed (loaded) image. This correlation requires the undeformed subvolume to undergo a deformation characterized by a function,

called "shape function" that encompasses the affine transformations: translation, rotation, normal strain and shear strain.

- Optimization algorithms: steepest descent, Levenberg-Marquardt method, or BFGS method used to minimize objective function.
- Objective function: Sum of squares correlation coefficient (SSCC), cross-correlation (CC), normalized cross-correlation (NCCC) and mutual information are typical functions used to map reference subset to corresponding position within deformed image.
- Interpolation is required if subvoxel deformations occur. Tricubic interpolation is common in the literature.

3. Calculations of strain tensors from the displacement field.

    - Smooth displacement data.
    - Gradient deformation tensor is estimated using least-squares fit or fitting second-order approximation of strain tensor.

3.2.4.2 Digital Volume Correlation: Influence of Parameters

The following overview of DVC parameters is summarized from Roberts and colleagues' review of DVC applications in bone [103].

- Subset size: Possibly the most influential parameter in terms of precision. Must be large enough so that during correlation procedure, intensity pattern is sufficiently unique. Smaller subsets show much larger displacement errors. Roberts and colleagues "suggest use of subsets that are sufficiently large to encompass unique datasets (e.g. subsets of 500 μm edge length when applied to human trabecular bone cores, such as cores 10 mm in height and 5 mm in diameter, scanned at 15 μm voxel size)".
- Objective function: Sum-of-square correlation coefficient (SSCC) or normalized cross-correlation coefficient (NCCC). Although SSCC offers balance between computational burdern and accuracy, the NCCC, while slower, is more accurate, especially when images exhibit low gray level contrast.
- Shape function: to avoid high errors due to non-translational deformations, implementing additional affine transformations (rotation, normal strain, shear strain) is recommended.

- Image voxel size: Changes in voxel size, at high resolutions, has minimal effect on error. For example, 12 to 20 and 36 microns increased error by less than 1 micron.
- Specimen microstructure: Smaller error for specimens having lower BV/TV (bone volume fractions), lower Tb.N (trabecular number), and higher Tb.Sp (trabecular separation) and SMI (structure model index).

3.2.4.3 Digital Volume Correlation: Error

Standardization in DVC remains a work in progress, and consequently, there are large variations in algorithms used, objective functions, shape functions, image processing techniques, intrinsic CT noise, and image resolution among studies. These parameters affect the accuracy and precision of displacement and strain measurements in DVC, which is why each unique experimental setup must quantify its error. Studies commonly scan and re-scan for no displacement, fixed rotation/displacement, or virtual rotation/displacement to quantify strain error [104]. Precision errors in strain smaller than 10% of nominal strain have been considered adequate [95, 105]. If however one desires to measure the full mechanical range (elastic, plastic, post-yield) smaller precision errors are required. Compared to continuum-level analyses, tissue-level analyses are likely to show larger strain measurement error due to proximity between measurement points [106]. Dall'ara and colleagues have shown that mean error (accuracy) and the standard deviation of error (precision) follow a power law relationship as a function of subset size/nodal spacing (NS) and are generally on the order of thousands of microstrain [12] (Figures 12,13).

3.3 Motivation

A significant proportion of fractures are attributed to the onset and accumulation of microdamage in cortical bone [107], yet the exact mechanisms involved remain unclear. The micro-mechanical environment of cortical bone may be influenced by several constituents, including pores, osteons, interstitial bone, cement lines, and vascular canals. These structural components all likely contribute to bone strength and fracture behavior, but how is not fully understood. Unravelling the relationships between dysfunctional pore (re)modelling, mechanical environment, and age-related degradation may lead to a better understanding of osteoporotic fracture risk.

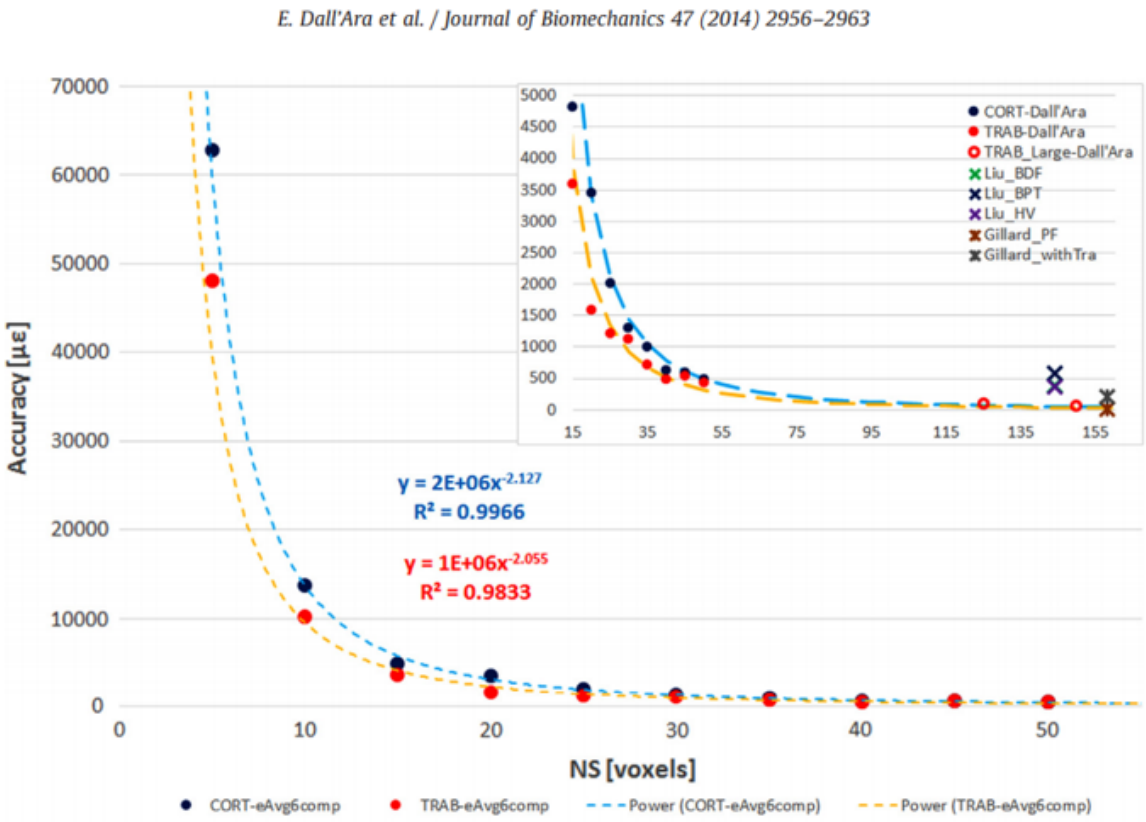

Figure 12: Mean error (accuracy) as a function of nodal spacing [12]

DVC is a promising full-field experimental technique which may help elucidate the relationship between intracortical pore morphology and local strain. While DVC has shown applicability in quantifying the full-field strain of bone, further experimentation on different loading conditions, length scales, and bone types will reveal new insights into local structure-function relationships in bone. Specifically, no study has performed DVC on cortical bone from the clinically significant femoral neck region. Studying the relationship between full-field strain and intracortical pore morphology in the femoral neck may lead to new insights into bone fragility, (re)modelling mechanisms, and allow for the validation of FE models.

3.4 Study aims

The goal of Chapter 3 was to optimize Digital Volume Correlation (DVC) for cortical bone samples from the femur. The specific aims were as follows:

1. Perform a DVC error analysis on cortical bone specimens from the middle diaphysis,

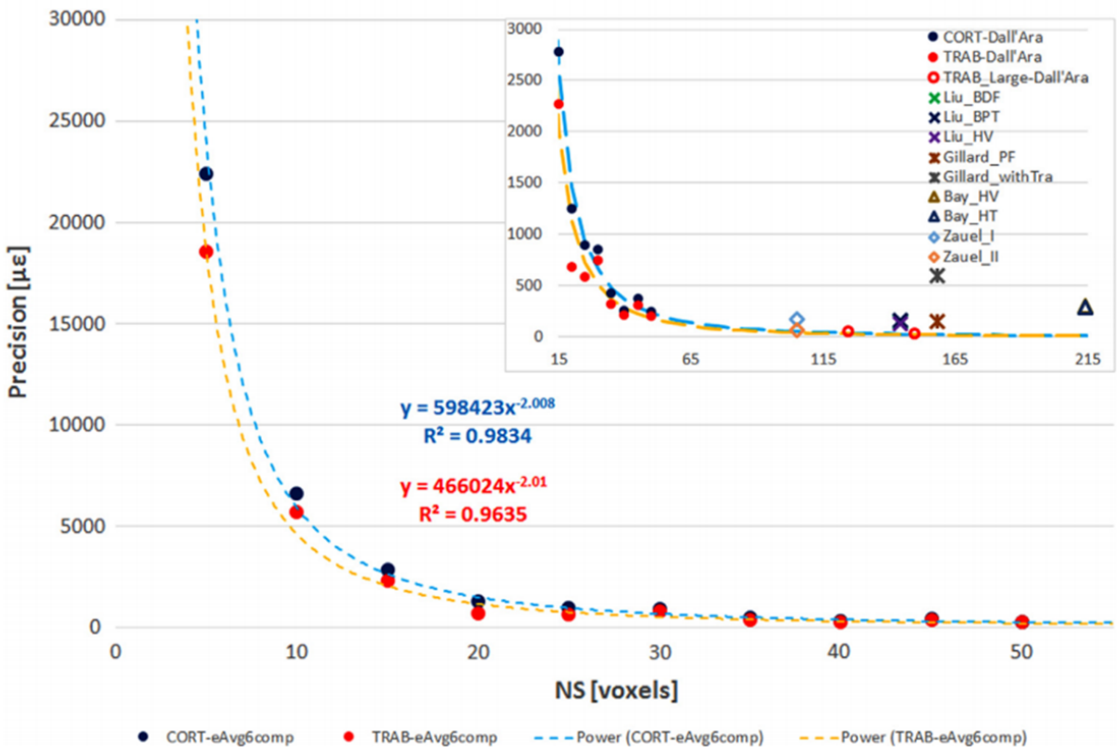

Figure 13: Standard deviation of error (precision) as a function of nodal spacing [12]

inferior neck, and superior neck of the femur

- We hypothesize that the error will be significantly different between the specimen regions due to the varying cortical thicknesses and intracortical pore structures

2. Perform mechanical testing on cortical bone samples to develop protocols for loaded DVC

3.5 Material and Methods

3.5.1 Specimen Preparation

The superior neck, inferior neck and middle diaphysis were chosen as the three specimen groups based on Chappard and colleagues' [22] findings on morphological and structural differences throughout the femur. These three groups have large differences in pore morphology and thickness, which will affect the pattern recognition in DVC. While the middle

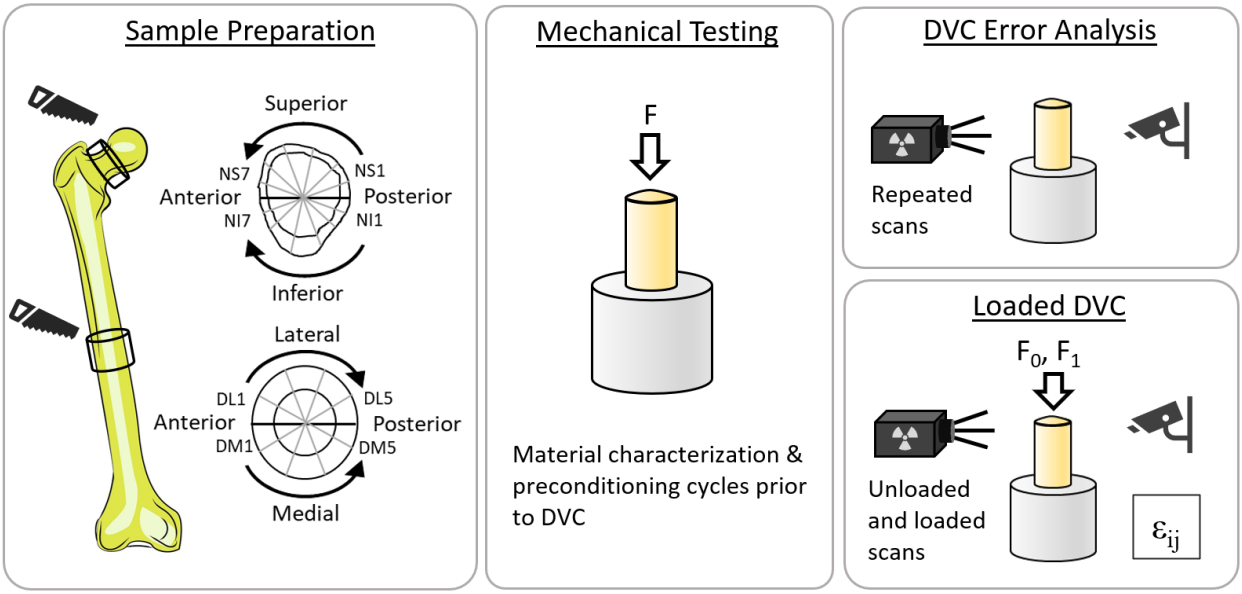

Figure 14: Specimens were sectioned from three regions of the femur. A subset of the specimen were mechanically tested to characterize specimen and potting materials. The other specimen were used to perform DVC error analyses or loaded DVC.

and proximal diaphysis had similar cortical thickness, ultimately the middle diaphysis was chosen since it was easier to section and more uniform about its cross section [108, 109].

A foam femur (Sawbones, Vashon Island, Washington, USA) and porcine femur (Meat Sciences Lab, University of Illinois Urbana Champaign) was used to practice sectioning and potting femoral neck specimens (Figs 31, 32). Next, the left femur of a fresh frozen cadaver (71 year old female, no history of bone disease) was thawed at room temperature. The specimen was kept damp during the entirety of specimen preparation, with the exception of potting. The femoral and diaphyseal axes were labeled using colord chalk to ensure that the specimens' long axes were cut parallel to the anatomical axes (Fig. 15).

Cortical bone specimen were sectioned using a diamond band saw (Gryphon C-40, Rio Grande, Albuquerque, NM) under constant irrigation. Initially, the entire femoral neck and middle diaphysis were cut out, before further sectioning into 7 specimens per half for the femoral neck and 5 per half for middle diaphysis, yielding a total of 19 specimens (14 from neck and 10 from middle diaphysis) (Fig. 16). The aspect ratio (i.e. the height to width ratio of the specimen) followed the 1:1-2 criteria to avoid buckling of the specimen during the compression test and thus maintain axial load application. The cortical bone specimen had full thickness maintained to replicate in-vivo boundary conditions. The final dimensions of the specimen were full cortical thickness, ≈5 mm wide, and ≈20 mm tall before potting,

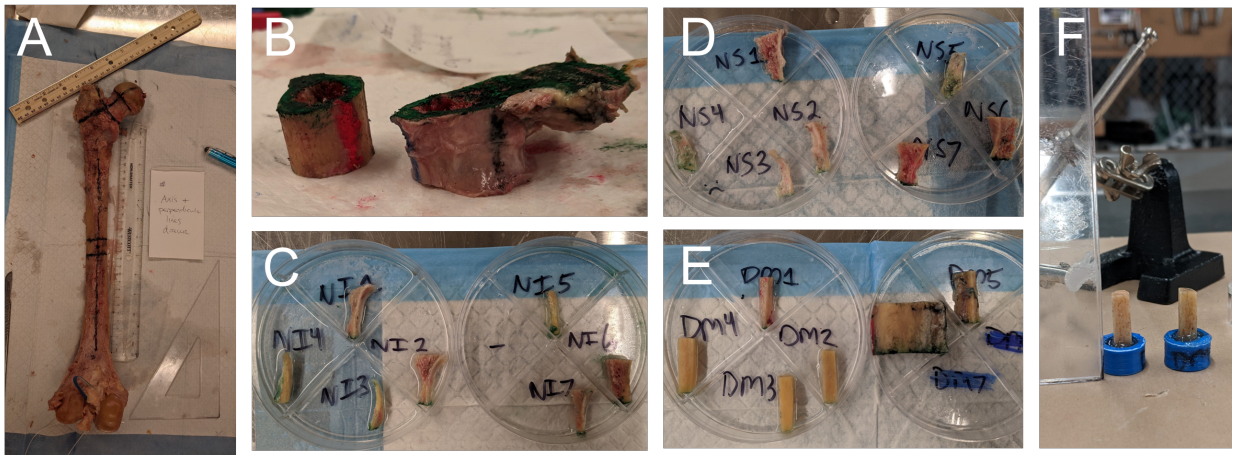

Figure 15: Femoral neck and diaphyseal axis were labeled (A). The femoral neck and middle diaphysis were sectioned (B) into ≈5 mm wide specimens (C-E). Finally, specimen were potted in either 3D printed or custom Deben endcaps (F).

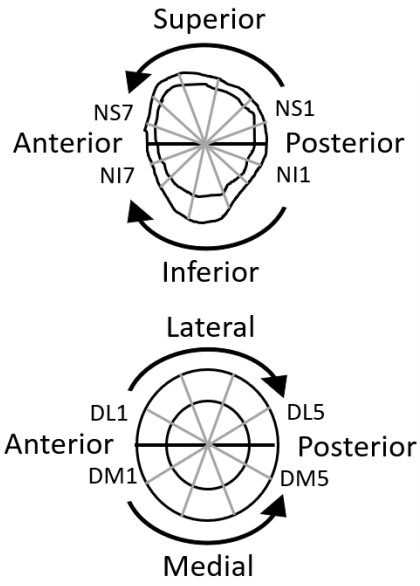

NS1	-
NS2	-
NS3	-
NS4	microCT
NS5	**DVC Error**
NS6	Mechanical testing
NS7	-

NI1	-
NI2	-
NI3	**DVC Error**
NI4	-
NI5	microCT
NI6	**DVC Loaded**
NI7	-

DM1	-
DM2	-
DM3	Mechanical testing
DM4	**DVC Error**
DM5	Mechanical testing

DL1	Mechanical testing
DL2	-
DL3	**DVC Loaded**
DL4	microCT
DL5	Mechanical testing

Figure 16: Specimen naming convention and role in the study

although this height was not achievable for some femoral neck specimen. Trabecular bone was removed and the specimen was sanded, when necessary. Post sectioning, specimen were cleaned using a water pick to remove bone dust, which may appear on micro-CT scans.

Specimen were potted using epoxy for non-loaded scans and bone cement for loaded scans. First, I marked off the depth of the specimen so as to leave an exposed aspect ratio of 2:1 [110]. The specimens had at least a 3:12 - 3:8 ratio of embedded length to free length given by Ohman and colleagues, who tested human cortical bone in PMMA under compression

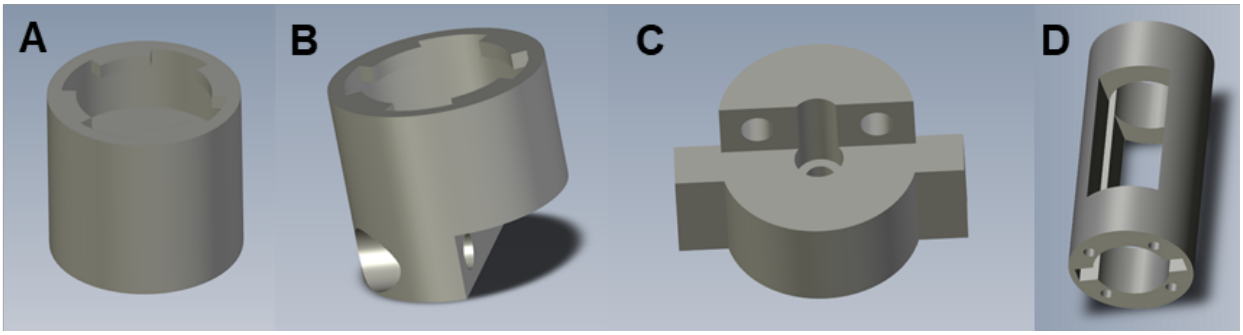

Figure 17: The custom Deben endcaps were comprised of a top end-cap that had a mold for the cortical bone surface and would compress the bone during mechanical tests (A), Bottom end-cap where the cortical bone is embedded (B), Base plate connector (C), and An alignment jig to ensure the end-caps are concentric to each other (D).

[111]. The specimen was held vertically in a clamp into either a 3D printed or custom Deben endcap (Fig. 17). The alignment of the specimen was checked using a level and set square. Specimen were completely dried before potting. Once potted, the final dimensions of the specimen were full cortical thickness, ≈5 mm wide, and ≈10 mm tall (2:1 aspect ratio). While not in use, specimens were wrapped in PBS soaked (not submerged) gauze, sealed in a petri dish or test tube, and placed in the freezer.

3.5.2 Micro-computed Tomography Imaging

Micro-computed tomography data was collected (Xradia MicroXCT- 200 and Xradia MicroXCT-400, Carl Zeiss AG, Oberkochen, Germany). The warm-up and scan had parameters of 68-69 V, 114 uA, and 7.8 W. The detector was positioned as close as possible (≈ 14.5 mm, ≈ 18-19 for DVC) to the cortical bone specimen to ensure best resolution. The exposure time was 1 and 2 seconds for the Xradia 400 and 200, respectively, and camera binning remained constant at 2. Using these parameters, a pixel size of ≈ 5.2 microns was achieved (Table 7).

Manual reconstruction was performed (XMReconstructor, Carl Zeiss AG, Oberkochen, Germany) to correct for beam hardening and center shift artifacts. Ring artifacts, motion artifact, and metal artifact were not observed in any of the scans. Center shift was manually corrected by either 0 or 1, and beam hardening was manually corrected using values of 0.5, 1 or 1.5. To maintain identical grayscale limits, byte scaling (-639.485, 1180.34) was held constant for all three DVC error scans. Finally, reconstructed image volumes were exported

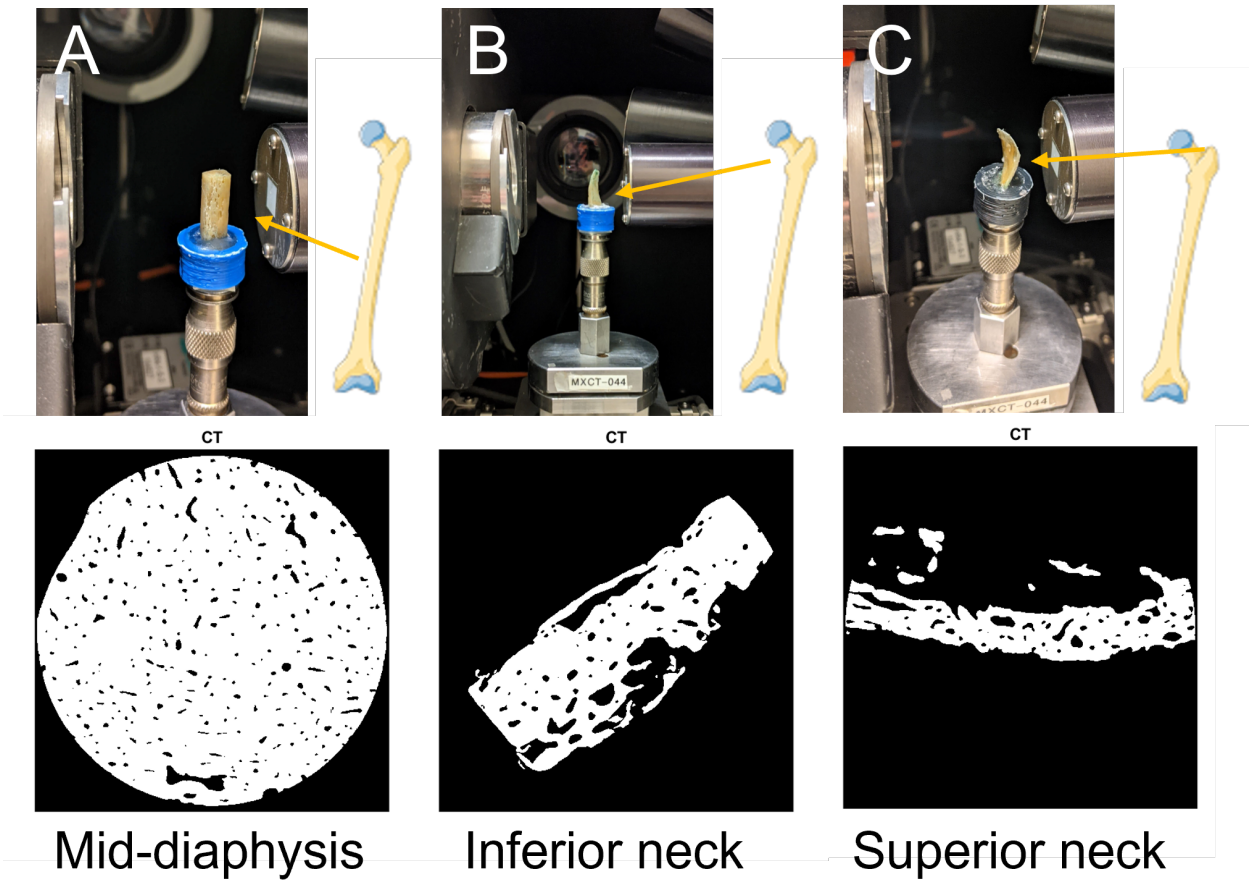

Figure 18: Representative micro-computed tomography images of the middle diaphysis, inferior neck, and superior neck

as 2D raw tiff (16 bit) images (Table 7, Fig. 18).

3.5.3 Image Processing

Image stacks were semi-automatically processed to decrease noise and scanning artifacts. For subsets sizes greater than 100 voxels, image stacks were resampled from 5 to 10 um using a Lanczos filter (Amira 2020, Thermo Fisher Scientific, MA, USA), resulting in an 1/8 decrease in image volume size. A non-local means filter was used to remove noise (kernel = 5, window ratio = 5) (MATLAB R2018b; MathWorks, Natick, MA, USA). The images volumes were further processed by subtracting the background, converting to 8-bit grayscale, and binarizing using a Phansalkar auto-local threshold (radius = 50) (ImageJ, NIH). Next, an interactive morphological reconstruction plugin (by dilation, 6) was used to removed

Table 7: Micro-computed tomography scanning parameters and reconstruction parameters

	Image Acquisition Settings								Reconstruction Parameters			
specimen	Voltage [V]	Current [uA]	Power (W)	Source - RA distance (mm)	Detector - RA distance (mm)	Exposure Time (sec)	Camera Binning	Pixel Size [um]	Center Shift	Beam Hardening	Byte Min	Byte Max
NI5	69	114	7.866	50	14.523	2	2	5.1794	0	1	-639.485	1180.34
NI3	69	114	7.866	54	14.5292	2	2	5.2667	0	1.5	-639.485	1180.34
NI3a	69	114	7.866	54	14.5292	2	2	5.2667	0	1.5	-639.485	1180.34
NI6	69	114	7.866	54	18.0223	1	2	5.0353	0	1	N/A	N/A
NI6a	69	114	7.866	54	18.0223	1	2	5.0353	0	1	N/A	N/A
DL4	68	114	7.752	54	14.498	2	2	5.2691	0	1	-639.485	1180.34
DM4	68	114	7.752	54	14.5086	2	2	5.2683	1	1	-639.485	1180.34
DM4a	68	114	7.752	54	14.508	2	2	5.2684	1	1	-639.485	1180.34
DL3	68	114	7.752	69.699	19.2005	3	2	5.2402	0	0.5	N/A	N/A
DL3a	68	114	7.752	69.699	19.2005	3	2	5.2402	0	0.5	N/A	N/A
NS4	68	114	7.752	54	14.498	2	2	5.2691	1	1.5	-639.485	1180.34
NS5	68	114	7.752	54	14.508	2	2	5.2684	1	1	-639.485	1180.34
NS5a	68	114	7.752	54	14.508	2	2	5.2684	1	1	-639.485	1180.34

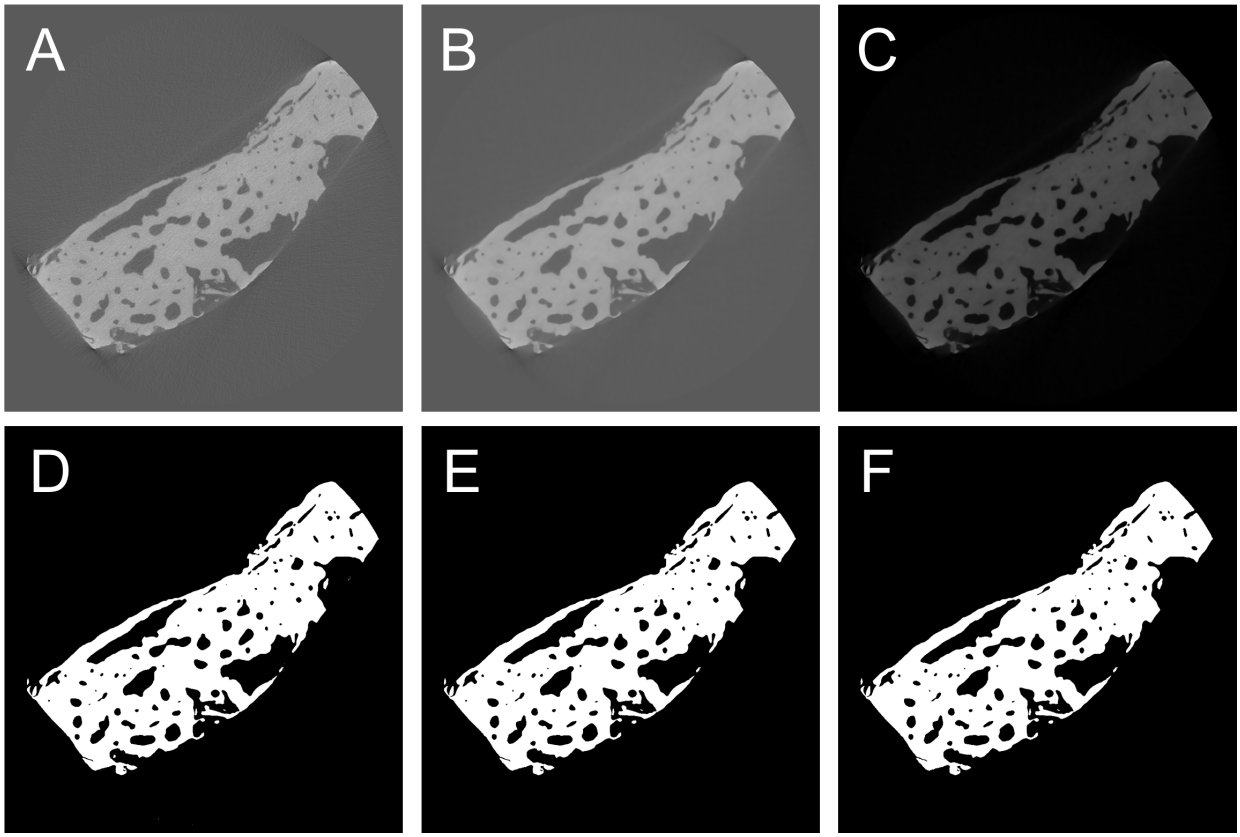

Figure 19: Image processing steps for micro-computed tomography generated images. Original (A), non-local means filter applied (B), background subtracted (C), binarized (D), morphological filter applied (E), and purified (F).

bone islands (MorphoLibJ, ImageJ, NIH). Finally, the purify plugin was used to eliminate or reconnect pores affected by the image reconstruction process (BoneJ, ImageJ, NIH) (Fig. 19).

3.5.4 Error Analysis Digital Volume Correlation

A pair of consecutive micro-CT scans was acquired of the specimen with no motion between the scans. Any strain measured was considered the strain error of our system. The effect of three DVC input parameters on strain error was assessed via a Design of Experiments (DOE). The subset size was varied from 41, 61, 81, 101, and 202, the subset step was 30% or 50% of the subset size, and the confidence threshold was 0.01 or 0.001 voxels (VIC-Volume, Correlated Solutions). However, not all runs were successful, depending on software and specimen limitations. The interpolation (optimized 8 tap), criterion (normalized squared differences), image type (filtered grayscale), consistency threshold (0.18 pixels), and matchability threshold (0.12 pixels) were held constant for all runs. A circular or rectangular region of interest (ROI) was manually drawn in VIC-Volume depending on the specimen geometry. The start point was manually chosen near the middle slice of the image volume. Initially, a filter size of 5 voxels was used for the strain calculation, but it was increased to 17 voxels for the final error calculations. Displacement and strain data were exported from VIC-Volume as CSV files and loaded into MATLAB (vR2018b; MathWorks, Natick, MA, USA) and R (R version 3.6.1, R Core Team) for post-processing and analysis.

3.5.5 Mechanical Testing

Prior to loaded digital volume correlation, mechanical testing was performed to characterize the cortical bone specimen and potting material, as well as to optimize DVC testing protocols. First, the stiffness of different types of potting material was measured to minimize the compliance of the system. A subset of specimens was loaded to 2% strain and another subset to failure on a universal testing machine (Instron, Norwood, MA, USA). The load-displacement data was converted to stress-strain data to calculate Young's modulus and failure strain. The data was checked for plateau regions, changes in slope, and other irregularities. Finally, loaded DVC specimens underwent pre-cyclic loading to reduce any end artifacts.

3.5.6 Loaded Digital Volume Correlation

Specimen were tested using a Deben compression stage (CT500, Deben UK Ltd, Suffolk, UK), which is a CT-based mechanical testing system capable of carrying loads up to 500

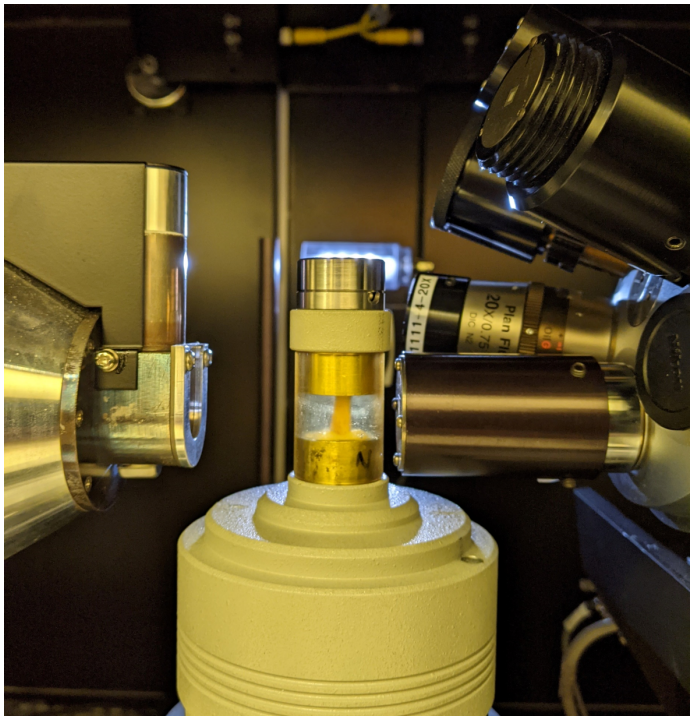

Figure 20: Loaded Digital Volume Correlation (DVC) test setup in Deben compression stage

N. Specimen were hydrated for one hour before experiments. The specimen-platen interface was lubricated to reduce friction. Prior to data collection, the cortical bone specimen were subjected to preconditioning cycles as a haversine waveform (1 Hz, 10 cycles) of 0.5% engineering strain to avoid edge effects from the harvesting process. The Deben test parameters were 500 ms sample time, displacement rate of 0.2mm/min, and a gain of x1. The specimen were loaded to 10 N. 10 minutes of settling time followed before acquiring the first micro-CT scan. Note that if drastic stress relaxation occurs, you may need more than 10 minutes of settling time. Next, specimen were loaded to 2% engineering strain. Again, 10 minutes of settling time followed before acquiring the second micro-CT scan (Fig. 20. The unloaded and loaded image volumes were processed and imported into VIC-Volume using the optimized input parameters. Displacement and strain data were exported from VIC-Volume as CSV files and loaded into MATLAB (vR2018b; MathWorks, Natick, MA, USA) and R (R version 3.6.1, R Core Team) for post-processing and analysis.

3.6 Results

3.6.1 Mechanical Testing

To remove the plateau region present at the beginning of the mechanical tests, a stiffer potting material was used and the specimen was sanded to improve surface planarity. The mechanical tests showed that the bone cement was stiffer than the epoxy, which in turn was stiffer than the Bondo. Further, our results show that loading the specimen with a fixed platen removed the initial plateau region, as well as decreased the stress relaxation, compared to an epoxy or bondo "endcap" molded to shape of the bone specimen. For a specimen from the middle diaphysis, the failure strain was approximately double when one end of the specimen was potted compared to both ends free. The Young's modulus calculated from the cortical bone specimens was ≈ 0.5 GPa when potted compared to ≈ 2 GPa when free on both ends. In summary, a fixed platen, as opposed to a potted "endcap" molded to the shape of the bone, and bone cement formed the best experimental setup to reduce system compliance and stress relaxation during DVC testing.

3.6.2 Error Quantification

VIC-Volume failed to compute displacement/strain fields for several of the smaller subset sizes (e.g. 41 or 61 voxels) due to lack of pattern to trace. A confidence threshold of 0.001 also caused errors for several runs because it was too restrictive for the image quality of our micro-CT scans.

For the diaphyseal specimen, the strain filter size was varied (Figs. 33, 34) from 5-23 voxels. We found that as filter size increased, the mean error decreased (≈ 200 $\mu\varepsilon$). The standard deviation of error decreased (≈ 200 $\mu\varepsilon$) for the 3 shear strain components and for the 3 normal strain components (≈ 700 $\mu\varepsilon$) (Figs 33, 34, 35). With a final filter size of 17, a DOE was performed to calculate mean error and standard deviation for the three specimen groups.

The subset size, subset step, and confidence threshold was varied for the design of experiments (DOE). In the middle diaphysis, mean error and standard deviation of error decreased for all strain components as a function of subset size, following a power law trend. From a subset size of 41 to 202 voxels (205 to 1010 μm), the mean error decreased (≈ 1500 $\mu\varepsilon$)

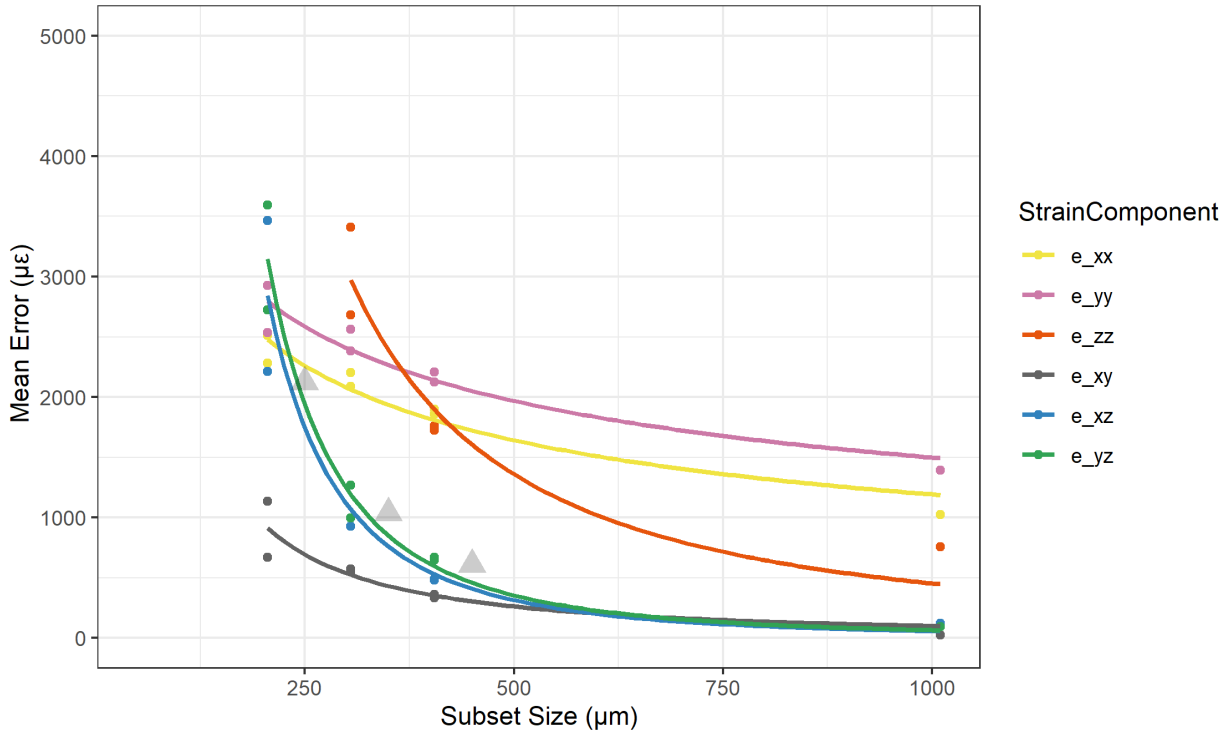

Figure 21: Absolute mean error as a function of subset size in the middle diaphysis specimen. Gray triangles are data digitized from Dall'ara and colleagues [12].

for the two in-plane normal strain components (ε_{xx}, ε_{yy}) and for ε_{yz}, ε_{xz}, and ε_{zz} ($\approx$ 3000 $\mu\varepsilon$). ε_{xy} did not follow either of these trends; it decreased by $<$ 1000 $\mu\varepsilon$ (Fig. 21). The standard deviation of error decreased ($\approx$ 1000-1500 $\mu\varepsilon$) for all six strain components (Fig. 22). The two in-plane normal strain components had a larger magnitude of mean error and standard deviation of error for subsets larger than 250 μm. The effect of subset step and the confidence threshold was not easily discernible due to lack of successful runs (Figs. 36, 37).

In the inferior neck, only the standard deviation of error decreased for all strain components as a function of subset size, following a power law trend. From a subset size of 41 to 202 voxels (205 to 1010 μm), the mean error did not decrease for any strain component (Fig. 23). The two in-plane normal strain components (ε_{xx}, ε_{yy}) had a larger of magnitude mean error than the other four components for all subset sizes. The standard deviation of error decreased ($\approx$ 1000-1500 $\mu\varepsilon$) for all six strain components (Fig. 24). The two in-plane normal strain components had a larger magnitude of standard deviation of error for all subset sizes. For the DOE, a smaller confidence threshold and larger step size decreased the standard deviation of error (Figs. 38, 39).

In the superior neck, the standard deviation of error decreased for all strain components

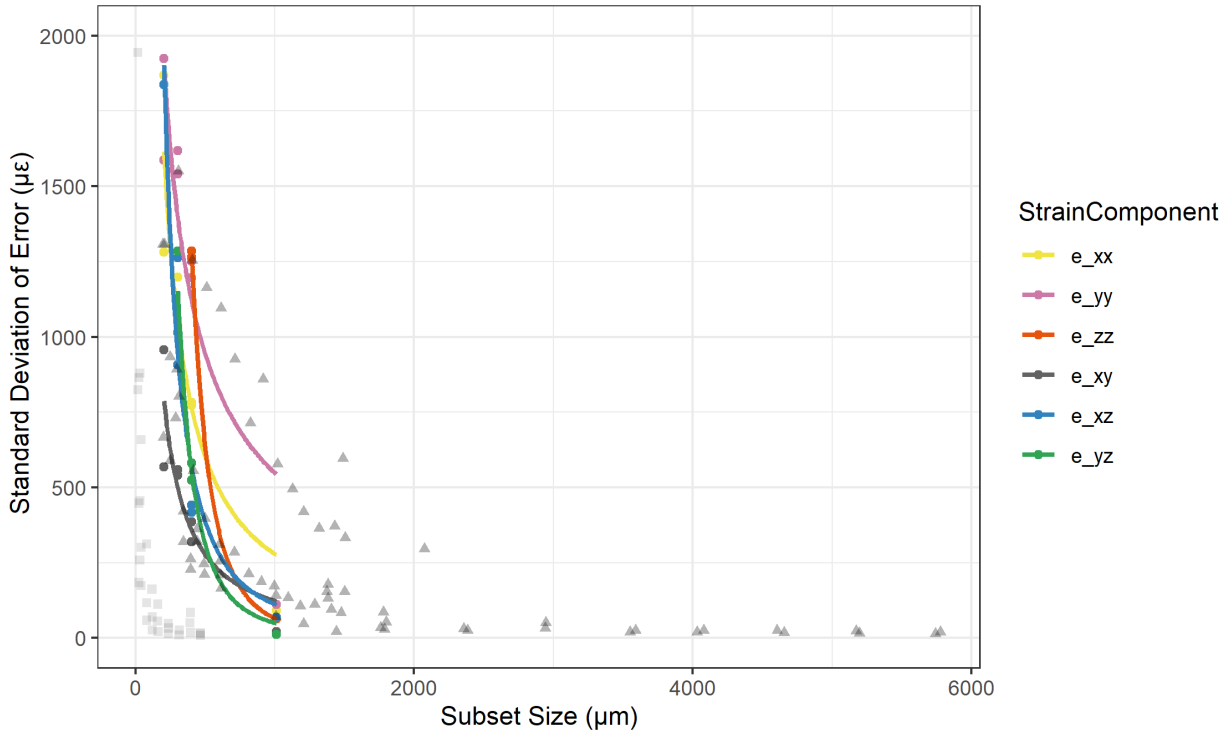

Figure 22: Absolute standard deviation of error as a function of subset size in the middle diaphysis specimen. Gray triangles are digitized micro-CT data and lighter gray squares are digitized synchrotron data, both from Dall'ara and colleagues [13].

except ε_{xy} as a function of subset size, following a power law trend. From a subset size of 41 to 202 voxels (205 to 1010 μm), the mean error did not decrease for any strain component except ε_{yy} (Fig. 25). The two in-plane normal strain components (ε_{xx}, ε_{yy}) had a larger of magnitude mean error than the other four components for all subset sizes. The standard deviation of error decreased ($\approx$ 700 $\mu\varepsilon$) for two in-plane normal strain components and decreased ($\approx$ 200-500 $\mu\varepsilon$) for ε_{zz}, ε_{xz}, and ε_{yz} (Fig. 26). The two in-plane normal strain components had a larger magnitude of standard deviation of error for all subset sizes. For the DOE, a smaller confidence threshold and larger step size decreased the standard deviation of error (Figs. 40, 41).

Based on our DOE, the final input parameters chosen were a subset size of 202 voxels (1010 μm), subset step of 60 voxels, confidence threshold of 0.01, optimized 8-tap interpolation, normalized squared differences criterion, consistency threshold of 0.18, matchability threshold of 0.12, and a strain filter size of 17. The mean error and standard deviation of error calculated for these parameters generally increased as cortical thickness of specimen decreased (middle diaphysis - inferior neck - superior neck). The two in-plane normal strain

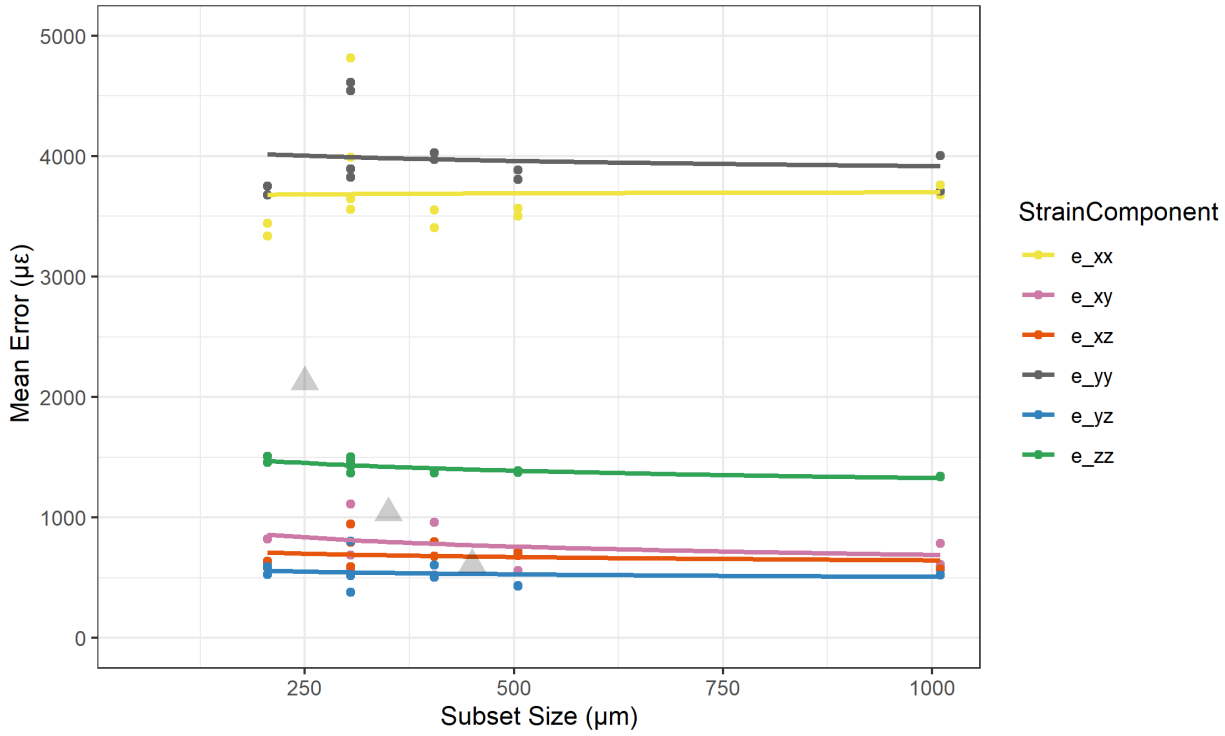

Figure 23: Absolute mean error as a function of subset size in the inferior neck specimen. Gray triangles are data digitized from Dall'ara and colleagues [12].

components (ε_{xx}, ε_{yy}) had the largest mean error for all three specimens (Table 8).

3.6.3 Loaded Digital Volume Correlation

One specimen from the middle diaphysis and one specimen from the inferior neck were loaded to 2% strain (Figs. 44, 45, 42, 43). The Young's modulus calculated from the cortical bone specimens was approximately 0.5 GPa. VIC-Volume calculated a local displacement of approximately 50% of the applied displacement, but only $\approx 1000\mu\varepsilon$, indicating that a majority of the displacement was rigid body motion (Figs. 46, 47).

3.7 Discussion

The cortical bone specimens had decreased Young's modulus compared to the approximately 20 GPa reported in the literature. The decreased modulus is likely a result of older,

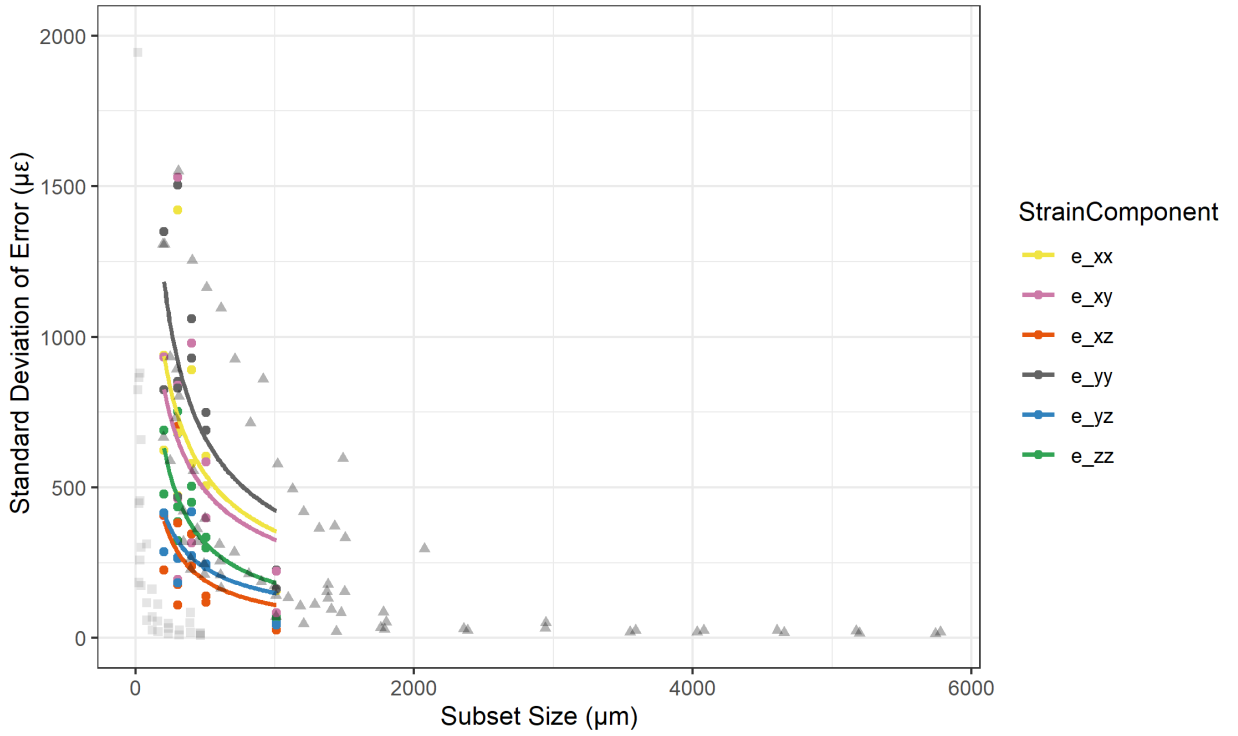

Figure 24: Absolute standard deviation of error as a function of subset size in the inferior neck specimen. Gray triangles are digitized micro-CT data and lighter gray squares are digitized synchrotron data, both from Dall'ara and colleagues [13].

postmenopausal bone which exhibited trabecularization and large pores in our micro-CT images. From the mechanical testing of specimen and potting materials, it was observed that an initial plateau region in the load-displacement curve indicated that the potting material was compliant, as was the case with the epoxy and Bondo, or that the specimen surface was not fully parallel to platen. Care must be taken in sectioning the specimen surface parallel to the loading platen, using the least compliant potting material, and characterizing specimens prior to loaded DVC.

DVC error is highly variable and dependent on the pattern traced, CT scanner noise, image processing protocols, and specimen variance. Further, a compromise must always be accepted between the precision of the DVC measurements and the measurement spatial resolution [12]. This held true for our results, where mean error and standard deviation of error decreased as subset size increased (Figs. 23, 24, 25, 26, 21, 22), but at the sacrifice of the spatial resolution of displacement/strain measurements. The standard deviation of error calculated for all three specimen agreed with reported values, however, the mean error of the in-plane normal strain components (ε_{xx}, ε_{yy}) for the inferior and superior neck were

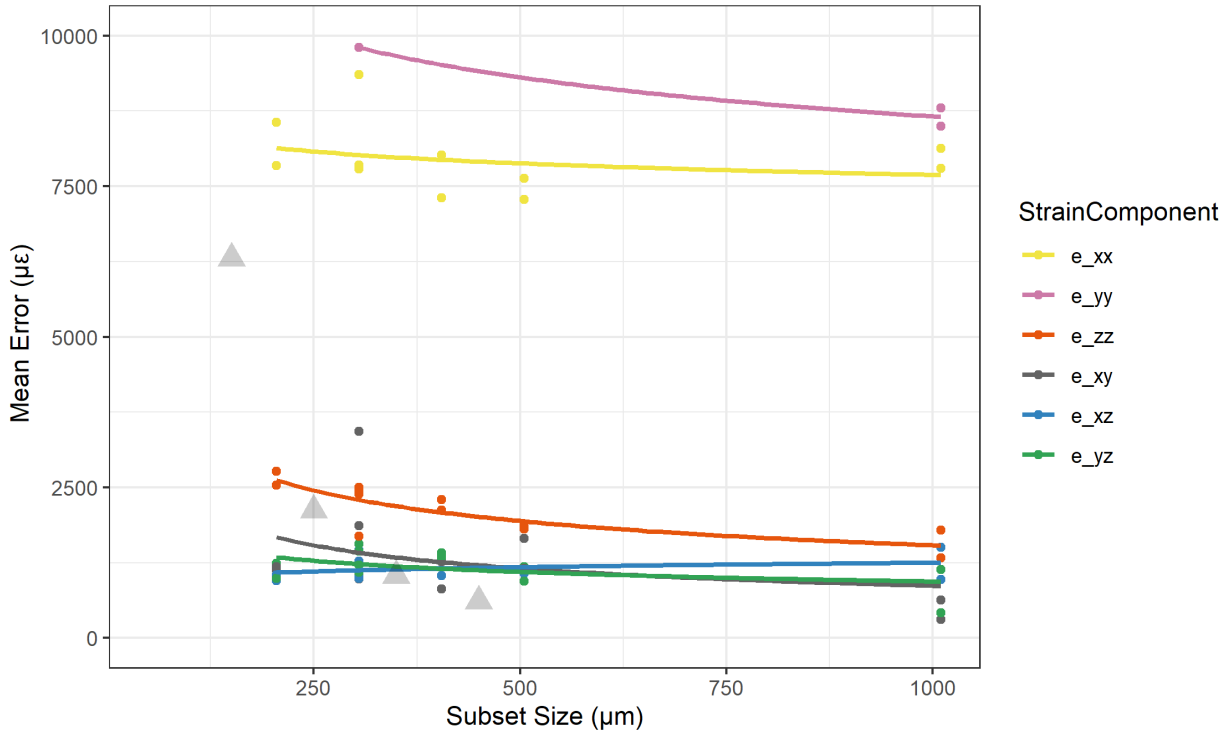

Figure 25: Absolute mean error as a function of subset size in the superior neck specimen. Gray triangles are data digitized from Dall'ara and colleagues [12].

larger than reported values, and they did not follow a power law trend (Figs. 23, 24, 25, 26, 21, 22). Although the femoral neck specimens had large in-plane strain errors, the ε_{zz} component was 1,330 $\mu\varepsilon$, which indicated that uniaxial compression/tension testing of these specimens is feasible. The large in-plane error calculated was likely due to the lack of in-plane pattern (i.e. smaller cortical bone thickness) compared to the diaphyseal specimen. Removing strain outliers and subsets at the bone specimen perimeter did not greatly affect the strain error.

While subset size is the most important input parameter [103], the effect of several other parameters such as step size, confidence threshold, and strain filter size was varied. The strain filter size controls the smoothing window and influences the "virtual strain gauge" size for DVC (Equation 1).

$$Virtual\ strain\ gauge = \Big(filter\ size\Big) \times \Big(step\ size\Big) \tag{8}$$

A larger strain filter size decreased the mean error and standard deviation of error, in accordance with the error-measurement resolution trade-off (Figs. 33, 34). Although a

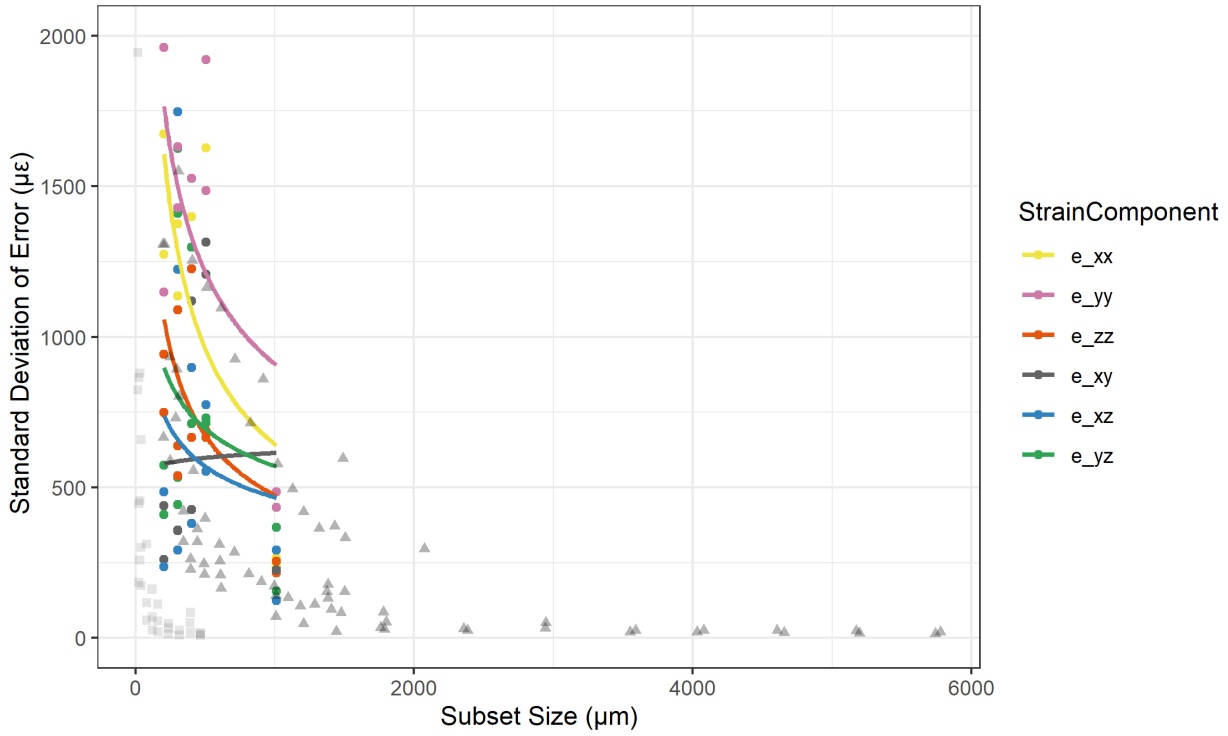

Figure 26: Absolute standard deviation of error as a function of subset size in the superior neck specimen. Gray triangles are digitized micro-CT data and lighter gray squares are digitized synchrotron data, both from Dall'ara and colleagues [13].

smaller confidence threshold resulted in decreased strain error, it caused many failed runs because the threshold was too restrictive for our image quality. Therefore, a 0.01 threshold value was used for the final error calculation and is recommended for future studies using a similar micro-CT scanner (Table 8). A 50% subset step decreased the standard deviation of error compared to a 30% subset step (Figs. 37, 39, 41), but as expected the effect was small compared to the subset size.

The two loaded DVC specimen underwent mostly rigid body motion due to compliance in the potting material, aluminum endcaps, or Deben system. Thus, the compliance must be decreased in future experiments or the specimen should be loaded to an larger global strain to induce larger local strains. The most compliant material in the system was likely the bone cement; therefore, it is advised to take extra precautions during specimen preparation and potting. Air pockets in the bone cement, a weak bone cement/cortical bone interface, or not fully drying the bone specimen before potting could all negatively impact the sample quality, and therefore the compliance of the system.

There are several limitations to this study. We only tested one specimen per femoral

Table 8: Mean error and standard deviation of error in three femoral specimen using final DVC input parameters

		Middle Diaphysis	Inferior Neck	Superior Neck
ε_{xx}	Mean Error ($\mu\varepsilon$)	1,020	3,670	8,120
	Standard Deviation of Error ($\mu\varepsilon$)	91	163	265
ε_{yy}	Mean Error ($\mu\varepsilon$)	1,390	3,700	8,490
	Standard Deviation of Error ($\mu\varepsilon$)	111	225	432
ε_{zz}	Mean Error ($\mu\varepsilon$)	759	1,330	1,330
	Standard Deviation of Error ($\mu\varepsilon$)	64	79	216
ε_{xy}	Mean Error ($\mu\varepsilon$)	25	786	628
	Standard Deviation of Error ($\mu\varepsilon$)	20	221	235
ε_{xz}	Mean Error ($\mu\varepsilon$)	123	590	1,500
	Standard Deviation of Error ($\mu\varepsilon$)	68	44	292
ε_{yz}	Mean Error ($\mu\varepsilon$)	95	569	1,130
	Standard Deviation of Error ($\mu\varepsilon$)	11	58	154

region, so we cannot comment on the distribution of strain error. The specimen was not continuously hydrated throughout scanning, which may cause bone to become brittle, but our target strain was well within the elastic and not post-yield region. Further, error scans were acquired externally to the Deben compression stage, but the difference in scan resolution was <0.03 microns and large differences in image quality were not observed. Another limitation is that the Deben could only withstand a maximum load of 500 N, which was insufficient for loading diaphyseal specimens. Prolonged exposure to radiation could damage the bone specimens, but we did not use long exposure times, high-energy synchrotron x-rays nor did we did test post-yield behavior [112, 113]. Lastly, this study does not address whole bone DVC, which may be more clinically relevant, but the resolution of data generally decreases at whole bone length scales, making it more difficult to study the intracortical pore network.

Keeping the trabecular bone intact with the cortical specimens from the femoral neck may help to increase the in-plane "thickness" or pattern, which would in turn decrease strain error. Further, improved micro-CT scanning and image processing protocols could improve the signal-to-noise ratio and hence provide lower strain error, but these are not likely to decrease the in-plane strain error close to reported values. It is worth investigating whether an improved micro-CT resolution would provide more pattern to trace via a greater number of pores and cement lines. DVC should continue to be explored on different bone specimens, but it is critical to remember that new specimens (e.g. young bone) may exhibit different intracortical networks and therefore a new error analysis must be completed. To save scanning time, error scans can take place on the same specimen prior to loaded DVC.

It is also recommended to pot all specimens using bone cement, if financially feasible. When testing loaded DVC on cortical bone from the femoral neck, I advise loading to a larger elastic strain or failure, due to the large strain errors calculated in this study. For loaded DVC of thicker cortical samples such as the diaphysis, it is recommended to use a 5kN Deben. Once loaded DVC protocols on femoral neck samples are fully optimized, an entire world of possibilities will open such as understanding relationships between full-field strain and intracortical pore morphology, as well as validating full-field FE full models using DVC-derived boundary conditions [102].

REFERENCES

[1] M. L. Bouxsein, S. K. Boyd, B. A. Christiansen, R. E. Guldberg, K. J. Jepsen, and R. Müller, "Guidelines for assessment of bone microstructure in rodents using micro-computed tomography," 2010.

[2] D. M. Cooper, A. L. Turinsky, C. W. Sensen, and B. Hallgrímsson, "Quantitative 3D analysis of the canal network in cortical bone by micro-computed tomography," 2003.

[3] M. Peña Fernández, A. P. Kao, F. Witte, H. Arora, and G. Tozzi, "Low-cycle full-field residual strains in cortical bone and their influence on tissue fracture evaluated via in situ stepwise and continuous X-ray computed tomography," *Journal of Biomechanics*, 2020.

[4] Staff, "Medical gallery of Blausen Medical 2014," *WikiJournal of Medicine*, 2014.

[5] W. G. Jerome, "Cell and Tissue Biology: A Textbook of Histology," *JAMA: The Journal of the American Medical Association*, 1989.

[6] E. A. Zimmermann, E. Schaible, H. Bale, H. D. Barth, S. Y. Tang, P. Reichert, B. Busse, T. Alliston, J. W. Ager, and R. O. Ritchie, "Age-related changes in the plasticity and toughness of human cortical bone at multiple length scales," *Proceedings of the National Academy of Sciences of the United States of America*, 2011.

[7] P. Susan Standring DSc, *Gray's Anatomy 41st edition: The Anatomical Basis of Clinical Practice*, 2015.

[8] R. Zebaze and E. Seeman, "Cortical bone: A challenging geography," 2015.

[9] A. Hammer, "The paradox of Wolff's theories," 2015.

[10] G. N. Duda, M. Heller, J. Albinger, O. Schulz, E. Schneider, and L. Claes, "Influence of muscle forces on femoral strain distribution," *Journal of Biomechanics*, 1998.

[11] K. E. Rudman, R. M. Aspden, and J. R. Meakin, "Compression or tension? The stress distribution in the proximal femur," *BioMedical Engineering Online*, 2006.

[12] E. Dall'Ara, D. Barber, and M. Viceconti, "About the inevitable compromise between spatial resolution and accuracy of strain measurement for bone tissue: A 3D zero-strain study," *Journal of Biomechanics*, 2014.

[13] E. Dall'Ara, M. Peña-Fernández, M. Palanca, M. Giorgi, L. Cristofolini, and G. Tozzi, "Precision of digital volume correlation approaches for strain analysis in bone imaged with micro-computed tomography at different dimensional levels," *Frontiers in Materials*, 2017.

[14] S. Cowin and J. Telega, "Bone Mechanics Handbook, 2nd Edition. -," *Applied Mechanics Reviews*, 2003.

[15] B. Clarke, "Normal bone anatomy and physiology." 2008.

[16] S. K. Eswaran, A. Gupta, M. F. Adams, and T. M. Keaveny, "Cortical and trabecular load sharing in the human vertebral body," *Journal of Bone and Mineral Research*, 2006.

[17] G. Holzer, G. Von Skrbensky, L. A. Holzer, and W. Pichl, "Hip fractures and the contribution of cortical versus trabecular bone to femoral neck strength," *Journal of Bone and Mineral Research*, 2009.

[18] M. J. Olszta, X. Cheng, S. S. Jee, R. Kumar, Y. Y. Kim, M. J. Kaufman, E. P. Douglas, and L. B. Gower, "Bone structure and formation: A new perspective," 2007.

[19] M. J. Silva, *Skeletal Aging and Osteoporosis*, 2011.

[20] X. Wang and Q. Ni, "Determination of cortical bone porosity and pore size distribution using a low field pulsed NMR approach," *Journal of Orthopaedic Research*, 2003.

[21] V. L. Yeager, S. Chiemchanya, and P. Chaiseri, "Changes in size of lacunae during the life of osteocytes in osteons of compact bone," *Journals of Gerontology*, 1975.

[22] C. Chappard, S. Bensalah, C. Olivier, P. J. Gouttenoire, A. Marchadier, C. Benhamou, and F. Peyrin, "3D characterization of pores in the cortical bone of human femur in the elderly at different locations as determined by synchrotron micro-computed tomography images," *Osteoporosis International*, 2013.

[23] H. M. Frost, "Bone "mass" and the "mechanostat": A proposal," *The Anatomical Record*, 1987.

[24] S. C. Cowin and M. L. Moss, "Mechanosensory mechanisms in bone," in *Bone Mechanics Handbook, Second Edition*, 2001.

[25] L. M. Wancket, "Animal Models for Evaluation of Bone Implants and Devices: Comparative Bone Structure and Common Model Uses," *Veterinary Pathology*, 2015.

[26] K. L. Bell, N. Loveridge, J. Power, N. Garrahan, B. F. Meggitt, and J. Reeve, "Regional differences in cortical porosity in the fractured femoral neck," *Bone*, 1999.

[27] M. S. Stein, S. A. Feik, C. D. Thomas, J. G. Clement, and J. D. Wark, "An automated analysis of intracortical porosity in human femoral bone across age," *Journal of Bone and Mineral Research*, 1999.

[28] J. Jowsey, "Studies of Haversian systems in man and some animals." *Journal of anatomy*, 1966.

[29] D. M. Cooper, C. D. L. Thomas, J. G. Clement, A. L. Turinsky, C. W. Sensen, and B. Hallgrímsson, "Age-dependent change in the 3D structure of cortical porosity at the human femoral midshaft," *Bone*, 2007.

[30] I. S. Cenzer, V. Tang, W. J. Boscardin, A. K. Smith, C. Ritchie, M. I. Wallhagen, R. Espaldon, and K. E. Covinsky, "One-Year Mortality After Hip Fracture: Development and Validation of a Prognostic Index," *Journal of the American Geriatrics Society*, vol. 64, no. 9, pp. 1863–1868, 2016.

[31] K. G. Thorngren, A. Hommel, P. O. Norrman, J. Thorngren, and H. Wingstrand, "Epidemiology of femoral neck fractures," *Injury*, 2002.

[32] E. Hernlund, A. Svedbom, M. Ivergård, J. Compston, C. Cooper, J. Stenmark, E. V. McCloskey, B. Jönsson, and J. A. Kanis, "Osteoporosis in the European Union: Medical management, epidemiology and economic burden: A report prepared in collaboration with the International Osteoporosis Foundation (IOF) and the European Federation of Pharmaceutical Industry Associations (EFPIA)," *Archives of Osteoporosis*, vol. 8, no. 1-2, 2013.

[33] N. Harvey, E. Dennison, and C. Cooper, "Osteoporosis: Impact on health and economics," 2010.

[34] R. K. Fuchs, J. J. Bauer, and C. M. Snow, "Jumping improves hip and lumbar spine bone mass in prepubescent children: A randomized controlled trial," *Journal of Bone and Mineral Research*, vol. 16, no. 1, pp. 148–156, 2001.

[35] K. J. MacKelvie, H. A. McKay, K. M. Khan, and P. R. Crocker, "A school-based exercise intervention augments bone mineral accrual in early pubertal girls," *Journal of Pediatrics*, vol. 139, no. 4, pp. 501–508, 2001.

[36] M. A. Petit, H. A. McKay, K. J. Mackelvie, A. Heinonen, K. M. Khan, and T. J. Beck, "A randomized school-based jumping intervention confers site and maturity-specific benefits on bone structural properties in girls: A hip structural analysis study," *Journal of Bone and Mineral Research*, 2002.

[37] T. F. Lang, I. H. Saeed, T. Streeper, J. Carballido-Gamio, R. J. Harnish, L. A. Frassetto, S. M. Lee, J. D. Sibonga, J. H. Keyak, B. A. Spiering, C. M. Grodsinsky, J. J. Bloomberg, and P. R. Cavanagh, "Spatial heterogeneity in the response of the proximal femur to two lower-body resistance exercise regimens," *Journal of Bone and Mineral Research*, vol. 29, no. 6, pp. 1337–1345, 2014.

[38] R. Nikander, P. Kannus, P. Dastidar, M. Hannula, L. Harrison, T. Cervinka, N. G. Narra, R. Aktour, T. Arola, H. Eskola, S. Soimakallio, A. Heinonen, J. Hyttinen, and H. Sievänen, "Targeted exercises against hip fragility," *Osteoporosis International*, vol. 20, no. 8, pp. 1321–1328, 2009.

[39] M. E. Kersh, S. Martelli, R. Zebaze, E. Seeman, and M. G. Pandy, "Mechanical Loading of the Femoral Neck in Human Locomotion," *Journal of Bone and Mineral Research*, vol. 33, no. 11, pp. 1999–2006, 2018.

[40] J. Wolff, "Das Gesetz der Transformation der Knochen," *Deutsche Medizinische Wochenschrift*, 1893.

[41] J. Wolff, *The Law of Bone Remodelling*, 1986.

[42] M. Taylor, K. Tanner, M. Freeman, and A. Yettram, "Stress and strain distribution within the intact femur: compression or bending? [see comments.]. Comment in: Med Eng Phys. 1997 Jan;19(1):97, 99-100 ; 9140878," *Medical Engineering & Physics*, vol. 18, no. 2, pp. 122–131, 1996.

[43] G. N. Duda, E. Schneider, and E. Y. Chao, "Internal forces and moments in the femur during walking," *Journal of Biomechanics*, 1997.

[44] J. A. Simões, M. A. Vaz, S. Blatcher, and M. Taylor, "Influence of head constraint and muscle forces on the strain distribution within the intact femur," *Medical Engineering and Physics*, vol. 22, no. 7, pp. 453–459, 2000.

[45] N. S. Sverdlova and U. Witzel, "Principles of determination and verification of muscle forces in the human musculoskeletal system: Muscle forces to minimise bending stress," 2010.

[46] A. Morse, M. M. McDonald, N. H. Kelly, K. M. Melville, A. Schindeler, I. Kramer, M. Kneissel, M. C. Van Der Meulen, and D. G. Little, "Mechanical load increases in bone formation via a Sclerostin-independent pathway," *Journal of Bone and Mineral Research*, 2014.

[47] H. M. Frost, "A determinant of bone architecture. The minimum effective strain," *Clinical Orthopaedics and Related Research*, 1983.

[48] H. M. Frost, "From Wolff's law to the Utah paradigm: Insights about bone physiology and its clinical applications," 2001.

[49] M. G. Mullender and R. Huiskes, "Proposal for the regulatory mechanism of Wolff's law," *Journal of Orthopaedic Research*, 1995.

[50] A. E. Goodship, L. E. Lanyon, and H. McFie, "Functional adaptation of bone to increased stress. An experimental study," *Journal of Bone and Joint Surgery - Series A*, 1979.

[51] L. E. Lanyon and D. G. Baggott, "Mechanical function as an influence on the structure and form of bone," *Journal of Bone and Joint Surgery - Series B*, 1976.

[52] T. M. Ryan and R. A. Ketcham, "Angular orientation of trabecular bone in the femoral head and its relationship to hip joint loads in leaping primates," *Journal of Morphology*, 2005.

[53] R. B. Martin, D. B. Burr, N. A. Sharkey, and D. P. Fyhrie, *Skeletal Tissue Mechanics*, 2015.

[54] A. A. Biewener, N. L. Fazzalari, D. D. Konieczynski, and R. V. Baudinette, "Adaptive changes in trabecular architecture in relation to functional strain patterns and disuse," *Bone*, 1996.

[55] W. J. TOBIN, "The internal architecture of the femur and its clinical significance; the upper end." *The Journal of bone and joint surgery. American volume*, 1955.

[56] E. Verhulp, B. van Rietbergen, and R. Huiskes, "Load distribution in the healthy and osteoporotic human proximal femur during a fall to the side," *Bone*, 2008.

[57] J. M. Wallace, "Skeletal Hard Tissue Biomechanics," in *Basic and Applied Bone Biology*, 2013.

[58] D. C. Wirtz, N. Schiffers, R. Forst, T. Pandorf, D. Weichert, and K. Radermacher, "Critical evaluation of known bone material properties to realize anisotropic FE-simulation of the proximal femur," *Journal of Biomechanics*, 2000.

[59] E. Novitskaya, P.-Y. Chen, E. Hamed, L. Jun, V. Lubarda, I. Jasiuk, and J. Mckittrick, "Recent advances on the measurement and calculation of the elastic moduli of cortical and trabecular bone: A review," *Theoretical and Applied Mechanics*, 2011.

[60] J. Fetto, A. Leali, and A. Moroz, "Evolution of the Koch model of the biomechanics of the hip: Clinical perspective," 2002.

[61] J. G. Skedros and S. L. Baucom, "Mathematical analysis of trabecular 'trajectories' in apparent trajectorial structures: The unfortunate historical emphasis on the human proximal femur," *Journal of Theoretical Biology*, 2007.

[62] N. Sverdlova, "Tensile trabeculae - Myth or reality?" 2011.

[63] J. G. Skedros, M. W. Mason, and R. D. Bloebaum, "Modeling and remodeling in a developing artiodactyl calcaneus: A model for evaluating Frost's mechanostat hypothesis and its corollaries," *Anatomical Record*, 2001.

[64] T. M. Keaveny, E. F. Morgan, G. L. Niebur, and O. C. Yeh, "Biomechanics of trabecular bone," 2001.

[65] M. Ganapathi, S. Evans, and P. Roberts, "Strain pattern following surface replacement of the hip," *Proceedings of the Institution of Mechanical Engineers, Part H: Journal of Engineering in Medicine*, 2008.

[66] H. M. Frost, "Skeletal structural adaptations to mechanical usage (SATMU): 1. Redefining Wolff's Law: The bone modeling problem," *The Anatomical Record*, 1990.

[67] L. Peng, J. Bai, X. Zeng, and Y. Zhou, "Comparison of isotropic and orthotropic material property assignments on femoral finite element models under two loading conditions," *Medical Engineering and Physics*, 2006.

[68] J. S. Gregory and R. M. Aspden, "Femoral geometry as a risk factor for osteoporotic hip fracture in men and women," 2008.

[69] J. Thevenot, J. Hirvasniemi, P. Pulkkinen, M. Maäta, R. Korpelainen, S. Saarakkala, and T. Jamsä, "Assessment of risk of femoral neck fracture with radiographic texture parameters: A Retrospective study," *Radiology*, 2014.

[70] S. M. Kazemi, M. Qoreishy, A. Keipourfard, M. M. Sajjadi, and S. Shokraneh, "Effects of hip geometry on fracture patterns of proximal femur," *Archives of Bone and Joint Surgery*, 2016.

[71] M. Viceconti, M. Ansaloni, M. Baleani, and A. Toni, "The muscle standardized femur: A step forward in the replication of numerical studies in biomechanics," *Proceedings of the Institution of Mechanical Engineers, Part H: Journal of Engineering in Medicine*, vol. 217, no. 2, pp. 105–110, 2003.

[72] L. Cristofolini, M. Viceconti, A. Toni, and A. Giunti, "Influence of thigh muscles on the axial strains in a proximal femur during early stance in gait," *Journal of Biomechanics*, vol. 28, no. 5, pp. 617–624, may 1995. [Online]. Available: https://www.ncbi.nlm.nih.gov/pubmed/7775497 http://jbjs.org/article.aspx?doi=10.2106/JBJS.OT.K.00082 https://linkinghub.elsevier.com/retrieve/pii/002192909400106E

[73] J. F. Griffith and H. K. Genant, "New imaging modalities in bone," *Current Rheumatology Reports*, 2011.

[74] D. T. Reilly and A. H. Burstein, "The elastic and ultimate properties of compact bone tissue," *Journal of Biomechanics*, 1975.

[75] F. Katsamanis and D. D. Raftopoulos, "Determination of mechanical properties of human femoral cortical bone by the Hopkinson bar stress technique," *Journal of Biomechanics*, 1990.

[76] J. S. Nyman, H. Leng, X. Neil Dong, and X. Wang, "Differences in the mechanical behavior of cortical bone between compression and tension when subjected to progressive loading," *Journal of the Mechanical Behavior of Biomedical Materials*, 2009.

[77] X. N. Dong and X. E. Guo, "The dependence of transversely isotropic elasticity of human femoral cortical bone on porosity," *Journal of Biomechanics*, 2004.

[78] K. Winwood, P. Zioupos, J. D. Currey, J. R. Cotton, and M. Taylor, "Strain patterns during tensile, compressive, and shear fatigue of human cortical bone and implications for bone biomechanics," *Journal of Biomedical Materials Research - Part A*, 2006.

[79] C. H. Turner, T. Wang, and D. B. Burr, "Shear strength and fatigue properties of human cortical bone determined from pure shear tests," *Calcified Tissue International*, 2001.

[80] S. Saha, "Longitudinal shear properties of human compact bone and its constituents, and the associated failure mechanisms," *Journal of Materials Science*, 1977.

[81] X. N. Dong, Q. Luo, and X. Wang, "Progressive post-yield behavior of human cortical bone in shear," *Bone*, 2013.

[82] H. C. Park and R. S. Lakes, "Cosserat micromechanics of human bone: Strain redistribution by a hydration sensitive constituent," *Journal of Biomechanics*, 1986.

[83] P. Zioupos, M. Gresle, and K. Winwood, "Fatigue strength of human cortical bone: Age, physical, and material heterogeneity effects," *Journal of Biomedical Materials Research - Part A*, 2008.

[84] U. Wolfram and J. Schwiedrzik, "Post-yield and failure properties of cortical bone," *BoneKEy Reports*, 2016.

[85] L. L. Loundagin, I. T. Haider, D. M. Cooper, and W. B. Edwards, "Association between intracortical microarchitecture and the compressive fatigue life of human bone: A pilot study," *Bone Reports*, 2020.

[86] F. G. Evans, "Mechanical properties and histology of cortical bone from younger and older men," *The Anatomical Record*, 1976.

[87] R. W. McCalden, J. A. McGlough, M. B. Barker, and C. M. Court-Brown, "Age-related changes in the tensile properties of cortical bone. The relative importance of changes in porosity, mineralization and microstructure," *Journal of Bone and Joint Surgery - Series A*, 1993.

[88] H. H. Bayraktar, E. F. Morgan, G. L. Niebur, G. E. Morris, E. K. Wong, and T. M. Keaveny, "Comparison of the elastic and yield properties of human femoral trabecular and cortical bone tissue," *Journal of Biomechanics*, 2004.

[89] M. Doblaré, J. M. García, and M. J. Gómez, "Modelling bone tissue fracture and healing: A review," 2004.

[90] M. J. Mirzaali, J. J. Schwiedrzik, S. Thaiwichai, J. P. Best, J. Michler, P. K. Zysset, and U. Wolfram, "Mechanical properties of cortical bone and their relationships with age, gender, composition and microindentation properties in the elderly," *Bone*, 2016.

[91] Y. N. Yeni, C. U. Brown, Z. Wang, and T. L. Norman, "The influence of bone morphology on fracture toughness of the human femur and tibia," *Bone*, 1997.

[92] A. Gustafsson, M. Wallin, and H. Isaksson, "The influence of microstructure on crack propagation in cortical bone at the mesoscale," *Journal of Biomechanics*, 2020.

[93] L. P. Bakalova, C. M. Andreasen, J. S. Thomsen, A. Brüel, E. M. Hauge, B. J. Kiil, J. M. Delaisse, T. L. Andersen, and M. E. Kersh, "Intracortical Bone Mechanics Are Related to Pore Morphology and Remodeling in Human Bone," *Journal of Bone and Mineral Research*, 2018.

[94] P. K. Zysset, X. Edward Guo, C. Edward Hoffler, K. E. Moore, and S. A. Goldstein, "Elastic modulus and hardness of cortical and trabecular bone lamellae measured by nanoindentation in the human femur," *Journal of Biomechanics*, 1999.

[95] B. K. Bay, T. S. Smith, D. P. Fyhrie, and M. Saad, "Digital volume correlation: Three-dimensional strain mapping using x-ray tomography," *Experimental Mechanics*, 1999.

[96] A. I. Hussein, P. E. Barbone, and E. F. Morgan, "Digital volume correlation for study of the mechanics of whole bones," in *Procedia IUTAM*, 2012.

[97] A. Karali, A. P. Kao, J. Zekonyte, G. Blunn, and G. Tozzi, "Micromechanical evaluation of cortical bone using in situ XCT indentation and digital volume correlation," *Journal of the Mechanical Behavior of Biomedical Materials*, 2021.

[98] D. Christen, A. Levchuk, S. Schori, P. Schneider, S. K. Boyd, and R. Müller, "Deformable image registration and 3D strain mapping for the quantitative assessment of cortical bone microdamage," *Journal of the Mechanical Behavior of Biomedical Materials*, 2012.

[99] M. Peña Fernández, A. P. Kao, R. Bonithon, D. Howells, A. J. Bodey, K. Wanelik, F. Witte, R. Johnston, H. Arora, and G. Tozzi, "Time-resolved in situ synchrotron-microCT: 4D deformation of bone and bone analogues using digital volume correlation," *Acta Biomaterialia*, 2021.

[100] R. Zauel, Y. N. Yeni, B. K. Bay, X. N. Dong, and D. P. Fyhrie, "Comparison of the linear finite element prediction of deformation and strain of human cancellous bone to 3D digital volume correlation measurements," *Journal of Biomechanical Engineering*, 2006.

[101] M. R. Hardisty and C. M. Whyne, "Whole bone strain quantification by image registration: A validation study," *Journal of Biomechanical Engineering*, 2009.

[102] J. Kusins, N. Knowles, M. Ryan, E. Dall'Ara, and L. Ferreira, "Full-field comparisons between strains predicted by QCT-derived finite element models of the scapula and experimental strains measured by digital volume correlation," *Journal of Biomechanics*, 2020.

[103] B. C. Roberts, E. Perilli, and K. J. Reynolds, "Application of the digital volume correlation technique for the measurement of displacement and strain fields in bone: A literature review," 2014.

[104] M. Palanca, G. Tozzi, L. Cristofolini, M. Viceconti, and E. Dall'Ara, "Three-dimensional local measurements of bone strain and displacement: Comparison of three digital volume correlation approaches," *Journal of Biomechanical Engineering*, 2015.

[105] L. Liu and E. F. Morgan, "Accuracy and precision of digital volume correlation in quantifying displacements and strains in trabecular bone," *Journal of Biomechanics*, 2007.

[106] B. A. Roeder, K. Kokini, J. P. Robinson, and S. L. Voytik-Harbin, "Local, three-dimensional strain measurements within largely deformed extracellular matrix constructs," *Journal of Biomechanical Engineering*, 2004.

[107] P. Augat and S. Schorlemmer, "The role of cortical bone and its microstructure in bone strength," in *Age and Ageing*, 2006.

[108] D. S. Carlson, G. J. Armelagos, and D. P. Van Gervan, "Patterns of age related cortical bone loss (osteoporosis) within the femoral diaphysis," *Human Biology*, 1976.

[109] J. H. Gosman, Z. R. Hubbell, C. N. Shaw, and T. M. Ryan, "Development of Cortical Bone Geometry in the Human Femoral and Tibial Diaphysis," *Anatomical Record*, 2013.

[110] T. M. Keaveny, T. P. Pinilla, R. P. Crawford, D. L. Kopperdahl, and A. Lou, "Systematic and random errors in compression testing of trabecular bone," *Journal of Orthopaedic Research*, 1997.

[111] C. Öhman, M. Baleani, C. Pani, F. Taddei, M. Alberghini, M. Viceconti, and M. Manfrini, "Compressive behaviour of child and adult cortical bone," *Bone*, 2011.

[112] H. D. Barth, E. A. Zimmermann, E. Schaible, S. Y. Tang, T. Alliston, and R. O. Ritchie, "Characterization of the effects of x-ray irradiation on the hierarchical structure and mechanical properties of human cortical bone," *Biomaterials*, 2011.

[113] H. D. Barth, M. E. Launey, A. A. MacDowell, J. W. Ager, and R. O. Ritchie, "On the effect of X-ray irradiation on the deformation and fracture behavior of human cortical bone," *Bone*, 2010.

APPENDIX A

STRAIN AND ORIENTATION OF ALL REGIONS

Table 9: Median (median absolute deviation) Tensile and Compressive Strains ($\mu\varepsilon$) for 3 loading conditions in the four quadrants of the proximal neck, middle neck, distal neck, pertrochanter and subtrochanter. The median percent change is reported, not percent change of medians. *p<0.05, **p<0.01, *** p<0.001

		Median Tensile Strain ($\mu\varepsilon$)			Median Compressive Strain ($\mu\varepsilon$)		
		Loading 1: "All muscle + JRF"	Loading 2: "Some muscle + JRF"	Loading 3: "JRF only"	Loading 1: "All muscle + JRF"	Loading 2: "Some muscle + JRF"	Loading 3: "JRF only"
Proximal Neck							
Superior	Median	639 (138)	702 (145)	**990 (253)*** **	-871 (318)	-833 (296)	**-599 (104)*** **
	% Change		9.9	56.2		-1.1	-37.4
Posterior	Median	651 (134)	**725 (172)***	**786 (124)*** **	-1556 (224)	**-1672 (221)****	**-1456 (223)*** **
	% Change		9	18.9		6.2	-11.7
Inferior	Median	583 (106)	**655 (134)***	**787 (128)*** **	-1679 (317)	-1762 (358)	**-1990 (271)*** **
	% Change		6.9	30.1		3.8	20
Anterior	Median	474 (101)	490 (99)	**893 (114)*** **	-909 (207)	-859 (227)	**-1274 (312)*** **
	% Change		0.8	85.7		-2.6	43.2
Middle Neck							
Superior	Median	601 (198)	670 (179)	**1440 (275)*** **	-854 (272)	-845 (251)	**-519 (107)*** **
	% Change		20.5	140.7		-6.4	-43.1
Posterior	Median	565 (128)	610 (127)	**836 (191)*** **	-1405 (275)	**-1528 (320)***	**-996 (234)*** **
	% Change		9.1	62.5		10.9	-26.9
Inferior	Median	516 (94)	**544 (102)***	**679 (113)*** **	-1608 (275)	**-1690 (293)***	**-1989 (316)*** **
	% Change		5.3	25.9		4.7	22.2
Anterior	Median	408 (93)	**469 (130)****	**662 (118)*** **	-946 (146)	-914 (174)	**-1276 (270)*** **
	% Change		20.2	41.7		0.7	41.3
Distal Neck							
Superior	Median	657 (128)	714 (134)	**1154 (152)*** **	-1247 (242)	-1238 (204)	**-439 (67)*** **
	% Change		6.7	83.7		-4.3	-67.7
Posterior	Median	449 (95)	478 (95)	**621 (188)****	-944 (159)	-987 (193)	**-566 (82)*** **
	% Change		6.8	32		6	-41.8
Inferior	Median	510 (70)	**531 (66)***	**596 (64)*** **	-1544 (229)	**-1612 (236)***	**-1750 (241)*** **
	% Change		3.8	13.4		3.8	12.7
Anterior	Median	580 (140)	**800 (197)*** **	**369 (66)*** **	-1104 (243)	-1113 (259)	**-702 (122)*** **
	% Change		31.4	-43.1		2.9	-35.9
Pertrochanter							
Lateral	Median	1447 (258)	1424 (240)	**439 (116)*** **	-766 (140)	-766 (119)	**-294 (65)*** **
	% Change		-1.3	-70.9		-1.4	-60.3
Posterior	Median	613 (154)	650 (189)	**481 (91)****	-708 (161)	**-769 (172)***	**-607 (117)*** **
	% Change		4.8	-19		12.5	-19.8
Medial	Median	577 (104)	**645 (76)*** **	**561 (82)****	-1414 (225)	**-1562 (211)*** **	**-1396 (220)****
	% Change		10.8	-3		8.3	-2.4
Anterior	Median	856 (240)	**1019 (255)***	**478 (123)*** **	-996 (228)	-1056 (223)	**-581 (108)*** **
	% Change		15.4	-42.6		6.1	-39.7
Subtrochanter							
Lateral	Median	1369 (321)	1428 (292)	**686 (177)*** **	-536 (111)	**-626 (100)***	**-230 (36)*** **
	% Change		2.2	-46		13.5	-52
Posterior	Median	728 (195)	**861 (181)***	**287 (68)*** **	-741 (162)	**-895 (169)*** **	**-407 (100)*** **
	% Change		11.3	-59.3		26.3	-34.5
Medial	Median	669 (116)	**728 (119)*** **	**492 (83)*** **	-1737 (289)	**-1943 (311)***	**-1515 (251)*** **
	% Change		11.8	-14.9		6.4	-9.6
Anterior	Median	485 (159)	**702 (180)****	**228 (66)*** **	-837 (289)	-895 (231)	**-332 (144)*** **
	% Change		29.6	-54.1		10.6	-53

Table 10: Median (median absolute deviation) Tensile and Compressive Strains ($\mu\varepsilon$) for 3 loading conditions in the four quadrants of the proximal diaphysis, middle diaphysis, and distal diaphysis. The median percent change is reported, not percent change of medians. *p<0.05, **p<0.01, *** p<0.001

		Median Tensile Strain ($\mu\varepsilon$)			Median Compressive Strain ($\mu\varepsilon$)		
		Loading 1: "All muscle + JRF"	Loading 2: "Some muscle + JRF"	Loading 3: "JRF only"	Loading 1: "All muscle + JRF"	Loading 2: "Some muscle + JRF"	Loading 3: "JRF only"
Proximal Diaphysis							
Lateral	Median	1029 (221)	1056 (184)	**283 (65)*** **	-418 (123)	**-571 (138)** **	**-163 (40)*** **
	% Change		2	-69.5		32.1	-59.8
Posterior	Median	610 (167)	**771 (153)** **	**358 (88)*** **	-573 (123)	**-836 (191)*** **	**-915 (179)*** **
	% Change		26.7	-38.8		27.2	37.7
Medial	Median	540 (128)	**603 (122)***	**337 (78)*** **	-1368 (252)	-1455 (271)	**-940 (179)*** **
	% Change		16	-34.3		5.1	-28.1
Anterior	Median	399 (121)	**588 (148)*** **	**215 (53)*** **	-581 (244)	**-681 (164)***	**-151 (42)*** **
	% Change		37.9	-39.3		25.9	-67.6
Middle Diaphysis							
Lateral	Median	598 (210)	**745 (228)** **	**268 (50)*** **	-315 (74)	**-570 (156)*** **	**-650 (202)*** **
	% Change		22.4	-56		61.8	41.3
Posterior	Median	404 (96)	**600 (195)*** **	361 (90)	-639 (159)	**-745 (154)***	**-1039 (239)*** **
	% Change		36.4	-15.2		7.7	47.6
Medial	Median	371 (128)	**521 (128)*** **	323 (146)	-767 (243)	**-945 (214)***	**-288 (81)*** **
	% Change		33.7	-26		10.6	-62.5
Anterior	Median	319 (116)	**524 (163)*** **	380 (135)	-385 (126)	**-671 (216)*** **	**-163 (57)** **
	% Change		49.2	14.2		63.4	-60.2
Distal Diaphysis							
Lateral	Median	319 (126)	**613 (184)*** **	**517 (105)***	-663 (245)	**-1054 (244)*** **	**-1584 (302)*** **
	% Change		53.2	50.2		36.8	99.7
Posterior	Median	339 (103)	**542 (125)*** **	422 (91)	-784 (150)	-744 (106)	**-1268 (263)*** **
	% Change		48.1	16		-1.2	60.9
Medial	Median	470 (113)	**732 (174)*** **	**912 (345)*** **	-358 (130)	**-537 (129)** **	-349 (68)
	% Change		43.6	92.9		34.8	-16.2
Anterior	Median	420 (117)	**557 (173)*** **	**439 (176)***	-357 (186)	**-657 (193)*** **	-306 (56)
	% Change		25.5	18.2		70.3	-30.3

Table 11: 95% (median absolute deviation) Tensile and Compressive Strains ($\mu\varepsilon$) for 3 loading conditions in the four quadrants of the proximal neck, middle neck, distal neck, pertrochanter and subtrochanter. The median percent change is reported, not percent change of medians. *p<0.05, **p<0.01, *** p<0.001

		95% Tensile Strain ($\mu\varepsilon$)			95% Compressive Strain ($\mu\varepsilon$)		
		Loading 1: "All muscle + JRF"	Loading 2: "Some muscle + JRF"	Loading 3: "JRF only"	Loading 1: "All muscle + JRF"	Loading 2: "Some muscle + JRF"	Loading 3: "JRF only"
Proximal Neck							
Superior	Median	853 (151)	1001 (188)	**1709 (388)*** **	-1503 (359)	-1516 (263)	**-1285 (201)** **
	% Change		12.5	76.7		3.5	-17.1
Posterior	Median	870 (169)	970 (202)	**1210 (264)*** **	-2158 (364)	**-2345 (483)*** **	**-2191 (477)***
	% Change		7.9	34		7.1	-1.7
Inferior	Median	812 (188)	820 (176)	**1051 (153)*** **	-2232 (416)	**-2298 (419)***	**-2719 (415)*** **
	% Change		5.4	28.7		4.4	24.2
Anterior	Median	693 (139)	764 (117)	**1179 (161)*** **	-1699 (386)	-1645 (334)	**-2309 (323)*** **
	% Change		1.9	68.9		0.3	33
Middle Neck							
Superior	Median	877 (269)	1042 (291)	**2232 (465)*** **	-1433 (380)	-1268 (290)	**-869 (155)*** **
	% Change		17.3	126		-4.3	-43.9
Posterior	Median	787 (133)	866 (160)	**1458 (395)*** **	-2025 (268)	**-2232 (362)*** **	**-1833 (355)*** **
	% Change		9.6	85.7		11.6	-17.4
Inferior	Median	767 (138)	**830 (138)** **	**1038 (116)*** **	-2219 (286)	**-2445 (352)** **	**-3013 (472)*** **
	% Change		7.6	29.3		8.3	28.7
Anterior	Median	695 (139)	**791 (187)** **	**1029 (194)*** **	-1517 (343)	-1442 (344)	**-2140 (380)*** **
	% Change		21.9	37.2		-2.1	46.5
Distal Neck							
Superior	Median	1274 (375)	1414 (391)	**2007 (355)*** **	-2372 (439)	-2278 (374)	**-725 (105)*** **
	% Change		18	75.7		-8.1	-72.5
Posterior	Median	672 (120)	699 (129)	**1503 (265)*** **	-1488 (246)	**-1655 (292)***	**-1031 (197)*** **
	% Change		8.2	126.3		11.2	-36.2
Inferior	Median	765 (123)	**831 (110)** **	**971 (185)*** **	-2240 (322)	**-2461 (343)** **	**-2921 (512)*** **
	% Change		8.7	20.5		7.9	21.9
Anterior	Median	1193 (358)	**1410 (379)*** **	**819 (166)*** **	-1648 (293)	-1671 (315)	-1580 (284)
	% Change		32.9	-33.1		1.1	3.6
Pertrochanter							
Lateral	Median	2791 (678)	2666 (699)	**1123 (217)*** **	-2019 (628)	-1998 (635)	**-542 (116)*** **
	% Change		-2.6	-61.4		-0.9	-74.6
Posterior	Median	1491 (321)	1542 (462)	**1059 (254)*** **	-1562 (291)	-1525 (243)	**-927 (150)*** **
	% Change		-2.1	-30.8		6.1	-34
Medial	Median	908 (89)	**1012 (125)** **	**834 (125)** **	-2678 (334)	**-2747 (414)** **	**-2449 (301)*** **
	% Change		10.5	-8.8		3.4	-4.5
Anterior	Median	1455 (331)	**1577 (391)** **	**896 (204)*** **	-1668 (315)	-1751 (266)	**-966 (198)*** **
	% Change		11.6	-30		2.2	-35
Subtrochanter							
Lateral	Median	2205 (501)	2175 (442)	**1142 (236)*** **	-805 (142)	-894 (170)	**-426 (88)*** **
	% Change		-0.4	-41.2		7.3	-43
Posterior	Median	1678 (351)	1603 (366)	**651 (219)*** **	-1359 (231)	**-1595 (290)*** **	-1267 (223)
	% Change		-1.4	-60.3		22	-0.2
Medial	Median	917 (189)	**1041 (199)*** **	**717 (113)*** **	-2531 (426)	-2706 (503)	**-2260 (359)*** **
	% Change		11.9	-13.4		4	-11
Anterior	Median	836 (183)	**1086 (232)***	**537 (140)*** **	-1725 (224)	-1742 (255)	**-1396 (376)*** **
	% Change		22.4	-31.8		-1.7	-22.2

Table 12: 95% (median absolute deviation) Tensile and Compressive Strains ($\mu\varepsilon$) for 3 loading conditions in the four quadrants of the proximal diaphysis, middle diaphysis, and distal diaphysis. The median percent change is reported, not percent change of medians. *p<0.05, **p<0.01, *** p<0.001

		95% Tensile Strain ($\mu\varepsilon$)			95% Compressive Strain ($\mu\varepsilon$)		
		Loading 1: "All muscle + JRF"	Loading 2: "Some muscle + JRF"	Loading 3: "JRF only"	Loading 1: "All muscle + JRF"	Loading 2: "Some muscle + JRF"	Loading 3: "JRF only"
Proximal Diaphysis							
Lateral	Median	1808 (406)	1735 (329)	**757 (147)*** **	-654 (195)	-947 (251)	-611 (255)
	% Change		0.1	-53.8		25.6	-27.4
Posterior	Median	1219 (273)	1417 (233)	**497 (105)*** **	-1199 (254)	**-1418 (259)*** **	**-1326 (208)** **
	% Change		14.7	-57.3		16.8	15.3
Medial	Median	743 (182)	883 (224)	526 (98)	-2052 (360)	-2117 (329)	**-1604 (240)*** **
	% Change		17.4	-26		4	-20.9
Anterior	Median	809 (235)	**1013 (250)*** **	**507 (136)*** **	-1371 (252)	-1460 (308)	**-557 (221)*** **
	% Change		20.2	-29		4.3	-54.4
Middle Diaphysis							
Lateral	Median	1055 (305)	**1329 (330)** **	**478 (125)*** **	-681 (201)	**-1067 (279)*** **	**-1515 (241)*** **
	% Change		18.2	-46.7		43	97.8
Posterior	Median	746 (247)	**1129 (262)*** **	**590 (150)***	-999 (267)	**-1329 (320)** **	**-1602 (413)*** **
	% Change		47	-26.1		11.7	43.3
Medial	Median	640 (231)	**913 (262)*** **	**924 (276)***	-1306 (309)	**-1589 (417)***	**-682 (245)*** **
	% Change		38.5	39.3		7.2	-46.1
Anterior	Median	563 (180)	**862 (258)** **	**890 (302)*** **	-743 (299)	**-1056 (288)*** **	**-391 (125)** **
	% Change		40.3	46.4		30	-54.8
Distal Diaphysis							
Lateral	Median	505 (178)	**905 (272)*** **	**833 (117)***	-1221 (330)	**-1568 (352)** **	**-2667 (377)*** **
	% Change		46.1	63.6		19.5	96.2
Posterior	Median	543 (190)	**1017 (290)*** **	763 (175)	-1241 (251)	-1321 (243)	**-2323 (581)*** **
	% Change		68.9	41.1		7.5	82.1
Medial	Median	849 (198)	**1148 (232)*** **	**1763 (344)*** **	-707 (167)	**-977 (283)** **	-611 (127)
	% Change		40.8	114.8		16.3	-18.5
Anterior	Median	762 (173)	**865 (210)***	**1348 (412)*** **	-522 (243)	**-978 (238)*** **	-767 (203)
	% Change		20.1	80.7		58.2	15

Table 13: Median (median absolute deviation) Tensile and Compressive Alpha Orientation (°) for 3 loading conditions in four quadrants of the proximal neck, middle neck, distal neck, pertrochanter, and subtrochanter. The median percent change is reported, not percent change of medians. *p<0.05, **p<0.01, *** p<0.001

		Tensile Orientation Alpha (°)			Compressive Orientation Alpha (°)		
		Loading 1: "All muscle + JRF"	Loading 2: "Some muscle + JRF"	Loading 3: "JRF only"	Loading 1: "All muscle + JRF"	Loading 2: "Some muscle + JRF"	Loading 3: "JRF only"
Proximal Neck							
Superior	Median	70.5 (13.9)	60.2 (15.5)	149.3 (23.6)	136.9 (19.6)	128.8 (17.6)	**62.4 (10.3)*** **
	% Change		-10	36.5		-11.9	-54.1
Posterior	Median	62.6 (15.4)	55.2 (11.9)	133.5 (43.5)	29.4 (18)	112.4 (50.6)	80.7 (40.3)
	% Change		-8.2	104.7		20.7	23.2
Inferior	Median	41 (15.9)	43.2 (12.8)	**99.6 (48.9)*** **	133 (20.7)	128.1 (13.5)	146.3 (13.8)
	% Change		20.3	115.5		-6.8	11.9
Anterior	Median	115.8 (45.4)	142.7 (34.9)	154.8 (7.2)	134.3 (17.2)	**112.3 (14.1)*** **	**114.1 (7.1)***
	% Change		-4.5	21.1		-20.2	-9.4
Middle Neck							
Superior	Median	65.4 (24.4)	53.7 (18.8)	**160.7 (8.1)*** **	154.9 (13.5)	**129.6 (18.1)***	**99.7 (43)*** **
	% Change		-2.8	133.4		-10.4	-30.1
Posterior	Median	80.3 (10.5)	79.1 (20.4)	**157.3 (10.4)** **	152.3 (16.9)	158.6 (11.2)	**75.9 (31.1)** **
	% Change		-1.3	69		3.8	-45.1
Inferior	Median	71 (48.6)	58 (21.1)	129.9 (19.3)	144.1 (17.2)	139.9 (16.2)	148.5 (10.8)
	% Change		-1.6	64		-2.2	8.2
Anterior	Median	49.9 (25.5)	38.6 (22.5)	**158.3 (10)*** **	95.5 (35.4)	83.8 (26.6)	**113.9 (15.8)***
	% Change		-2.2	72.4		-15.6	6.6
Distal Neck							
Superior	Median	70 (26.9)	67.2 (28)	**152.9 (15.5)***	152.9 (5.2)	145.9 (6.9)	**39.4 (35.1)*** **
	% Change		-1.5	82		-1	-60.5
Posterior	Median	82.8 (7.5)	77.4 (6.3)	**147 (8.3)*** **	147.5 (20.5)	139.1 (19.7)	139.7 (35.8)
	% Change		-2.9	81.3		-0.6	5.1
Inferior	Median	72.6 (46.1)	78.6 (38.2)	71.8 (44.1)	122.8 (27.3)	121 (23)	143.5 (15.1)
	% Change		-8.5	-4.2		6.4	21
Anterior	Median	142.3 (28.3)	**161.8 (12.4)***	100.3 (27.2)	35.8 (26.2)	29.4 (22)	35.2 (29.5)
	% Change		7.5	0.9		-26.7	14.8
Pertrochanter							
Lateral	Median	53.7 (28.9)	50.8 (22.2)	**112.4 (29.6)***	122.6 (32.7)	85.5 (38)	114.8 (39.4)
	% Change		6.4	68.6		-1.3	-13.1
Posterior	Median	71.8 (45.1)	151.8 (22)	76.4 (38.6)	152.9 (16.5)	155.2 (12.6)	142.6 (33.5)
	% Change		2.4	-7.4		2.6	-7
Medial	Median	69.4 (22.4)	**111.4 (39.9)** **	55.8 (20.6)	78.4 (39.9)	**115.5 (30)***	**131.6 (23.2)** **
	% Change		39.5	-8.1		14.6	36
Anterior	Median	123.6 (25.4)	140.7 (19.3)	108.9 (54.2)	160.4 (10.2)	154.4 (18)	152.4 (18.5)
	% Change		2.1	8.8		-0.4	-6.2
Subtrochanter							
Lateral	Median	57.6 (42.4)	48.9 (19.5)	**155.8 (10.9)*** **	113.3 (43.1)	97.4 (23.7)	64.6 (62.5)
	% Change		-33	182.7		-17.5	-10.1
Posterior	Median	155.9 (9.6)	155.7 (13.4)	111.1 (49.1)	151.1 (21.7)	137.3 (39.1)	52 (50.7)
	% Change		-2.3	-12.4		-5.7	-27.2
Medial	Median	90.3 (20.5)	98.9 (16.5)	92.7 (33.4)	91.7 (32.2)	91.5 (29.5)	86.1 (63.7)
	% Change		5.8	-7.3		-1.1	11.5
Anterior	Median	112.1 (46.2)	149.6 (21.9)	90.8 (46.5)	156.4 (11.7)	156 (12.1)	156.1 (18)
	% Change		2.3	-5.4		-1.6	-1.9

Table 14: Median (median absolute deviation) Tensile and Compressive Alpha Orientation (°) for 3 loading conditions in four quadrants of the proximal diaphysis, middle diaphysis, and distal diaphysis. The median percent change is reported, not percent change of medians. *p<0.05, **p<0.01, *** p<0.001

		Tensile Orientation Alpha (°)			Compressive Orientation Alpha (°)		
		Loading 1: "All muscle + JRF"	Loading 2: "Some muscle + JRF"	Loading 3: "JRF only"	Loading 1: "All muscle + JRF"	Loading 2: "Some muscle + JRF"	Loading 3: "JRF only"
Proximal Diaphysis							
Lateral	Median	35.7 (22)	57.6 (29.7)	**115.3 (49.4)****	51.7 (26.6)	79.2 (20.6)	70 (39.9)
	% Change		29.9	69.1		67.3	27.3
Posterior	Median	152.5 (13.1)	138.6 (26)	**128.5 (24.5)***	147.4 (26.3)	155.2 (15.5)	100.8 (51.2)
	% Change		-1.5	-15.1		4.5	3
Medial	Median	95.2 (9.4)	97.3 (26)	112.7 (18.8)	67 (15.6)	81.3 (29.1)	53.8 (35.4)
	% Change		2.1	10.6		23.9	-2.8
Anterior	Median	136 (30.5)	142.7 (26.6)	146.8 (15.7)	143.6 (18.8)	150.9 (20.3)	113.6 (47.7)
	% Change		-2.5	9.1		9.6	-9
Middle Diaphysis							
Lateral	Median	56.1 (16.4)	57.9 (13.8)	45.2 (16.1)	97 (33.1)	103.7 (32.7)	101 (45.8)
	% Change		9.1	-24.7		-4.7	5.6
Posterior	Median	134 (27.5)	29.8 (17.6)	91.3 (57.8)	119.7 (28.2)	123.3 (36.7)	99.3 (21.6)
	% Change		-27	-6.6		4.6	-12.5
Medial	Median	97.5 (23)	109.6 (18.4)	115.5 (17.5)	94.5 (9.8)	86.1 (21.8)	99.7 (16)
	% Change		3.2	13.3		1.1	14.2
Anterior	Median	133 (42.2)	32.1 (30.3)	146.3 (30.9)	156.8 (16.2)	144.3 (32.3)	133.9 (34.7)
	% Change		-7.8	-0.2		-4.4	-6.3
Distal Diaphysis							
Lateral	Median	77.6 (15.4)	62 (14.8)	61.5 (20.5)	84.2 (25.7)	75.1 (29.9)	87.1 (58.4)
	% Change		-26.6	-31.5		-2.1	35.1
Posterior	Median	43.1 (42.8)	148.5 (19)	50.2 (36.5)	116.4 (43.9)	126.4 (25.7)	95.5 (30.8)
	% Change		18.3	15.2		1.7	-8.2
Medial	Median	118.7 (21.4)	98.6 (32.7)	**26.4 (20.2)****	91.2 (23.8)	73.9 (28.8)	107 (44.4)
	% Change		-19.3	-78.1		7.4	8.8
Anterior	Median	143.9 (19.8)	133.3 (36.1)	**45.3 (40.9)***	120.9 (53.3)	68 (57.4)	118 (33)
	% Change		1.3	-22.7		-16	-4.6

Table 15: Median (median absolute deviation) Tensile and Compressive Beta Orientation (°) for 3 loading conditions in four quadrants of the proximal neck, middle neck, distal neck, pertrochanter, and subtrochanter. The median percent change is reported, not percent change of medians. *p<0.05, **p<0.01, *** p<0.001

		Tensile Orientation Beta (°)			Compressive Orientation Beta (°)		
		Loading 1: "All muscle + JRF"	Loading 2: "Some muscle + JRF"	Loading 3: "JRF only"	Loading 1: "All muscle + JRF"	Loading 2: "Some muscle + JRF"	Loading 3: "JRF only"
Proximal Neck							
Superior	Median	36.7 (9.2)	43.1 (18.7)	34.1 (19)	65.1 (18.4)	67.3 (10)	**106.3 (8)*** **
	% Change		0.8	-26.2		-1	55.3
Posterior	Median	148.6 (22.1)	168.7 (10.5)	164.9 (5.4)	58.7 (9)	64.5 (9.4)	**84.9 (6.3)*** **
	% Change		8.2	8.5		0.6	37.1
Inferior	Median	145 (24.5)	149.4 (27.7)	**160.4 (4.7)***	60.7 (14.4)	57.6 (10.4)	64.7 (11.9)
	% Change		4.9	14.1		-6.8	0.6
Anterior	Median	144.9 (14.2)	152.2 (20.5)	**160.7 (5.6)***	64.1 (7.5)	73.3 (12.5)	**80 (7.2)***
	% Change		5.1	8.8		5.4	16.4
Middle Neck							
Superior	Median	36.5 (8.7)	39.8 (11.3)	26.7 (6.1)	54.1 (43.2)	47.8 (26)	**116.1 (9.3)** **
	% Change		-4.7	-27.1		21.6	117.3
Posterior	Median	119.9 (57.2)	100.1 (60.3)	27.8 (20.7)	70.5 (11.8)	67.7 (4.8)	**99.5 (3.4)*** **
	% Change		-20	-77.4		0.7	42.1
Inferior	Median	152.3 (10)	144.5 (28.6)	153.7 (6.1)	66.2 (10.1)	71.1 (7.1)	65.7 (8.1)
	% Change		-0.7	1		2	1.1
Anterior	Median	25.6 (16.6)	23 (6.6)	**166.5 (9.9)** **	80.6 (13.7)	93.3 (13.9)	81.1 (5)
	% Change		16.6	93.5		17.3	-0.2
Distal Neck							
Superior	Median	54.6 (24.8)	60.7 (23.2)	34 (9.2)	146.3 (12.5)	141.3 (7.4)	118.7 (8.5)
	% Change		3.5	-31.4		-5.8	-18.7
Posterior	Median	56.3 (42.7)	44.9 (28)	32.1 (11.6)	61.1 (35.6)	83.6 (37.4)	**116.7 (7.5)** **
	% Change		-21.7	-32.2		-3.3	90.9
Inferior	Median	140.8 (27.5)	136.6 (37.4)	157.5 (14.8)	80.7 (8.8)	78.3 (7.2)	**73.9 (5.4)*** **
	% Change		-2.6	8.4		-5.6	-7.6
Anterior	Median	30.3 (7.5)	36.8 (3.8)	**47.9 (17.6)***	120.1 (10.3)	126.6 (10.1)	118.5 (18.8)
	% Change		30	50.6		2.5	-2.6
Pertrochanter							
Lateral	Median	100.3 (8.8)	101 (14.6)	81.3 (12.1)	30.2 (20.2)	49.3 (29.2)	134.8 (34.8)
	% Change		-4.4	-14.9		11.3	29.5
Posterior	Median	100.2 (41)	123.3 (14.6)	**41.2 (20.6)*** **	79.9 (44.8)	94.5 (52.3)	**127.5 (20.7)***
	% Change		6.3	-55.2		-0.8	58.4
Medial	Median	33.1 (28)	104.3 (67.2)	162.7 (13.6)	89.3 (6.1)	**81.9 (5.1)***	**82.8 (5)** **
	% Change		3.2	47.2		-8.2	-7.3
Anterior	Median	67.5 (14.5)	54.3 (8.6)	56 (11.8)	131.5 (10.4)	136.5 (7.6)	153.2 (9.4)
	% Change		-2.1	-5.4		0.9	6.5
Subtrochanter							
Lateral	Median	98.8 (6)	100.5 (4.2)	99.9 (2.2)	21.9 (12.1)	54.6 (37)	12 (3.4)
	% Change		2.4	0.3		49.1	-36.9
Posterior	Median	121.1 (12.8)	131.9 (6.8)	139.7 (27.4)	53.7 (20.1)	54.1 (15.6)	78 (16.1)
	% Change		4.9	19.1		7.9	41.3
Medial	Median	112.3 (54.4)	94.1 (58.7)	14 (11.9)	90.7 (5.2)	91 (7.4)	90.3 (5.7)
	% Change		4.3	-59.8		3.5	-0.1
Anterior	Median	41 (17.1)	53 (14.2)	42 (35)	120.9 (9.8)	125.2 (11.7)	103.2 (12.8)
	% Change		13.7	2.5		4.2	-10.6

Table 16: Median (median absolute deviation) Tensile and Compressive Beta Orientation (°) for 3 loading conditions in four quadrants of the proximal diaphysis, middle diaphysis, and distal diaphysis. The median percent change is reported, not percent change of medians. *p<0.05, **p<0.01, *** p<0.001

		Tensile Orientation Beta (°)			Compressive Orientation Beta (°)		
		Loading 1: "All muscle + JRF"	Loading 2: "Some muscle + JRF"	Loading 3: "JRF only"	Loading 1: "All muscle + JRF"	Loading 2: "Some muscle + JRF"	Loading 3: "JRF only"
Proximal Diaphysis							
Lateral	Median	102 (4)	101.6 (8.9)	**107.2 (8.9)****	30 (14)	**56.6 (26.5)***	37.2 (30.9)
	% Change		-0.6	4.5		121.2	27.3
Posterior	Median	146 (5.5)	143.2 (5.6)	167.2 (5.8)	61.3 (6.8)	61.6 (7.3)	**86.4 (3.9)***
	% Change		-0.7	14.6		-2.6	40.3
Medial	Median	116.6 (27.1)	111.5 (54.2)	114.5 (61.3)	96.3 (5.2)	94.2 (7.6)	96.5 (3.9)
	% Change		-13	6.5		-3.9	-1.9
Anterior	Median	45.8 (15)	55.1 (14.9)	**107.7 (10.9)*****	126.1 (15.9)	132.7 (14.2)	**43.2 (30.7)*****
	% Change		24.2	108.5		5.4	-63.6
Middle Diaphysis							
Lateral	Median	104.7 (7.8)	115.5 (5.4)	53.9 (52.8)	109.7 (42.4)	96.1 (27.3)	92.8 (4.6)
	% Change		6.1	-46.8		-7.2	-20
Posterior	Median	147.8 (8.2)	147.8 (5)	154.5 (23.4)	75 (9)	65.4 (5.6)	**88.6 (3.8)*****
	% Change		-1.2	8.8		-9	21.6
Medial	Median	107.8 (33.8)	119.2 (17.9)	105.5 (17.2)	88.5 (6.8)	94.1 (9.7)	**74.1 (21.5)*****
	% Change		11	0.8		1.1	-28.7
Anterior	Median	54 (7.6)	52 (8.8)	**108.1 (6.8)*****	138.5 (15.8)	133.9 (5)	**26.1 (15.8)*****
	% Change		2.6	89.6		-6.1	-75.3
Distal Diaphysis							
Lateral	Median	89.7 (41.1)	**131.7 (17.7)***	**5.8 (4)*****	88.6 (8.1)	86.7 (13.8)	92.7 (2.8)
	% Change		42.4	-91.8		0.3	3
Posterior	Median	158.2 (13.2)	145.1 (10.9)	171.4 (7.3)	78.5 (4.5)	64.9 (4.6)	**89.4 (2.5)***
	% Change		-7.2	9		-15.2	13.4
Medial	Median	101.6 (11.6)	87.5 (17.4)	100.5 (1.8)	82.9 (21.3)	105.7 (29.1)	**13.6 (7.5)*****
	% Change		-8.6	-2.2		-4.8	-80.4
Anterior	Median	64.5 (32.5)	50.4 (3.8)	**99.1 (6.9)***	97 (44.3)	133.9 (6.4)	13.1 (8.3)
	% Change		-9.8	53.6		3.7	-72.3

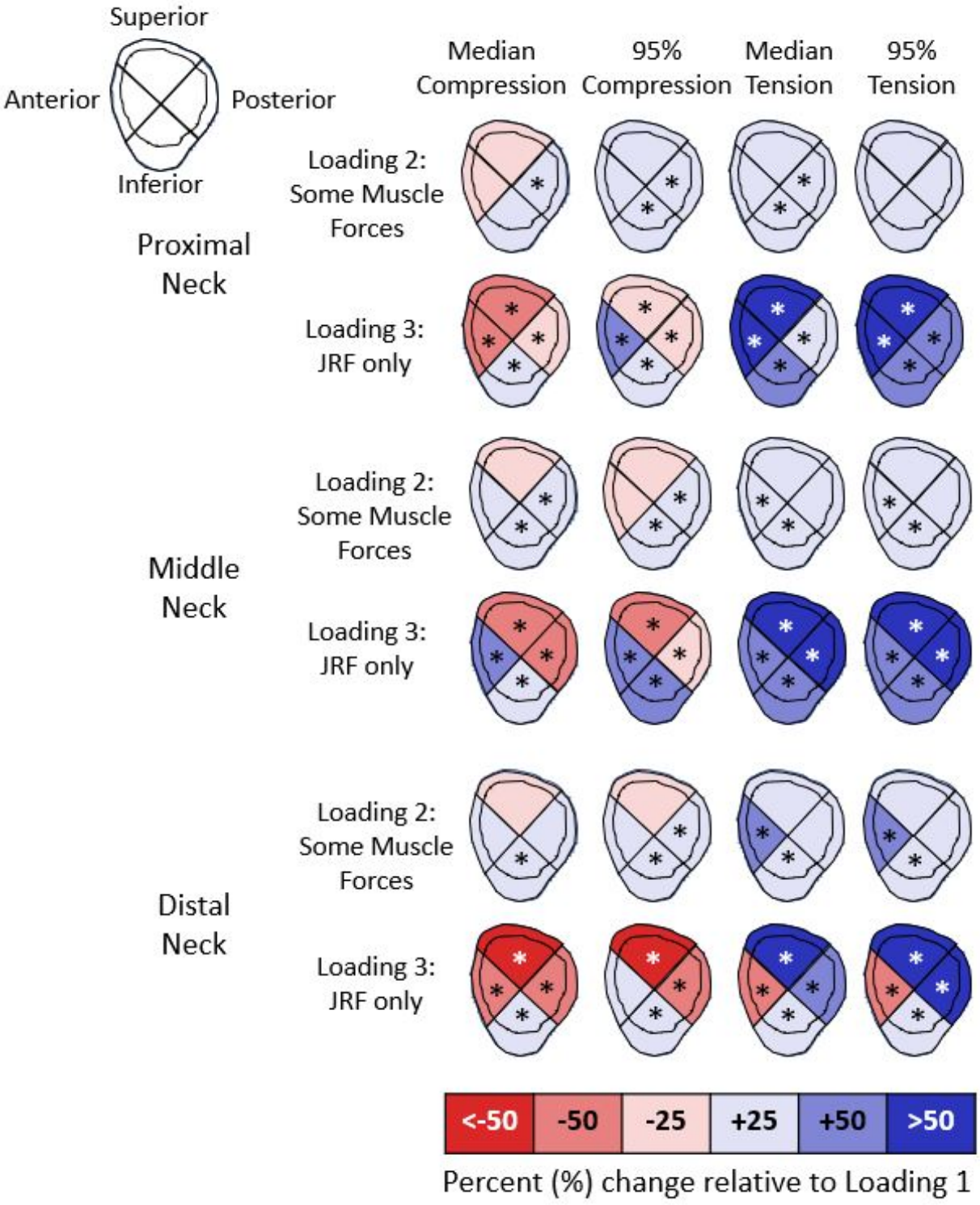

Figure 27: Percent change in loading condition 2 and 3 relative to loading condition 1 for median compressive and tensile strains in four quadrants of the proximal neck, middle neck and distal neck. *$p<0.05$

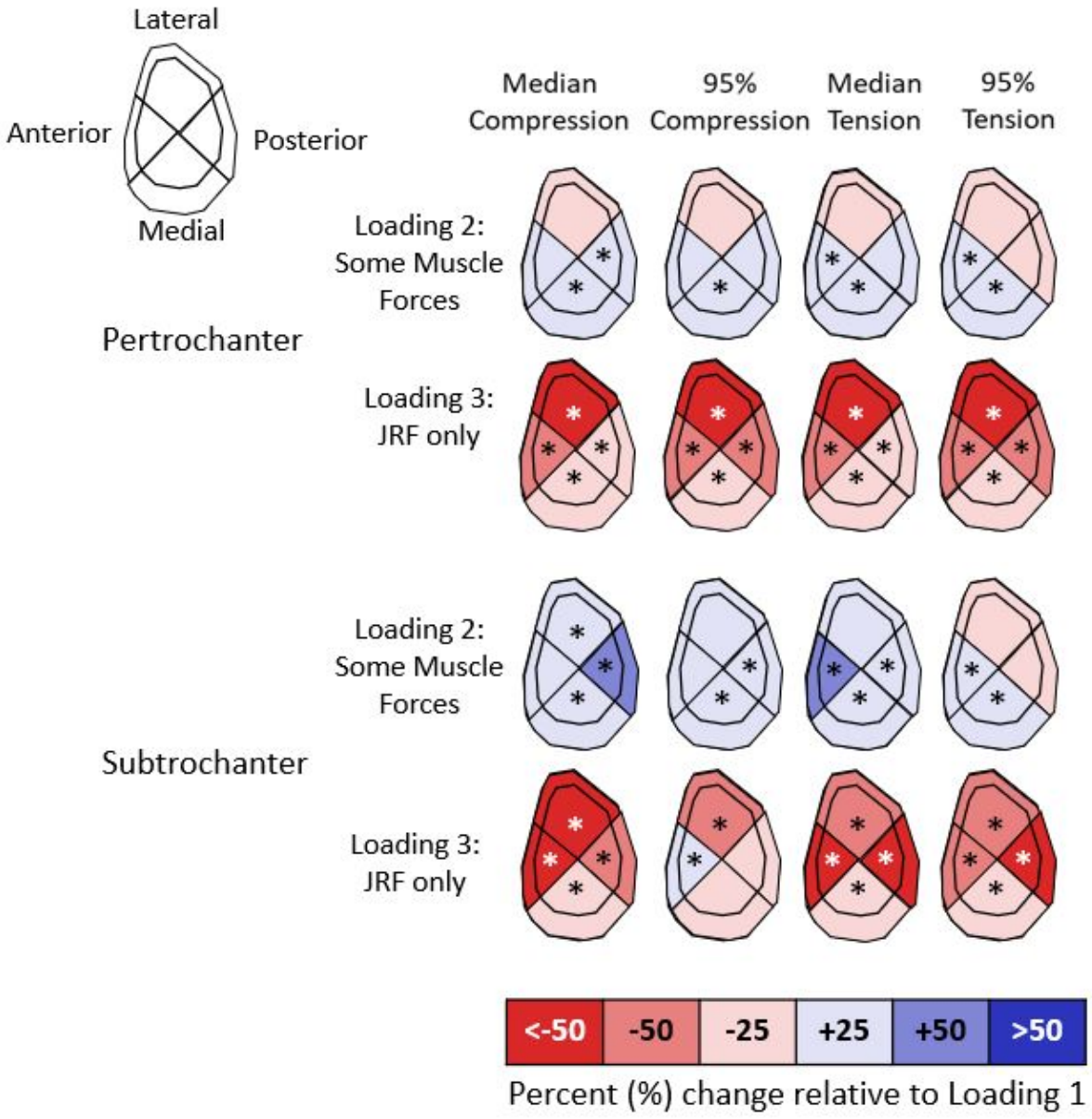

Figure 28: Percent change in loading condition 2 and 3 relative to loading condition 1 for median compressive and tensile strains in four quadrants of the pertrochanter and subtrochanter. *p<0.05

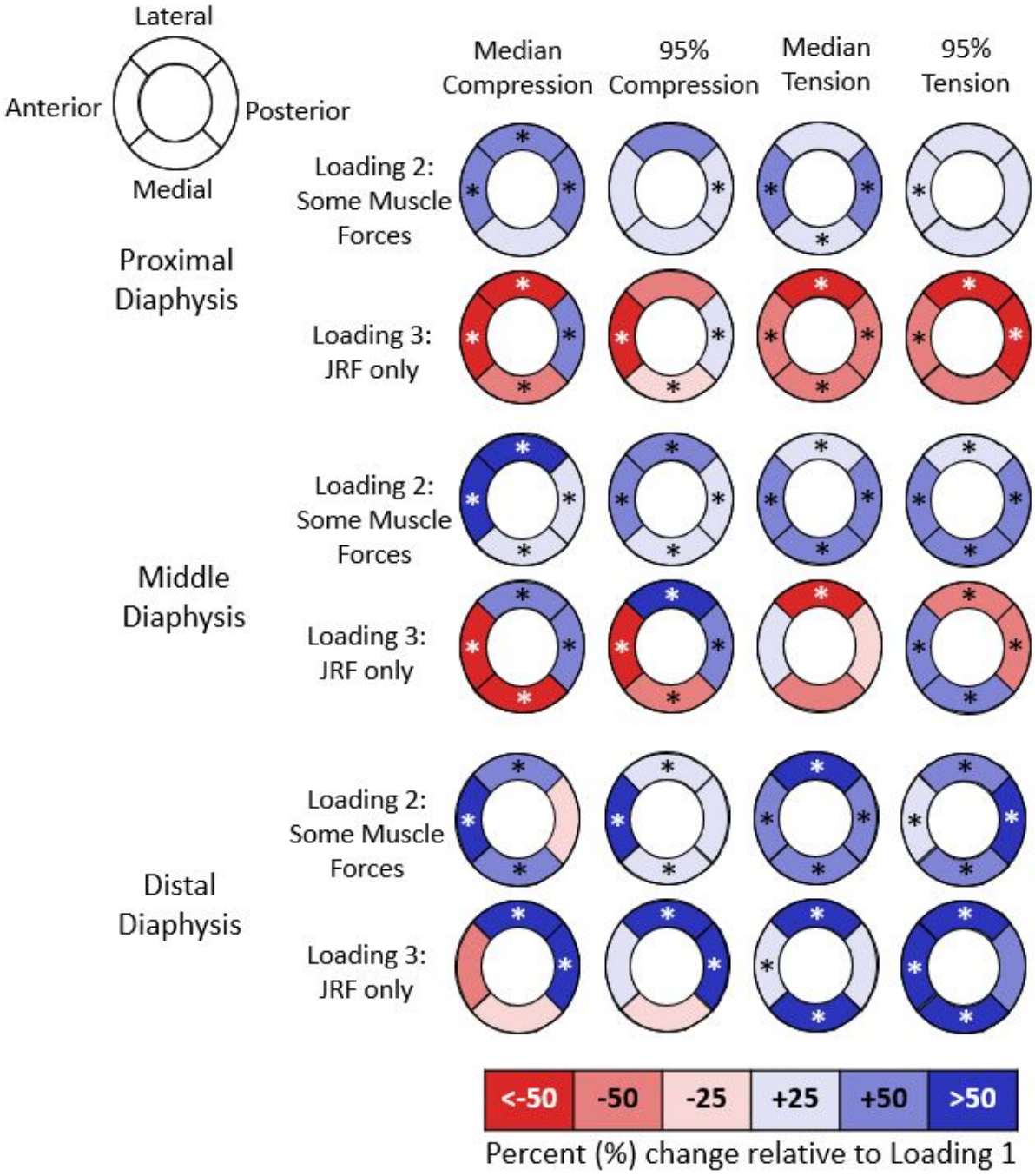

Figure 29: Percent change in loading condition 2 and 3 relative to loading condition 1 for median compressive and tensile strains in four quadrants of the proximal diaphysis, middle diaphysis, and distal diaphysis. Asterisks denote $p<0.05$.

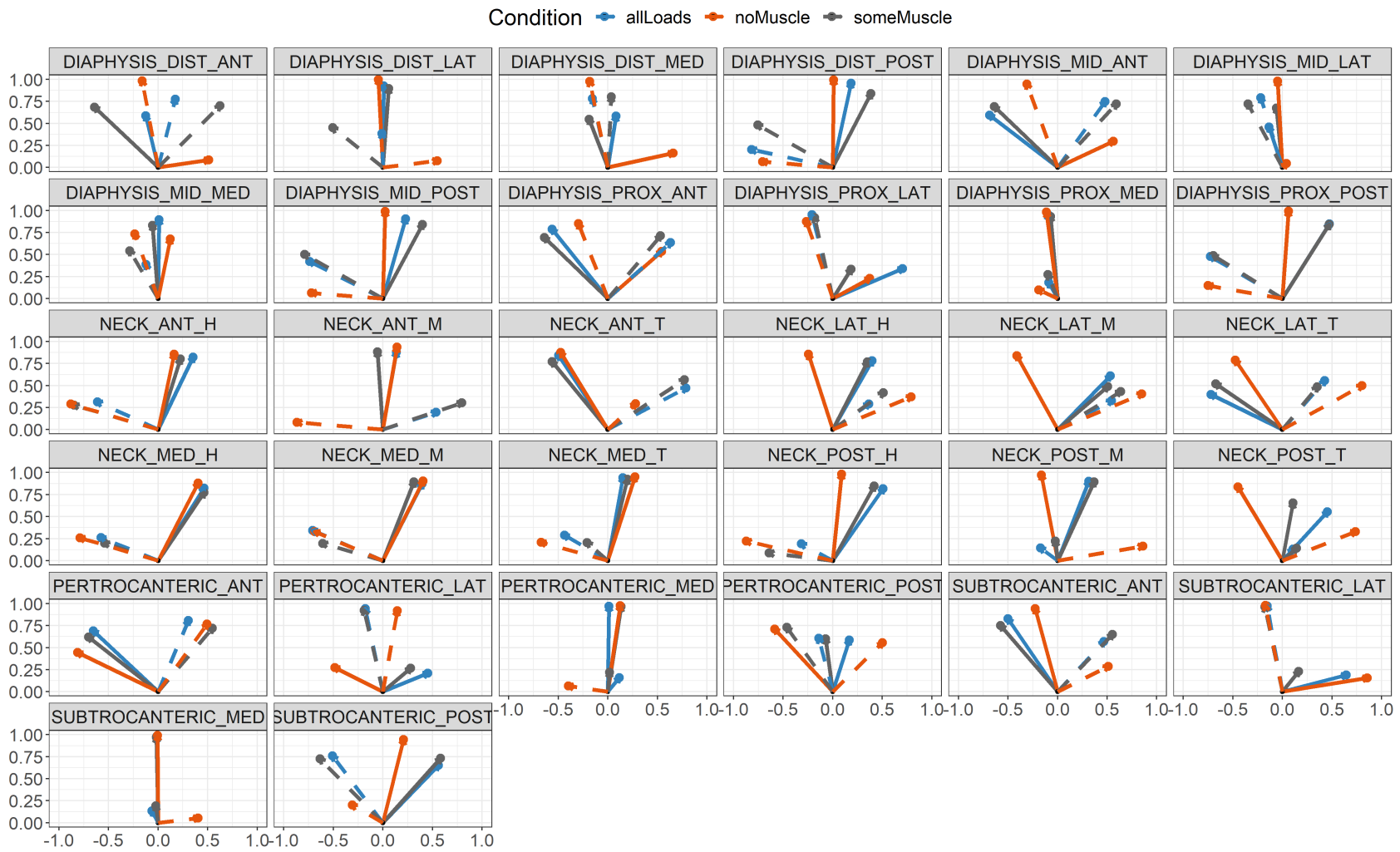

Figure 30: Median tensile and compressive beta orientation for 3 loading conditions in four quadrants of the proximal neck, middle neck, distal neck, pertrochanter, subtrochanter, proximal diaphysis, middle diaphysis, and distal diaphysis. Dashed lines denote compressive orientation while solid lines denote tensile orientation.

APPENDIX B

SAMPLE PREPARATION, DVC ERROR DOE, AND LOADED DVC

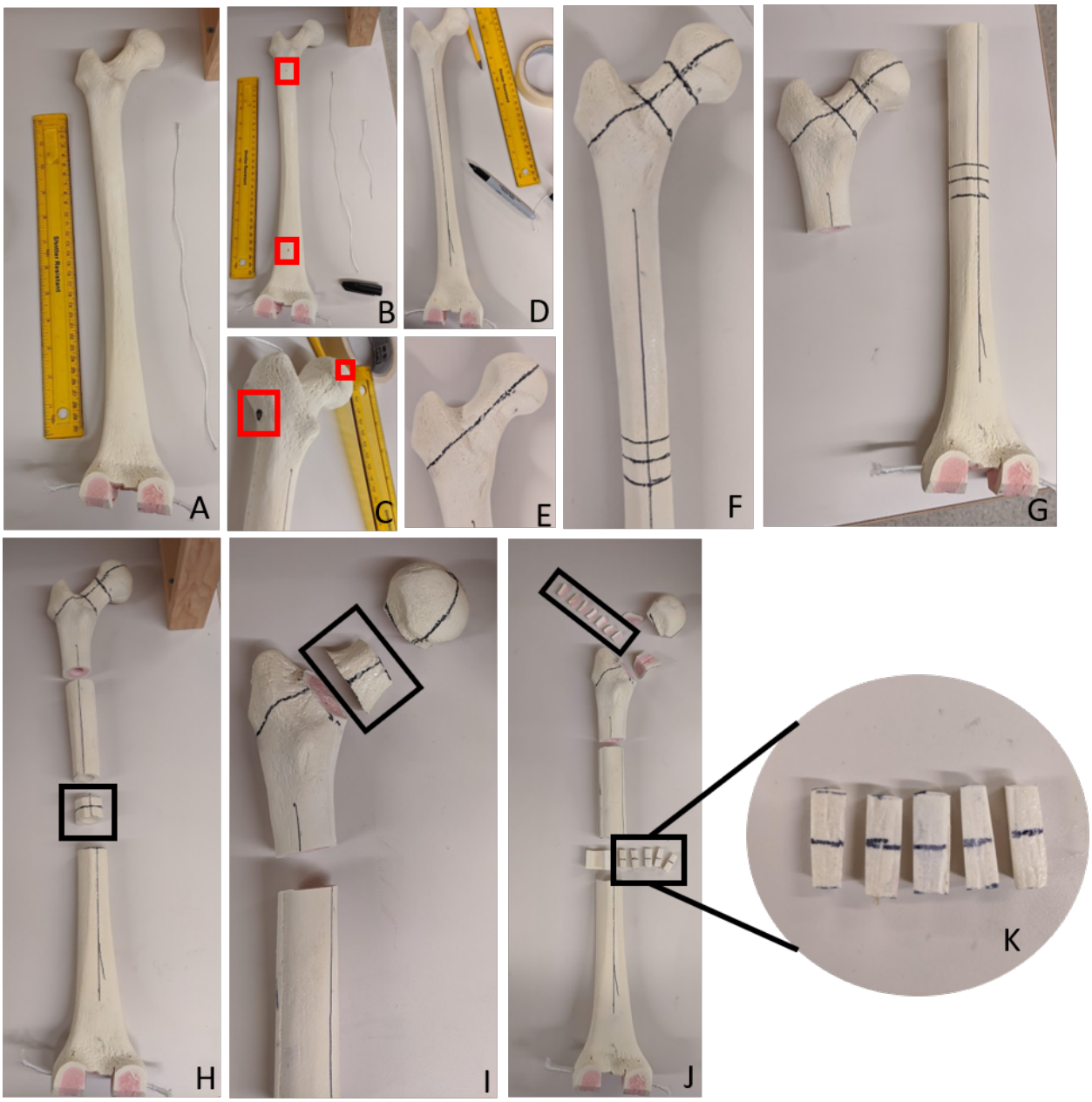

Figure 31: Saw bone and materials (A), Label center of marrow cavity at lower level of lesser trochanter and center of marrow cavity at upper level of femoral condyle (B), Label base of lateral side of greater trochanter and apex of femoral head (not visible in picture) (C), Draw shaft anatomical axis (D), Draw femoral neck axis (E), Draw sections perpendicular to the two axes (F), Outline practicing femoral neck sectioning on saw bones (G-K), Initial cut separating diaphysis from proximal femur (G), Cut section normal to shaft anatomical axis (H), Cut section normal to femoral neck axis (I), Cut femoral neck section into superior–inferior halves, and cut diaphysis section into lateral–medial halves (J), and Cut halves into final 5mm wide specimens (K).

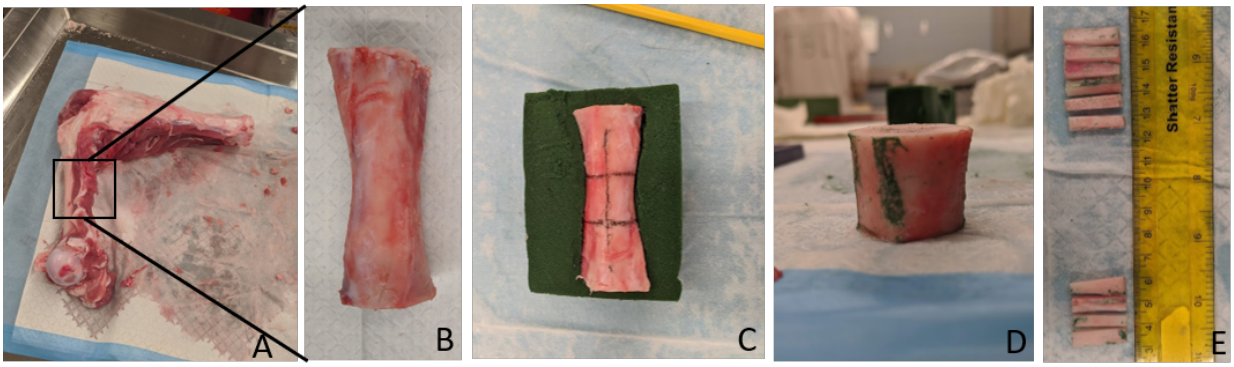

Figure 32: Porcine femur (A-B), Specimen placed on floral foam to ease diamond saw use (C), Middle femur sectioned (D), and 5mm wide specimen sectioned (E).

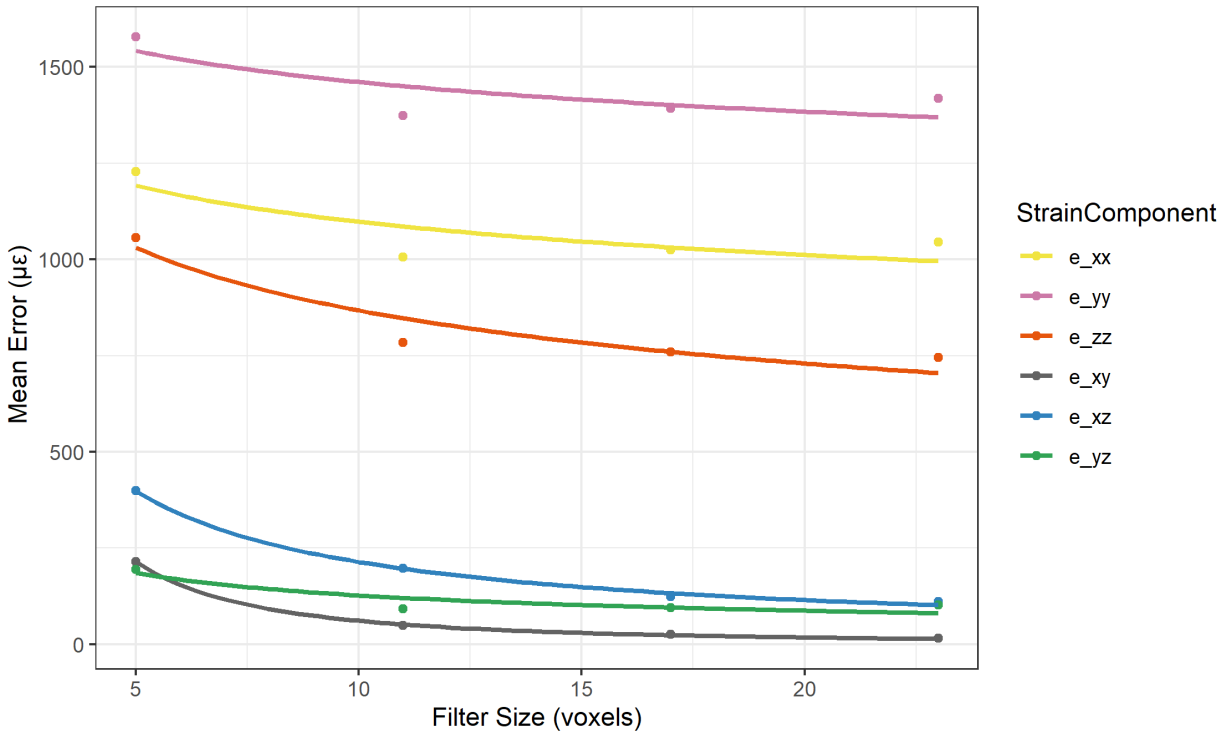

Figure 33: Absolute mean error in the middle diaphysis as a function of strain filter size

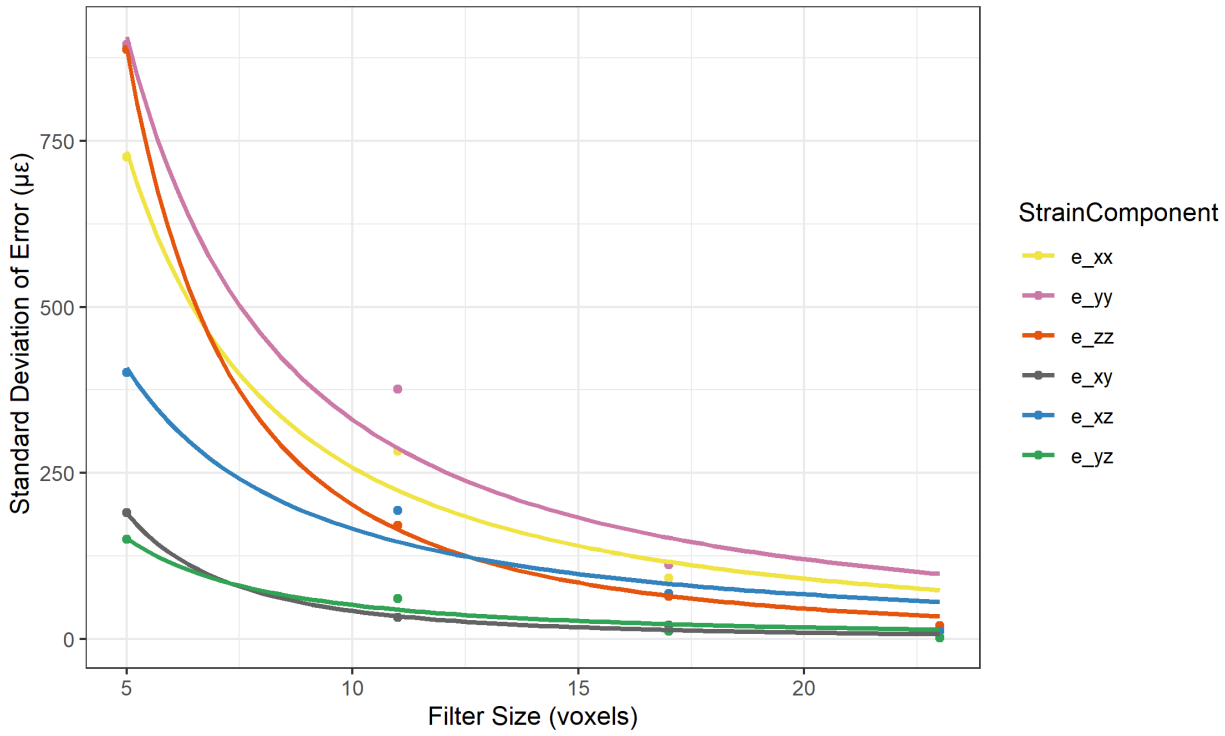

Figure 34: Absolute standard deviation of error in the middle diaphysis as a function filter size

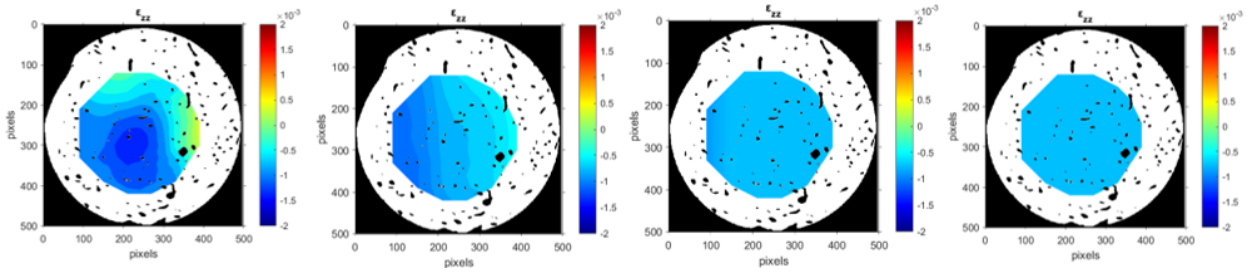

Figure 35: Effect of filter size on ε_{xx} for the same micro-CT slice of the middle diaphysis specimen

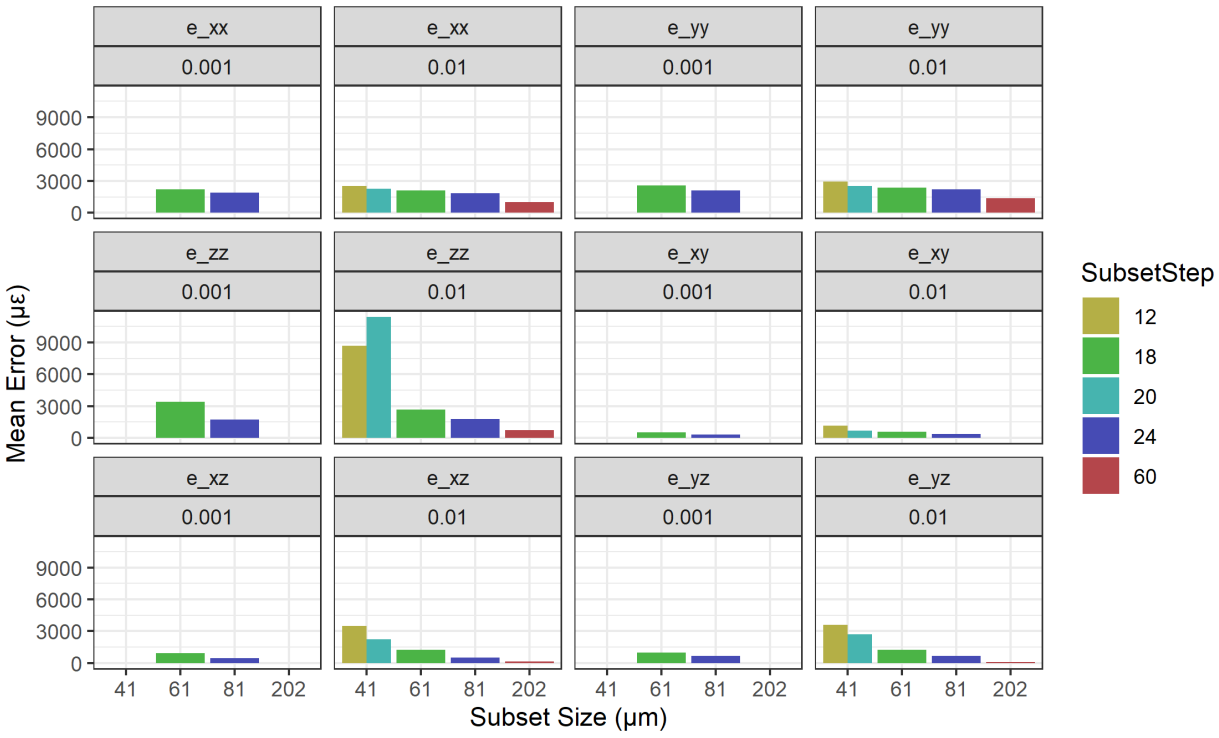

Figure 36: Absolute mean error in the middle diaphysis for the design of experiments

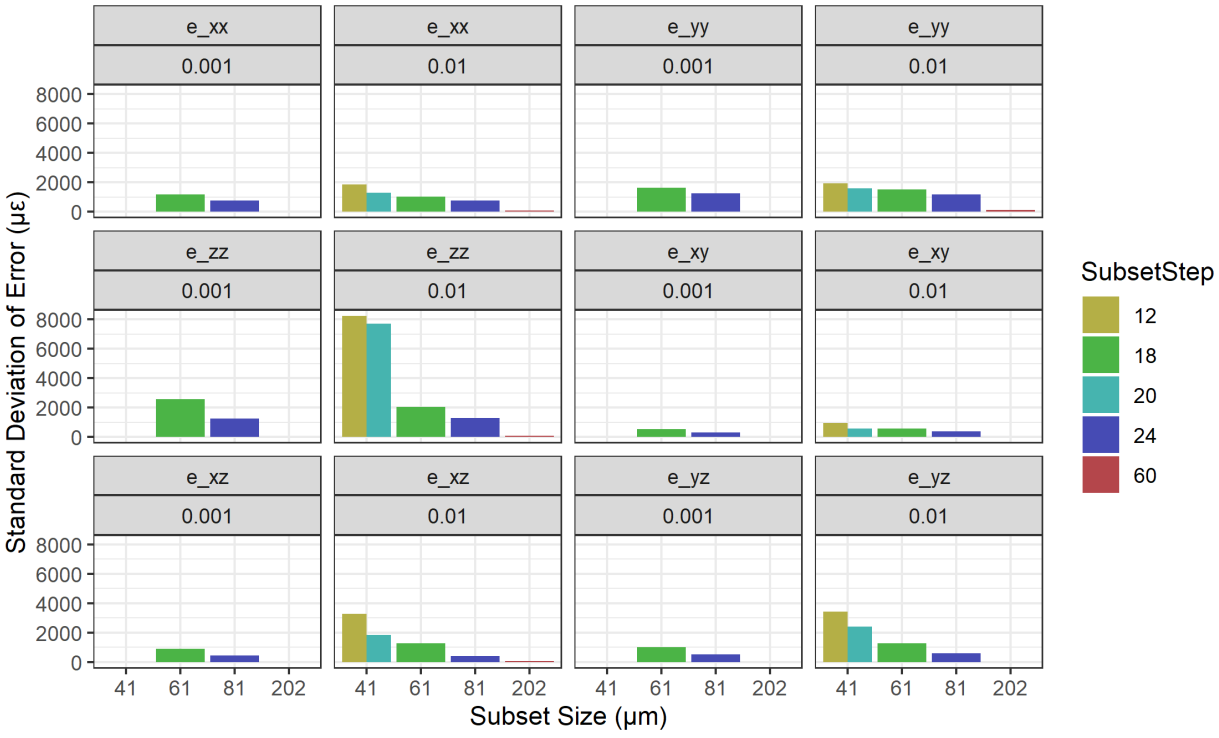

Figure 37: Absolute standard deviation of error in the middle diaphysis for the design on experiments

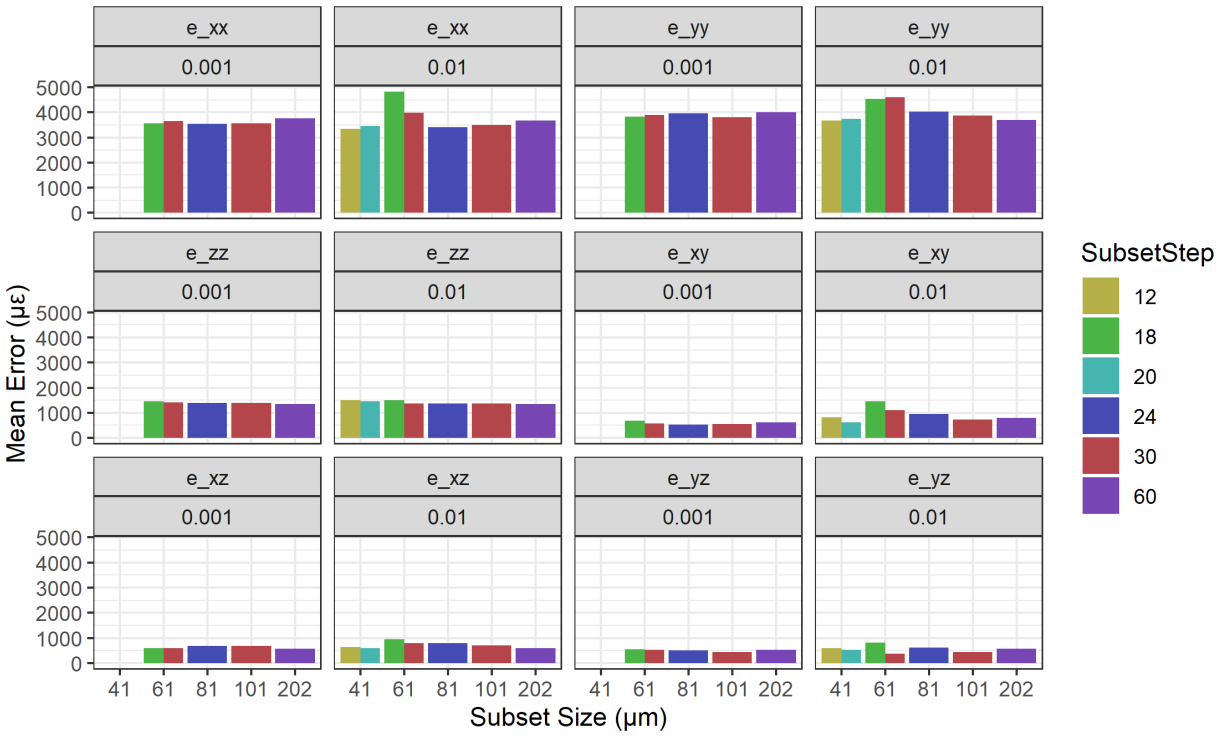

Figure 38: Absolute mean error in the inferior neck for the design of experiments

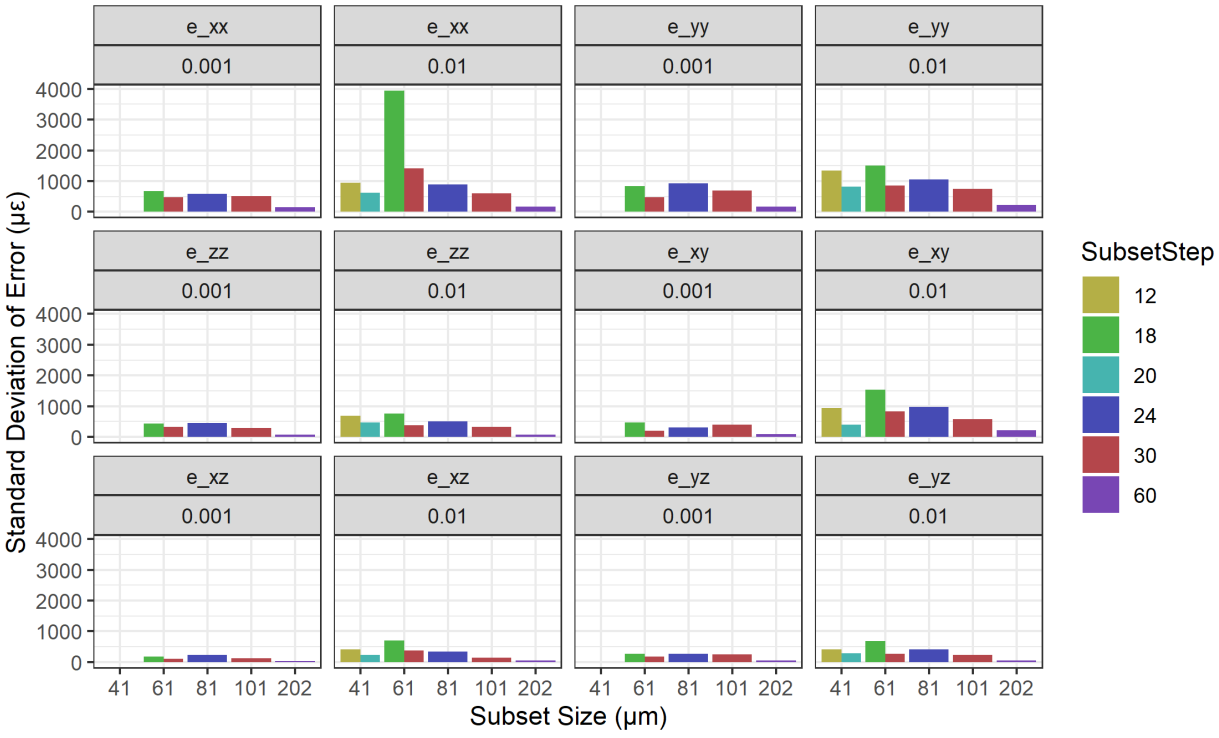

Figure 39: Absolute standard deviation of error in the inferior neck for the design of experiments

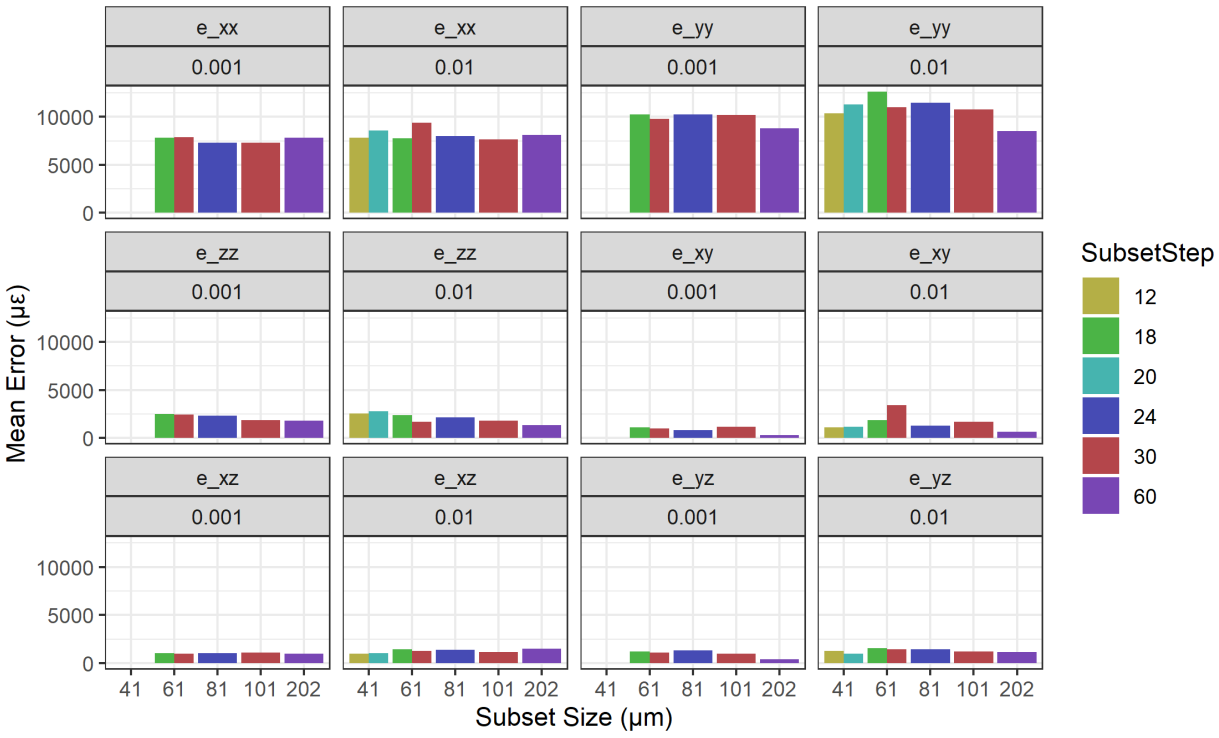

Figure 40: Absolute mean error in the superior neck for the design of experiments

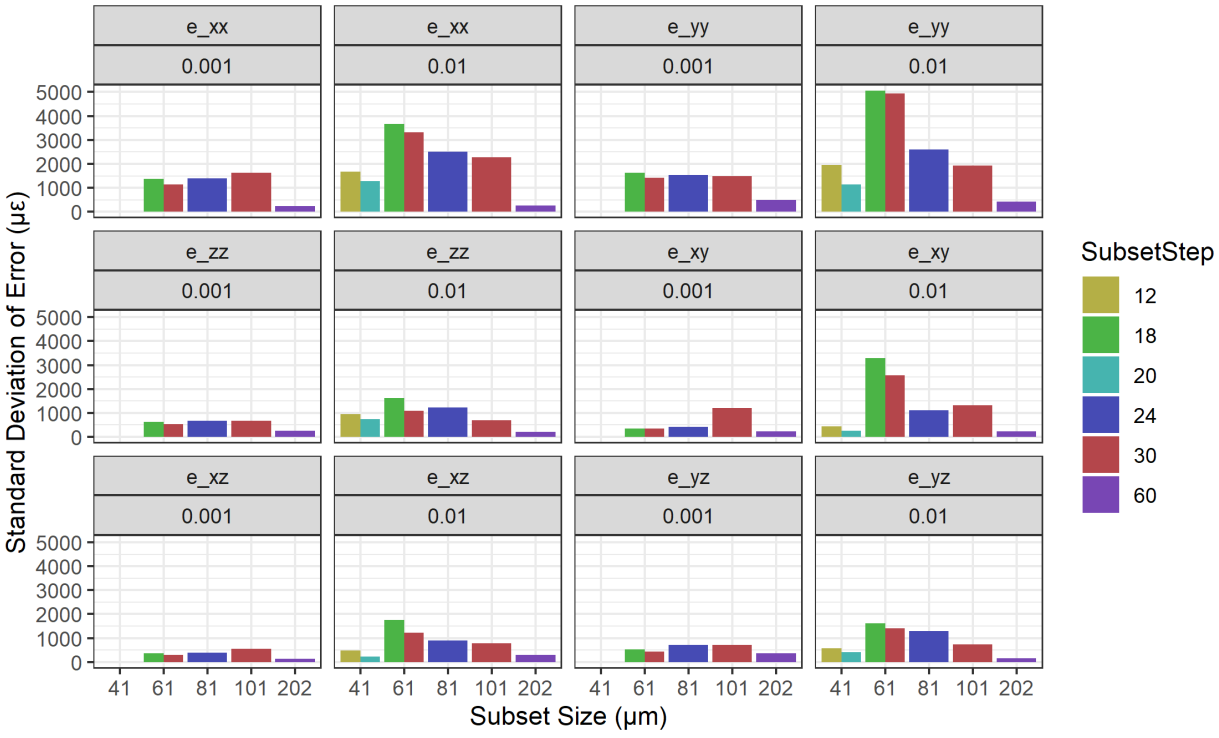

Figure 41: Absolute standard deviation of error in the superior neck for the design of experiments

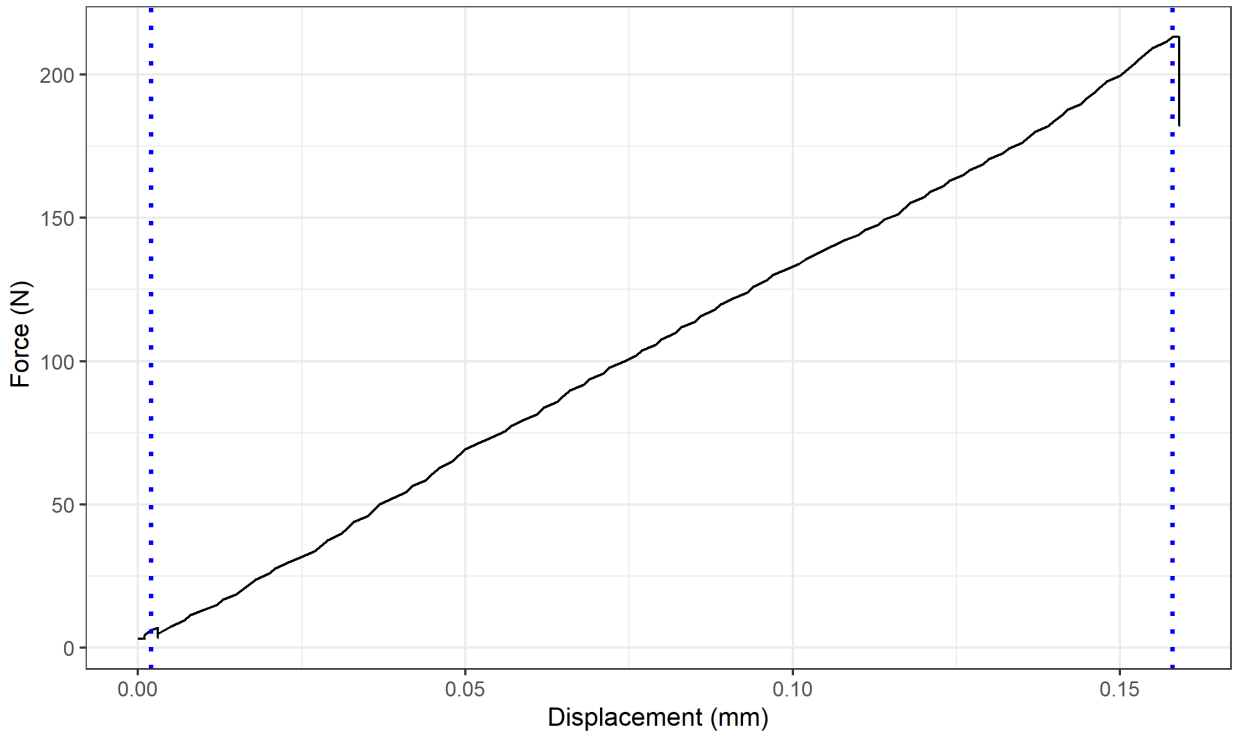

Figure 42: Load-displacement curve for loaded DVC experiment of middle diaphysis specimen

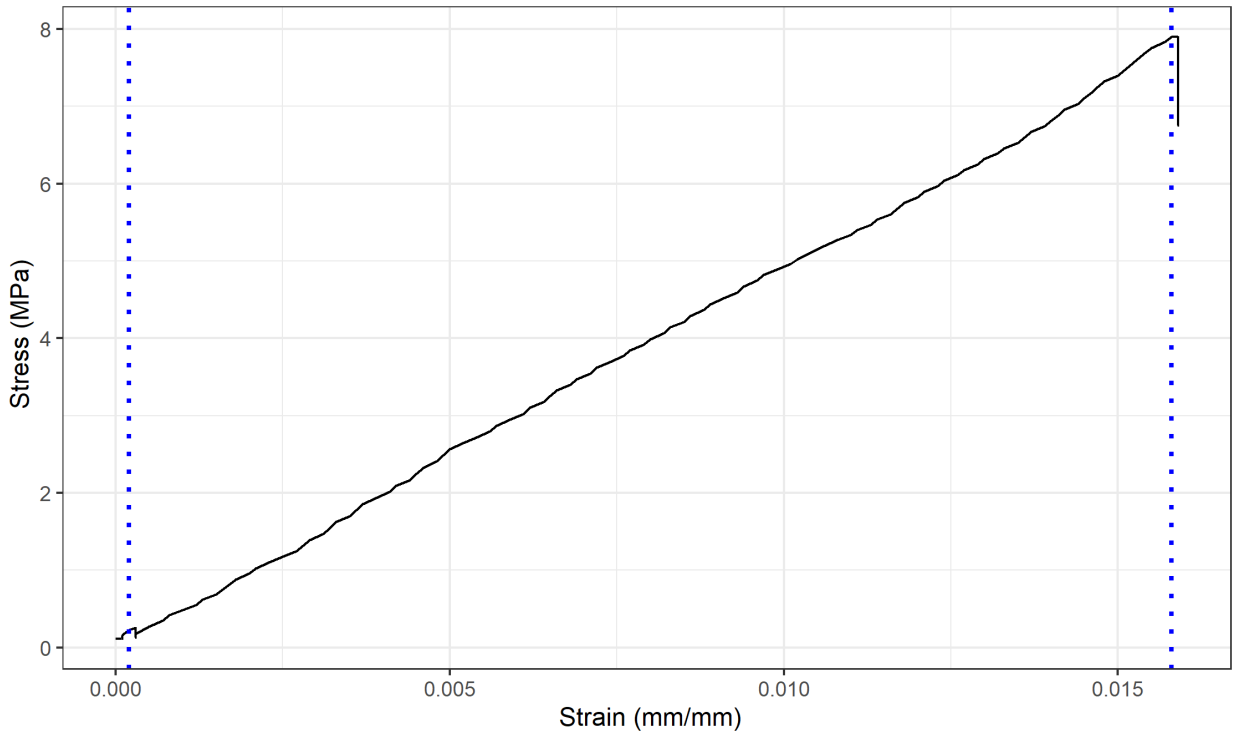

Figure 43: Stress-strain curve for loaded DVC experiment of middle diaphysis specimen

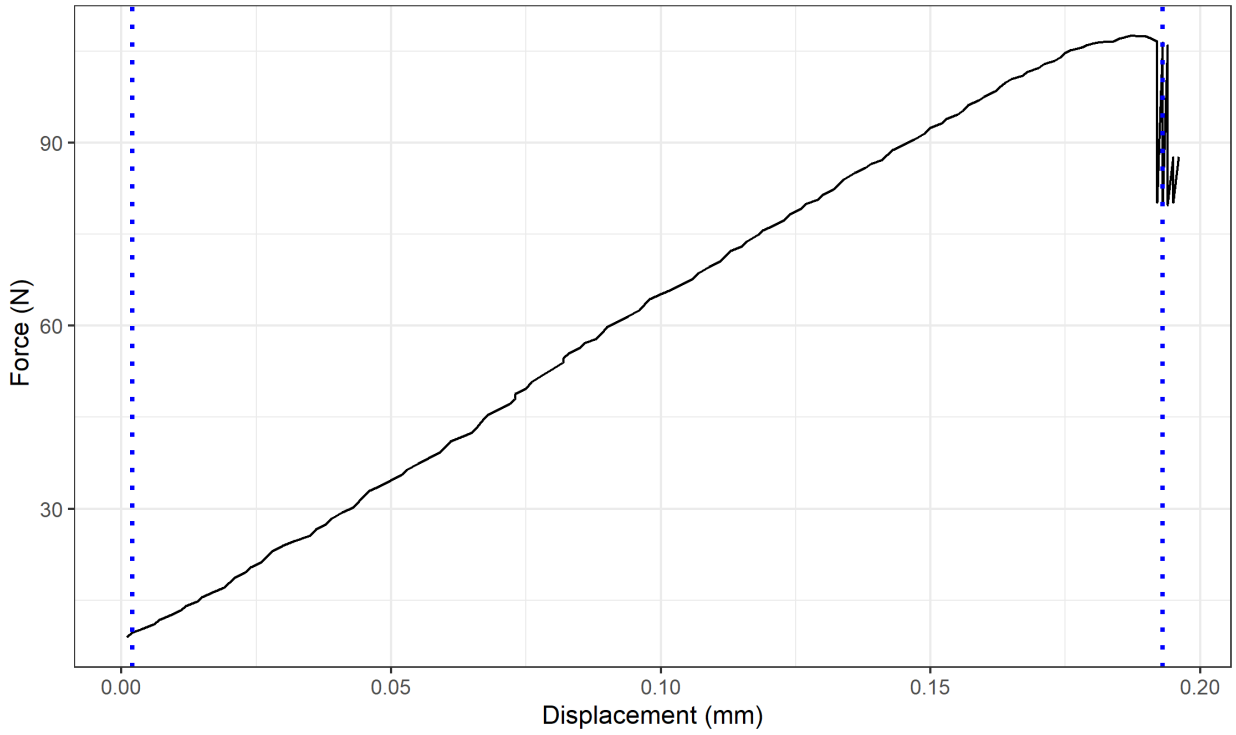

Figure 44: Load-displacement curve for loaded DVC experiment of inferior neck specimen

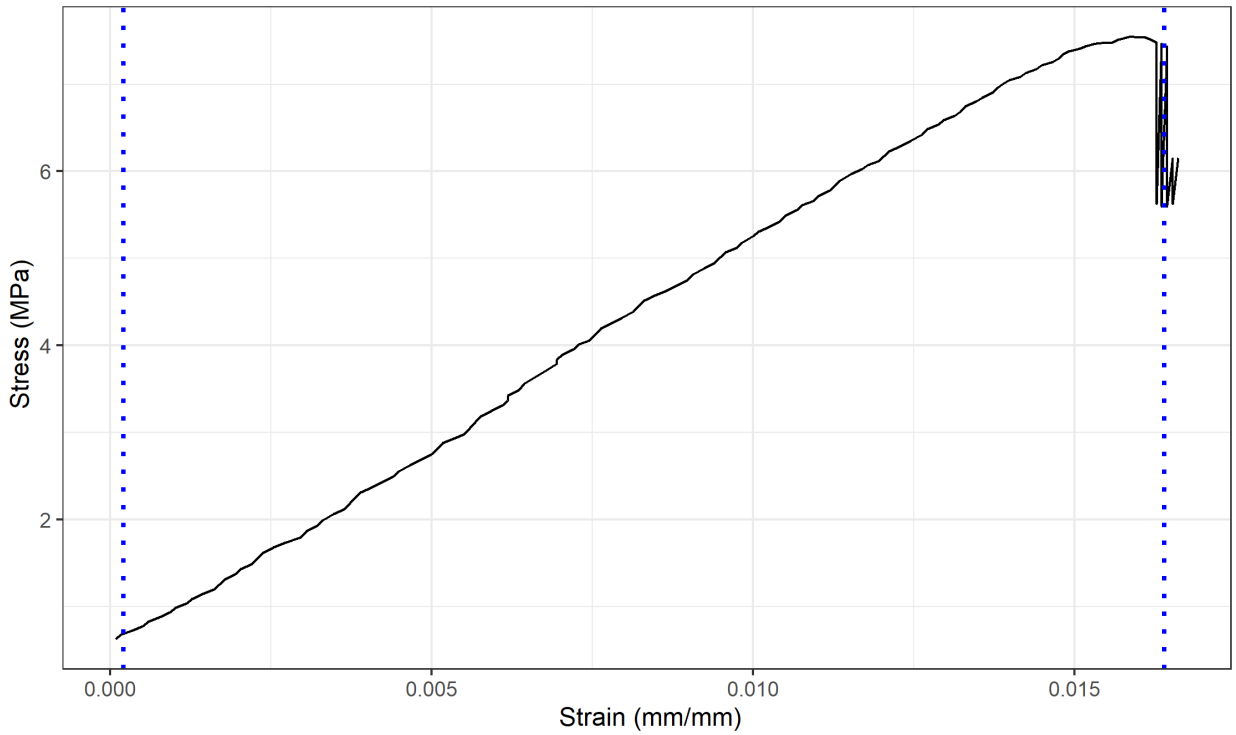

Figure 45: Stress-strain curve for loaded DVC experiment of inferior neck specimen

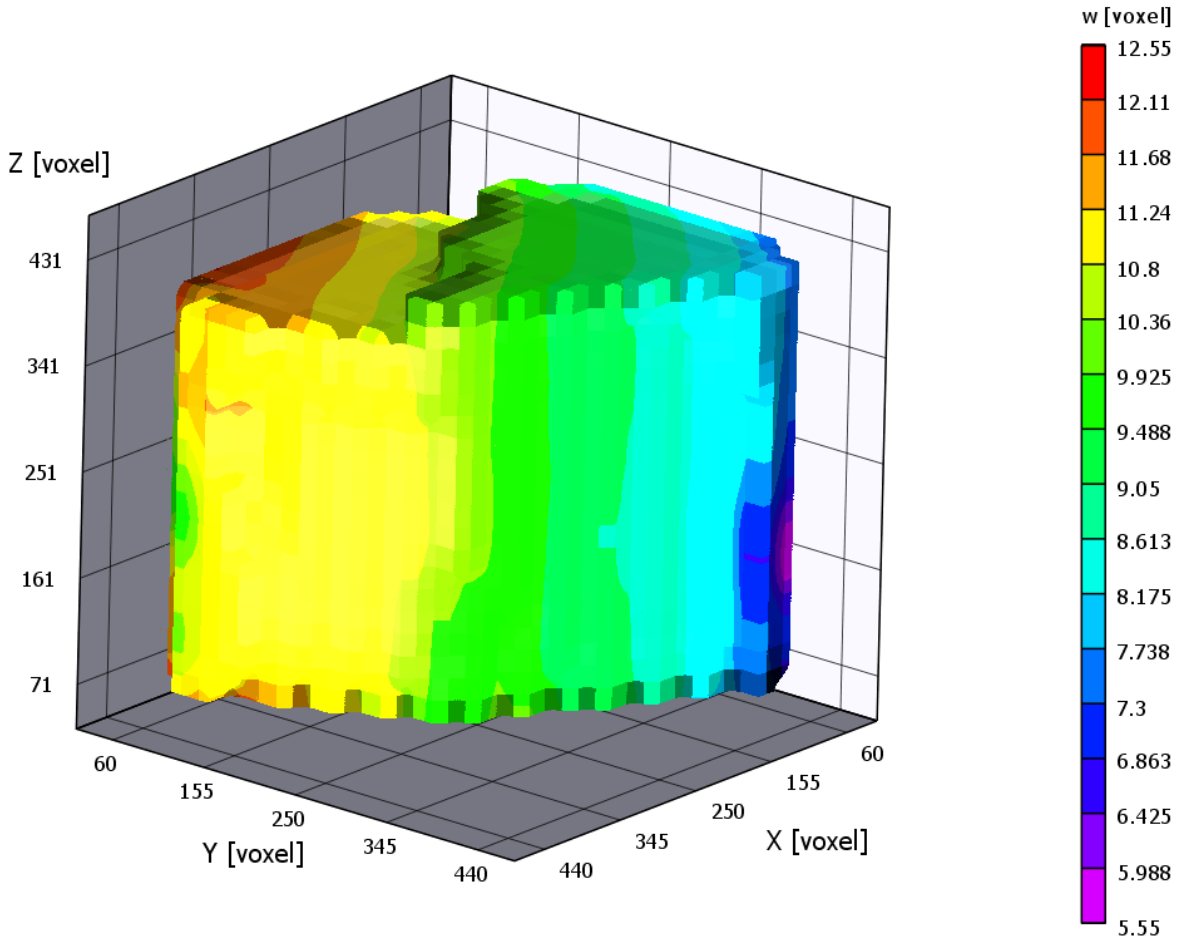

Figure 46: z displacement (voxels) for loaded DVC experiment of inferior neck specimen

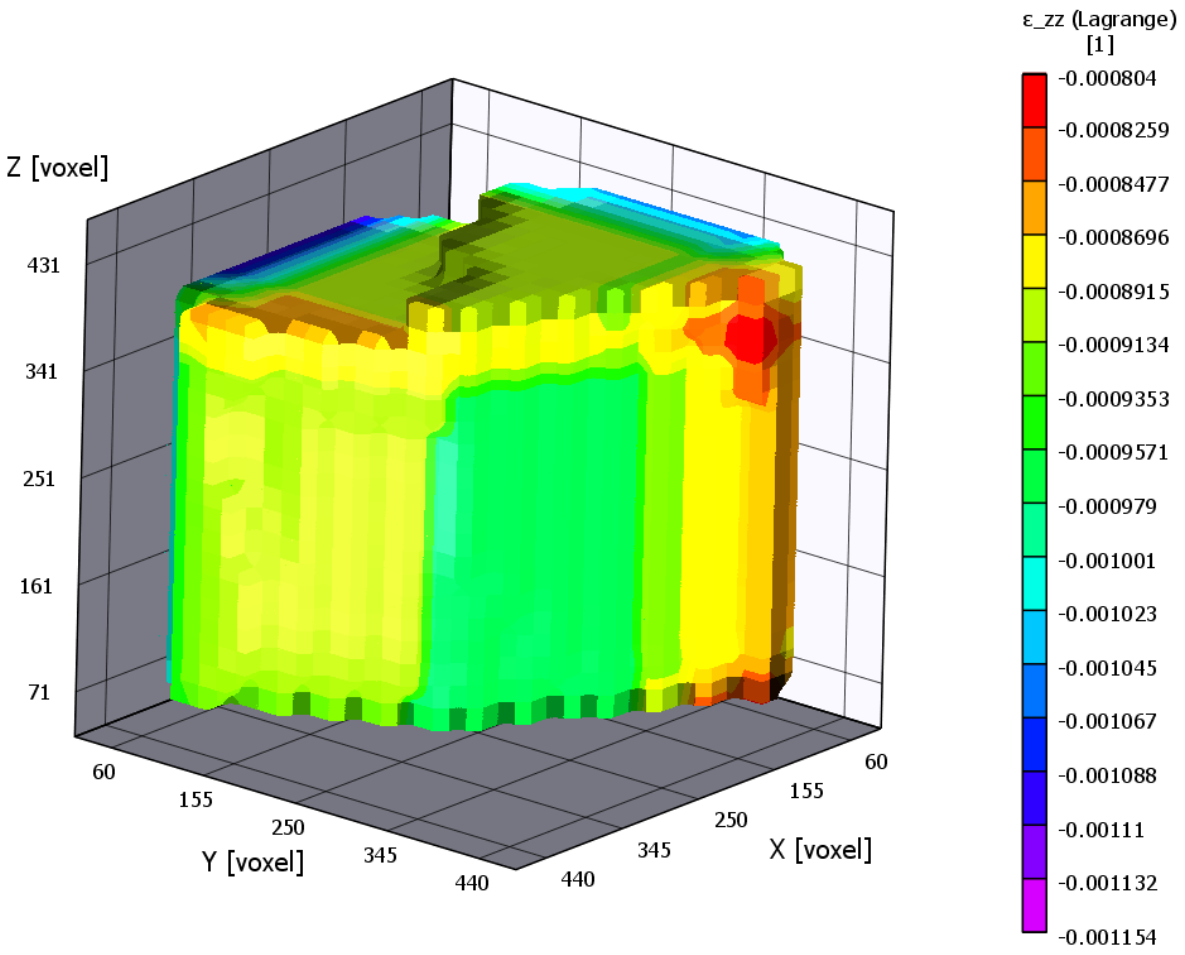

Figure 47: ε_{zz} for loaded DVC experiment of inferior neck specimen